Air-conditioning with TBAB clathrate hydrate slurry as secondary loop refrigerant

S. Drommel

Master Thesis Report
Delft University of Technology

TU Delft

Cover image:
Condenser units of air-conditioning systems in a residential area
(source: Ma Belle Maison (2016))

Air-conditioning with TBAB clathrate hydrate slurry as secondary loop refrigerant

by

S. Drommel

in partial fulfilment of the requirements for the degree of

Master of Science
in Mechanical Engineering

at the Delft University of Technology,
faculty of Mechanical, Maritime and Materials Engineering (3mE)
to be defended publicly on Thursday January 18, 2018 at 10:00 AM.

Student number:	4217411	
Thesis committee:	Dr. ir. C. Infante Ferreira	TU Delft & supervisor
	Prof. dr. ir. T.J.H. Vlugt,	TU Delft
	Dr. ir. S.C. Jansen,	TU Delft
	Ir. S. Lobregt,	Sparkling Projects

An electronic version of this thesis is available at http://repository.tudelft.nl/.

TU Delft

Acknowledgment

First of all, I would like to start off by thanking my supervisor dr. ir. C. Infante Ferreira for his guidance and supervision. I really appreciated the comprehensive feedback from my supervisor and the time he makes available for his guidance. The feedback was not just limited to the technical aspects of my thesis and this was beneficial to the overall quality of my thesis. Also, his sharp critical attitude helped me to remain critical towards my own work. I also would like to thank dr. ir. H. Zhou and ir. L. Pronk for their feedback and guidance in the early stages of my work.

Furthermore I would express my sincere gratitude to ir. S. Lobregt who made the pilot system and thus my thesis work possible. Also, I would thank the guys from Hollander Techniek for their technical support and their help with the pilot system in Twello.

In addition, I am also very grateful to the members of the exam committee for reviewing this thesis work.

Finally I would like to thank my family, friends and Nava for their unconditional encouragement and support and for listening to my struggle. This journey was not possible without their help.

I really enjoyed my time at the TU Delft for the past 5 years. Although it was sometimes hard when the exam period was around the corner, the lectures with my fellow students made sure that I always liked to travel to Delft. In this period, I did not only gained knowledge about engineering principles, but also made new friends and a general critical attitude which I will benefit from for my entire life. This thesis will be the end of my life as a student and will be the beginning of a new part in my life.

Sven Drommel
Delft, January 2018

Abstract

The demand of energy increases steadily due to the growing global population and the increasing living standard of emerging markets. The energy demand is mainly covered from fossil resources in the present and the near future. The growing energy demand is concerning due the exhaustion of natural resources and the heavy environmental impacts such as global warming. The global contribution towards energy consumption of buildings has also steadily increased to between 20% and 40%, mainly due to the conditioning of building spaces. The increasing energy demand and reduction of greenhouse gasses require a significant increase of renewable energy sources and energy efficiency of buildings. Also, the increasing degree of renewable energy sources increase the demand to store excess energy and to bridge the gap between energy production and consumption. This thesis focusses on the possible energy reduction for air-conditioning systems by the application of thermal energy storage and phase change materials (PCMs).

Tetra-n-butylammonium bromide (TBAB) is a promising PCM for air-conditioning applications. PCMs store thermal energy in the form of latent heat. The energy of a PCM is stored or released as it undergoes a phase change. Latent heat thermal storage has a higher energy density compared to sensible heat storage, which limits the needed mass and volume of material for a given amount of energy. PCMs are also promising cold storage media in air-conditioning systems because of the capacity to store energy at constant or near constant temperature. TBAB has a high solubility in water and hydrate crystals are formed in a TBAB aqueous solution at temperatures from 0-12.5 °C depending on the concentration of TBAB in the solution. The solid mass fraction of the slurry is limited to maintain the slurry pumpable.

A small pilot system to control the temperature of a space of 144 m² is installed in the sports hall 'De Jachtlust' in Twello, the Netherlands, in collaboration with Sparkling Projects and Hollander Techniek. The pilot system is equipped with multiple sensors to monitor the system. The air-conditioning system consists out of a primary loop, which uses the conventional refrigerant R134a, and a secondary loop, which uses a TBAB solution as distribution fluid. An initial mass fraction of 36.5 wt% TBAB is used, resulting in a phase equilibrium temperature of approximately 12.5 °C. The hydrate crystals are produced in the generator and stored in a storage vessel of 300 l. The capacity of the air-conditioning system is around 3.5 kW.

The pilot system is modelled with both water and a TBAB solution as secondary distribution fluid by improving and extending an existing model. Each component is modelled resembling the pilot system and the most appropriate heat transfer and pressure drop correlations were selected from the literature. The crystals are produced in the generator by evaporation of the primary refrigerant. The crystals are removed from the heat transfer surface by the friction of the flow. The model assumes a steady state crystal production rate when the removal work is equal to the friction losses. The crystal layer thickness and flow velocity in the generator are calculated by comparing the friction losses to experimental determined scrapping forces required to remove the crystals. Experimental data of the pilot plant are used to validate the model.

The model simulations of the air-conditioning system show a COP increase from 3.27 to 4.30 when a 36.5 wt% TBAB solution is used as a secondary distribution fluid instead of water. The total energy consumption of the system reduces by 18.6 %. The energy consumption of the main contributor to the total energy consumption, the compressor, reduces by 24.8 %. However, the energy consumption of the generator pump increases by 140.3 % due to the adhesion of hydrate crystals to the heat transfer surface. Simulation results show also an increased performance when the initial mass fraction of TBAB in the solution is lowered to 35 wt%. The COP of the system increased to 4.50 mainly due to the reduction of the energy consumption of the compressor. The force required to remove the crystals from the heat transfer surface lowers by lowering the initial mass fraction of TBAB in the solution. Therefore, the steady state crystal layer thickness in the generator reduces, increasing the heat transfer rate by lowering the thermal resistance. However, reducing the initial TBAB mass fraction also lowers the evaporation temperature of the primary refrigerant and the total cooling capacity of the slurry.

Nomenclature

Abbreviations

ACH	Air change rate per hour
CHS	Clathrate hydrate slurry
COP	Coefficient of performance
$LMDT$	Logarithmic mean temperature difference
$TBAB$	Terta-n-butylammonium bromide
TES	Thermal energy storage

Greek

α	Heat transfer coefficient	$W\ m^{-2}\ K^{-1}$
β	Chevron angle	–
Δ	Difference	–
δ	Thickness	m
$\dot{\gamma}$	shear rate	s^{-1}
η	Efficiency	–
λ	Thermal conductivity	$W\ m^{-1}\ K^{-1}$
μ	Viscosity	$Pa\ s^{-1}$
ω	Rotational speed	$rad\ s^{-1}$
Φ	Surface enlargement factor	–
ϕ	Volume fraction	–
ψ	Operand	–
ρ	Density	$kg\ m^{-3}$
σ	Surface tension	$N\ m^{-1}$
τ	Shear stress	Pa
ζ	Loss coefficient	–

Latin

A'	Cross section	m^2
A	Area	m^2
a	Operand	–
B	Bore	m
b	Distance between plates	m
Bd	Bond number	–
Bm	Bingham number	–
Bo	Boiling number	–
C	Concentration	m^{-3}
c_p	Specific heat	$J\ kg^{-1}\ K^{-1}$
D	Diffusivity	$m^2\ s^{-1}$
d	Diameter	m
F	Force	N
f	Darcy friction factor, Function	–
G	Mass flux	$kg\ m^{-2}\ s^{-1}$
g	Standard gravity	$m\ s^{-2}$
Gz	Graetz number	–
H	Height	m
h	Enthalpy	$J\ kg^{-1}$
i	Index	–
K'	Fluid consistency index	–
k	Mass transfer coefficient	$m\ s^{-1}$
L	Length	m
l	Stroke	m
M	Molecular mass	$kg\ kmol^{-1}$
$\dot{m}$	Mass flow	$kg\ s^{-1}$
N	Number, Parameter in Senapati model	–
n	Flow behaviour index	–
Nu	Nusselt number	–
P	Pressure	Pa
p	Pitch	m
Pr	Prandtl number	–
$\dot{Q}$	Heat flow	W
r	Radius	m
Re	Reynolds number	–
S	Parameter in Senapati model	–

Sc	Schmidt number	–
Sh	Sherwood number	–
T	Temperature	K
t	Time	s
U	Overall heat transfer coef.	$W\ m^{-2}\ K^{-1}$
V	Volume	m^3
v	Velocity	$m\ s^{-1}$
$\dot{V}$	Volume flow	$m^3\ s^{-1}$
w	Mass concentration	–
$\dot{W}$	Work	W
W	Width	m
X	Vapour fraction	–
x	Axial position	–

Subscripts

0	Initial
a	Acceleration
air	Air
amb	Ambient
app	Apparent
b	Bend
c	Crystal
CHS	Clathrate hydrate slurry
$comp$	Compressor
$cond$	Condenser
$cool$	Cooling
cr	Critical
cyl	Cylinder
ef	Effective
$elec$	Electric
eq	Equilibrium, Equivalent
$evap$	Evaporation
f	Friction
fan	Fan
fin	Fin
G	Gas
gen	Generator
H	Hydrate
h	Hydraulic
H_2O	Water
i	Inner
in	Inlet
int	Interface
is	Isentropic
lat	Latent
liq	Liquid
m	Mean
max	Maximum
$mech$	Mechanical
$melt$	Melting
mod	Modified
o	Outer
opt	Optimal
out	Outlet
p	Particle
pl	Plate
$prod$	Production
pt	Port
$pump$	Pump
r	Refrigerant
rat	Ratio
ref	Reference
rem	Removal
row	Row
sat	Saturation
$scrap$	Scrapping
set	Settling
sl	Slurry
sol	Solution
t	Tube
$tank$	Tank, storage vessel
$TBAB$	Tetra-n-butylammonium bromide
v	Virtual
vol	Volumetric
w	Wall

Table of contents

List of Figures

List of Tables

1 Introduction

This chapter gives the background of this thesis report. The importance of the application of thermal energy storage (TES) in air-conditioning and refrigeration systems is clarified. Thereafter the fundamentals of the working principle of phase change materials (PCMs) as cold storage media and hydrate slurries are discussed. Also, an overview of the pilot system, the research objective and the outline of this thesis report are given.

1.1. Importance of thermal energy storage

The demand of energy increases steadily due to the growing global population and the increasing living standard of emerging markets [34, 87]. The energy demand is mainly covered from fossil resources in the present and the near future. The growing energy demand is concerning due the exhaustion of natural resources and the heavy environmental impacts such as global warming [36]. Figure 1.1 shows a positive trend of the global temperature anomaly due to increased greenhouse gas emissions [27]. In 2015 the Paris Agreement is signed by members of the UNFCCC [85]. The Paris agreement aims to limit the increase of the average global temperature to 1.5 °C above pre-industrial levels by reducing the greenhouse gas emissions.
The global contribution towards energy consumption of buildings has also steadily increased to between 20% and 40% [67]. This is mainly due to the conditioning of the building spaces. It is expected that around 2060 the global energy demand for air-conditioning exceeds the demand for heating applications and that the cooling energy demand in 2100 is more than 40 times larger than in 2000 [35]. The increasing energy demand and reduction of greenhouse gasses require a significant increase of renewable energy sources and energy efficiency of buildings. The renewable energy sources are not everywhere and at all times available. These factors also increase the need to store excess energy that otherwise would be wasted and to shift the peak power demand to limit load fluctuations of power grids. This thesis focusses on the possible energy reduction for air-conditioning systems by the application of TES and PCMs.

Air-conditioning systems are used to control the temperature and humidity of air by extracting heat from a space. The demand of cooled air is especially high in periods and regions with high environmental temperatures. Conventional air-conditioning systems used originally refrigerants such as CFCs which are phased out under the Montreal Protocol because of the depletion of the ozone layer in the upper atmosphere by these CFCs [86]. Nowadays HFCs and HCFCs are used in conventional air-conditioning systems because they pose a smaller threat to the ozone layer. However, these refrigerants are also very potent greenhouse gases for very low atmospheric concentrations. To limit the need for these refrigerants, secondary loop air-conditioning systems are used increasingly. In these secondary loop air-conditioning systems an environmental-friendly working fluid (the secondary refrigerant) is used to store and distribute low temperature energy. This secondary refrigerant limits the amount of primary refrigerant in the system significantly, which reduces the environmental risks. Also, TES can easily be included in secondary loop air-conditioning systems. TES is an effective method to shift the peak load of an air-conditioning system to off-peak times [90]. TES also enables the system to shift the load to night time when lower ambient temperatures are available for the primary refrigeration cycle. Working fluids with high power capacity during discharging and charging and a high energy density are preferred for TES applications.

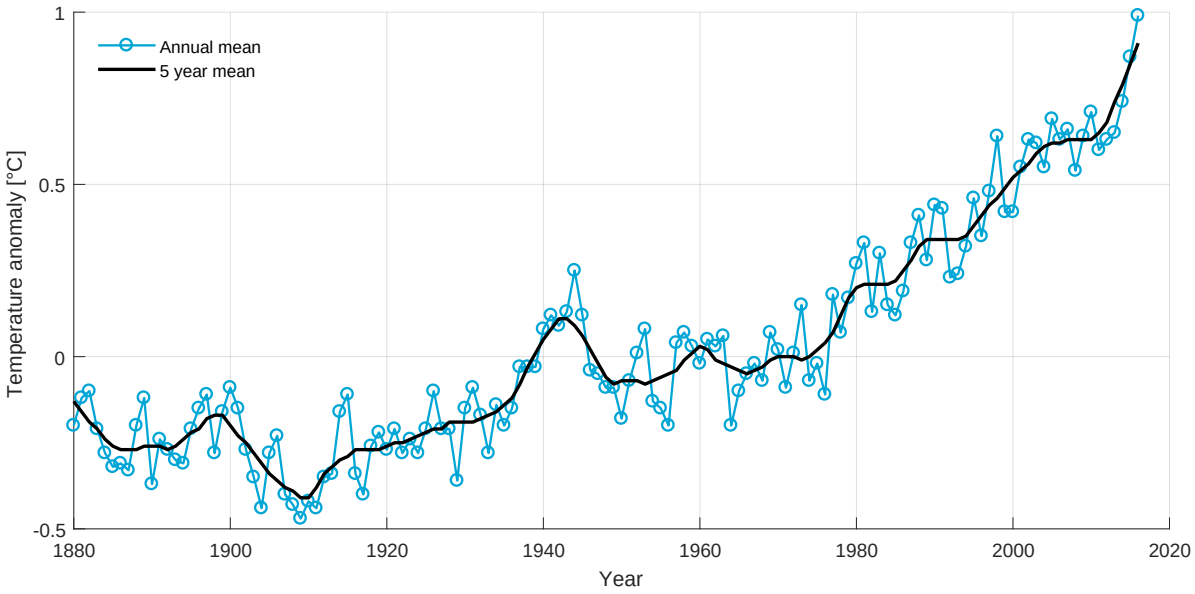

Figure 1.1: Global temperature anomaly measurements of NASA/GISS [27].

1.2. Cold energy storage with phase change materials

Conventional secondary loop air-conditioning systems use water as a secondary refrigerant between the chiller and the application site. In these systems water is cooled down from 12 °C to 7 °C in the evaporator of the primary refrigerant which is evaporated at about 2 °C. Then, the chilled water is used in the application heat exchanger to cool down air for example from 26 °C to 18 °C. Water is heated up from 7 °C to 12 °C at the application site. The temperature levels of water in the air cooler and evaporation of the refrigerant limit the overall efficiency of the system. Also, when water is used as a TES medium, only sensible heat is used which requires large storage volumes or large temperature differences. In addition, the low specific heat of water requires a large amount of energy to transport the water in the system. The pumping power of these systems can account from 20-50% of the total energy usage of the whole system [94, 95]. These problems can be solved by using a PCM as a secondary loop refrigerant.
PCMs store thermal energy in the form of latent heat. The energy of a PCM is stored or released as it undergoes a phase change. Latent heat thermal storage has a higher energy density compared to sensible heat storage, which limits the needed mass and volume of material for a given amount of energy [2, 45]. PCMs are also promising cold storage media in air-conditioning systems because of the capacity to store energy at constant or near constant temperature. The most promising PCMs for cold energy storage in air-conditioning systems are hydrates.

1.3. Hydrate slurry fundamentals

Hydrates are PCMs with appropriate phase change temperatures for cold energy storage of around 5-12 °C and a high enthalpy of fusion [91]. A hydrate slurry is a mixture of water and hydrate crystals. A hydrate crystal is an ice-like structure of a compound which contains water or its constituent elements. One promising hydrate slurry is a mixture of water and tetra-n-butylammonium bromide (TBAB). TBAB is a white salt which has a high solubility in water. Figure 1.2 shows the temperature levels of a secondary loop air-conditioning system with water and TBAB slurry as a distribution fluid. The cooling capacity of TBAB clathrate hydrate slurry (CHS) is about 2-4 times as large as chilled water [95, 99]. The TBAB hydrate crystals are formed in the aqueous solution at a temperature from 0-12.5 °C depending on the concentration of TBAB in the solution. The solid mass fraction of the slurry is limited to maintain the slurry pumpable. Another advantage of the application of TBAB as a secondary loop refrigerant is the limited safety risk. The system operates, unlike systems based on CO_2 hydrates, at low pressures. The low pressures result in a safer and more economically feasible system. TBAB powder can cause skin irritations by contact and is toxic when it is swallowed [60]. These hazards are avoided when a TBAB solution is integrated properly in the air-conditioning system. The TBAB solution can also be reused when the air-conditioning system is dismantled, since TBAB does not

deteriorate.

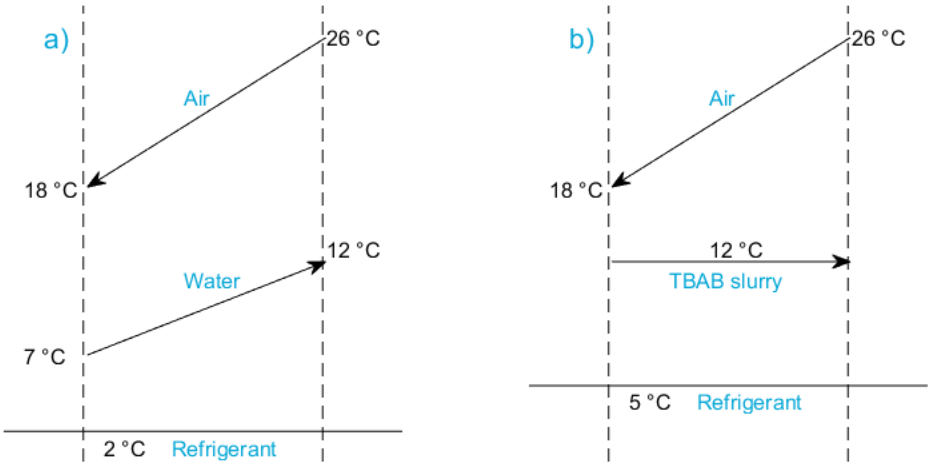

Figure 1.2: a) Working principle of air-conditioning system with water as a secondary loop refrigerant. b) Working principle of air-conditioning system with TBAB slurry as a secondary loop refrigerant.

1.4. Overview of the TBAB air-conditioning system in Twello

A pilot air-conditioning system with TBAB as a secondary loop refrigerant is installed in Twello. This air-conditioning system cools down a space of 144 m². Figure 1.3 shows a schematic overview of the pilot system in Twello. The air-conditioning systems consists out of two separate loops: the primary loop and the secondary loop. The primary loop makes use of the conventional refrigerant, R134a. The secondary loop has a TBAB solution as a distribution fluid. In the primary loop, the refrigeration cycle, heat is extracted from the secondary loop in the generator by evaporating R134a. The heat is released to the environment by the condenser in the primary loop. A compressor pumps R134a through the primary loop and pressurizes the refrigerant. The condensed refrigerant goes then through the expansion valve where the pressure abruptly decreases, causing the refrigerant to flash. Thereafter the liquid-vapour mixture vaporizes completely in the generator completing the thermodynamic cycle. The evaporation temperature of the refrigerant is indirectly controlled by controlling the compressor. A higher pressure results for example in a higher evaporation temperature of the refrigerant. The mass flow of the refrigerant is controlled by throttling the expansion valve.
By cooling the TBAB solution in the secondary loop, crystals will start to form if the temperature of the solution reaches the phase equilibrium temperature. This results in a suspension of hydrate crystals in a TBAB solution. This suspension is called a clathrate hydrate slurry. These crystals start to form in the generator. The generator is a plate heat exchanger where heat is transferred from the secondary to the primary loop. A pump pumps the TBAB CHS through the generator at the generating side of the secondary loop. The TBAB CHS is then stored in a storage vessel until there is a cooling demand.
When there is a cooling demand, TBAB CHS is pumped from the storage vessel to the air cooler at the utilization side. In the air cooler the TBAB crystals melt and cool down the air stream. The cooled air stream is used to regulate the temperature of the space. When the mass fraction of the crystals reduces below a certain setpoint, the systems starts to generate crystals at the generator side. The air-conditioning system can simultaneously produce crystals and cool down the air stream in the air cooler. Because the secondary loop includes a storage vessel, the crystal production can be shifted to night-time to smooth out the grid peak load and reduce the energy costs. The system can in this manner benefit from the lower night tariff by reducing the energy costs. This can also be realized with water as a secondary loop refrigerant. But TBAB has some additional energy saving benefits:

- By shifting the crystal production to night-time, when the ambient temperature is lower, the temperature and pressure in the condenser can be reduced. This reduces the power consumption of the compressor and the condenser fan.

- The hydrate crystals are produced around 12-12.5 °C depending on the initial TBAB mass fraction, while water needs to be cooled down to 7 °C. This allows the evaporation temperature of the primary refrigerant in the evaporator to be increased. This also reduces the power consumption of the compressor.
- TBAB CHS has a higher cooling capacity than water. This reduces the needed pumping power at the utilization site.

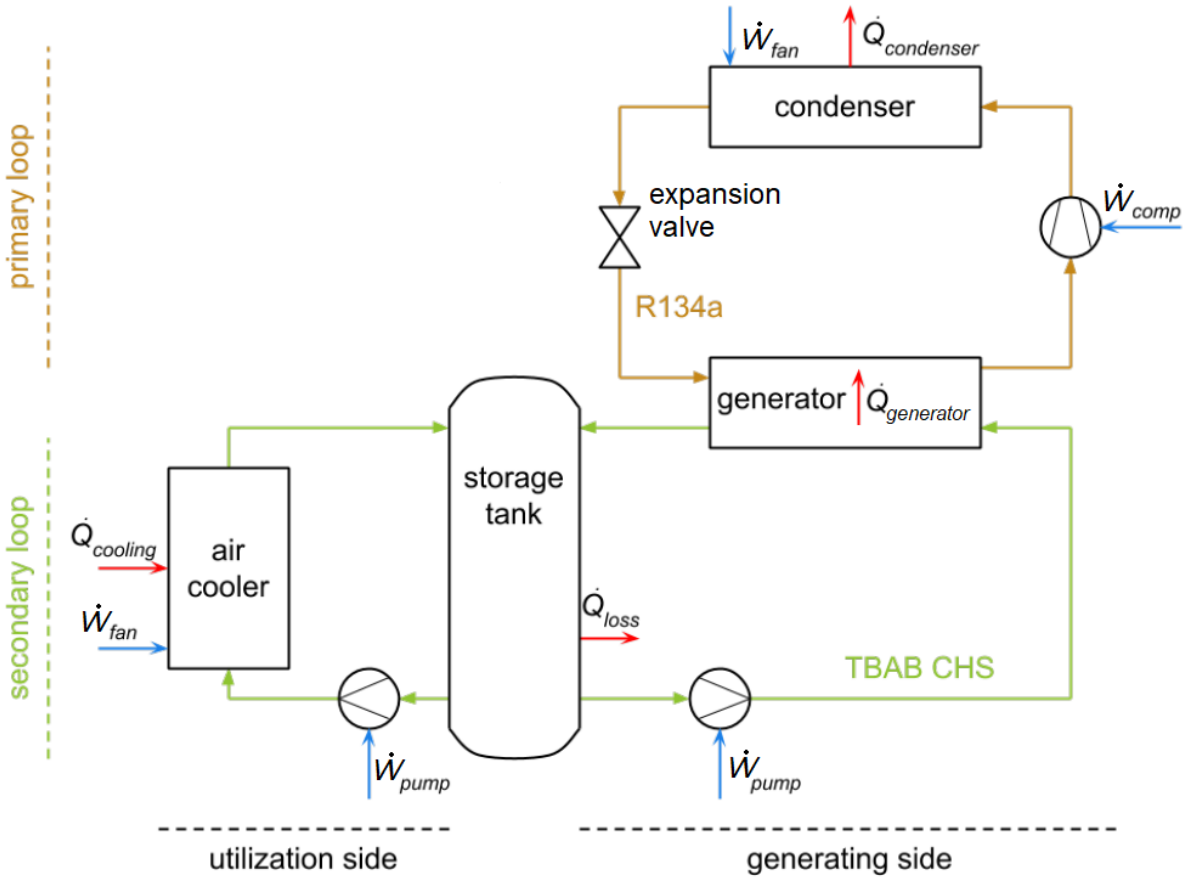

Figure 1.3: Schematic overview of the pilot air-conditioning system in Twello with TBAB as a secondary loop refrigerant.

The application of TBAB as a secondary loop refrigerant has also some disadvantages compared to water:

- TBAB is much more expensive compared to water. The price of TBAB depends on the quantity and the purity of TBAB itself. The TBAB used in the pilot system in Twello has a purity of 96% and costs around €10.00/kg. The pilot system in Twello uses around 120 kg of TBAB which increases the investment costs.
- A system with TBAB requires a larger generator compared to a system with water. This increases the initial investment costs.
- A TBAB system requires other pumps to distribute the slurry efficiently.
- The pump which pumps the slurry through the generator uses more power in the TBAB system. This is caused by the limited flow passage area in the generator by the crystal layer. Also, the pressure drop at the generator side is higher for the TBAB system.

1.5. Research objective

This thesis focusses on the quantification of the advantages of the application of TBAB clathrate hydrate slurry as secondary loop refrigerant in an air-conditioning system. The hypothesis of this work is as follows:

The coefficient of performance of the air-conditioning system in Twello can significantly be increased by using TBAB clathrate hydrate slurry as a secondary loop refrigerant instead of water.

The hypothesis will be validated by a model of the air-conditioning system in Twello. The model made by Zak [98] and improved by Pronk [68] will be further improved and extended. The original model of the air-conditioning system in Twello by Pronk is only validated for water as a secondary loop refrigerant. Also, the generator is modelled as a tube and should be replaced by a proper model of a plate heat exchanger. The improved model will be validated for TBAB CHS as secondary loop refrigerant with experimental data obtained from the pilot air-conditioning system in Twello. At last the model is used to compare the performance of the TBAB air-conditioning system with a conventional air-conditioning system.

1.6. Thesis outline

The chapters in this thesis report contain the following subjects:

- Chapter 2: this chapter gives an overview of the fundamental studies of TBAB as a secondary loop refrigerant.
- Chapter 3: this chapter gives an insight of the relevant correlations which are used in the model to describe the properties of a TBAB hydrate, solution and slurry.
- Chapter 4: this chapter describes the pressure drop and heat transfer correlations from the literature. The most suitable correlations are selected for the model based on data from research papers.
- Chapter 5: this chapter treats the modelling approach of each component of the pilot air-conditioning system in Twello. The correlations and modelling methods of each component are discussed.
- Chapter 6: this chapter contains the comparison of the modelled components and the experimental data of the pilot system. Based on the experimental data, the model of each component is improved by selecting the most suitable correlations.
- Chapter 7: this chapter discusses the most optimal mass flow rates at the generation and utilization side of the pilot system based on the energy consumption.
- Chapter 8: this chapter presents the simulation results and discusses the results and its implications.
- Chapter 9: this chapter answers the main research question and recommends topics to improve the current research and for further research. Also, improvements of the pilot system are suggested.

2

An overview of fundamental studies of TBAB as secondary loop refrigerant

This chapter gives an overview of fundamental studies of tetra-n-butyl ammonium bromide hydrate slurry in air-conditioning applications and as secondary loop refrigerant. These studies give an insight in the general phenomena of TBAB CHS in air-conditioning systems. The properties from the literature of TBAB clathrate hydrate, TBAB solution and TBAB CHS will be discussed in chapter 3.

2.1. Crystallization of TBAB

TBAB is at atmospheric conditions a white salt with a high solubility in water. When a TBAB solution is cooled down below equilibrium conditions, two different types of TBAB hydrate crystals can be formed: type A and type B hydrates. A TBAB clathrate hydrate crystal consists out of water molecules which form a cage-like structure around a TBAB molecule [81]. The TBAB hydrate crystals are stable at atmospheric conditions and easy to handle, unlike many other clathrate hydrates. Equation 2.1 represents the formation process of TBAB hydrates. One TBAB molecule forms together with a number, N, of water molecules a hydrate crystal. The number of water molecules in a hydrate crystal is different for the type of TBAB hydrate which is formed [47]. The number of water molecules which are needed to form one hydrate crystal is called the hydration number.

$$TBAB + N \cdot H_2O \rightleftharpoons N \cdot TBAB \cdot H_2O \tag{2.1}$$

The phase transition temperature of TBAB hydrate crystals at atmospheric pressure can be changed from 0 °C to 12 °C depending on the initial concentration of TBAB in the aqueous solution [65]. Also depending on the initial concentration of TBAB in the aqueous solution and the temperature, two different types of hydrate crystals can be formed. The structures of the two hydrate types are crystalline water-based solids physically resembling ice. Both types of TBAB hydrates have a different structure [47]. Type A TBAB hydrate has a columnar shape, see figure 2.1. Type B hydrate crystals are irregularly shaped. The growth kinetics of a single type A TBAB hydrate crystal have been studied for different supercooling degrees [77]. The growth velocity in transverse- and longitudinal direction have been measured. It was found that the hydrate crystals grow logarithmically with respect to the supercooling degree in the longitudinal direction. The growth velocity was independent of the size of the cross section. The growth velocity in the transverse direction was not measurable at supercooling degrees less than 1.4 K. Above this supercooling degree, the growth velocity increased rapidly with increasing super cooling degree.
The formation of the TBAB hydrate crystals can be described by de following procedures [57]:

- First of all, the thermodynamic state of the system has to be shifted away from the phase equilibrium conditions, i.e. the aqueous solution has to be supersaturated with respect to the crystallizing compound. For instance by cooling the solution down below the phase equilibrium temperature (cooling crystallization).

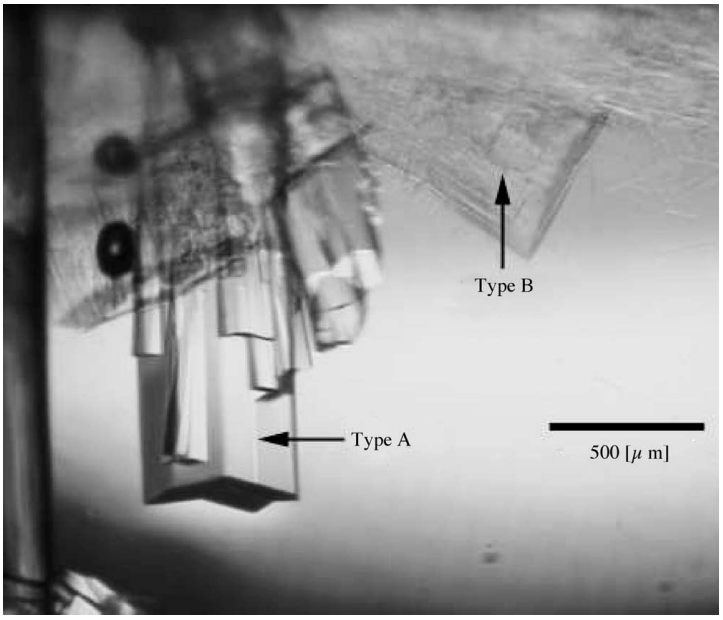

Figure 2.1: The two different hydrate crystal types of TBAB: type A and type B [65]. Type A has a columnar shape while type B crystals are irregularly shaped.

- Secondly, nucleation will start in the supersaturated aqueous solution. The nucleation starts in most cases because of impurities in the solution or at a surface of a wall. When the sensible heat lost due to supercooling is less than the heat released upon solidification, the temperature of the slurry rises to the phase equilibrium temperature and stays there until the phase change of the solution is completed.
- The nuclei start to grow into macro crystals. The supercooling stays the driving force behind the crystallization process, although a smaller supercooling degree is necessary to facilitate the nucleation process.

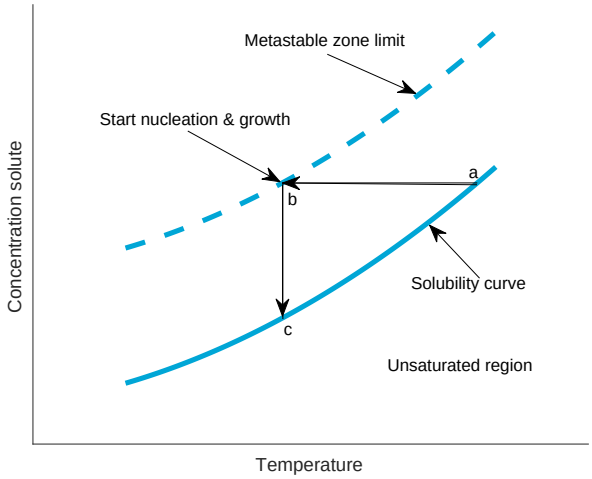

Figure 2.2: Simplified process of cooling crystallisation. The solubility of TBAB depends on the temperature and crystals will start to appear when the temperature of the solution is low enough.

Figure 2.2 shows a general solubility curve which represents a TBAB solution. The solubility increases for increasing temperature. The metastable zone limit is indicated with a dashed cyan line. During cooling crystallization, the TBAB solution is cooled down from point a to point b. At point b the solution reaches the metastable zone limit at which nucleation starts. The solution is kept at a constant temperature and crystals will start to grow. The concentration of the solute, TBAB, in the solution lowers from b to point c as crystals are formed. When the solution reaches the solubility curve, the crystals stop growing.

2.2. Hydrate crystal production methods

In the pilot system, the crystals will mainly grow on the surface of the generator. There are many different types of hydrate slurry generators. The most general generator for hydrate slurries is the tube heat exchanger, since they are easy to manufacture and the investment costs are low. The risk of blockage of the tubes and the difficulty to control the hydrate crystal production process limit the usability of this cost effective generator. Also, the formed crystal layer on the tube wall increases the thermal resistance drastically. Zhang and Ma [99] discussed three main types of generators which are able to detach the hydrate crystal layer from the heat transfer surface.

- Scraped surface generator: inside a tube a scrapper blade applies strong friction forces on the tube wall, which increases the heat transfer performance by removing the crystal layer. The blade of the scraped surface generator needs to be replaced after a certain time. This increases the maintenance cost. Also, the initial investment costs and energy consumption are considerably high.
- Orbital rod generator: in this generator, consisting out of a vertical shell-and-tube, the refrigerant is evaporated at the shell side, while also multiple tubes are inside the shell. Inside each tube a metallic whip rod rotates around the circumference of the tube to increase the heat transfer rate.
- Fluidized bed generator: small solid particles are added into the tubes of a shell-and-tube heat exchanger to detach the formed crystal layer from the tube wall. The solid particles also remove the necessity of periodical cleaning for this type of heat exchanger. The fluidized bed generator can also be used to produce ice slurries [69].

Shi and Zhang [74] investigated different TBAB crystal generation methods. By continuous cooling of the heat transfer surface, the crystals adhere strongly to the heat transfer surface [15]. They found that the high scrapping forces which are needed to detach the TBAB crystals from the heat transfer surface, resulted in high power consumption of the scrapper. Therefore, they investigated different strategies with reverse operation of the refrigerator to produce crystals in a double-tube heat exchanger. They found a higher COP (coefficient of performance) for the method which keeps the temperature of the heat exchanger wall relatively at a higher level. This reduces the crystal adhesion to the wall significantly. Also, a higher flow rate generally results in a higher COP since less crystals are produced in the generator and the strong shear forces flush down the adhered crystals from the wall of the heat exchanger. Ma et al. [49] also used this technique to generate TBAB crystals.
Zhou et al. produced TBAB crystals in a coaxial double-tube heat exchanger with a different method. They used the friction between the flow and the tube wall to detach the crystals from the heat transfer surface [105]. During the crystal generation process, the supercooling degree was limited to prevent blockages and limit the adhesion of the crystals to the tube wall. The shear force induced by the flow was sufficient to break the crystal layer and maintain a steady state crystal layer thickness. This process is modelled to predict the steady state crystal layer thickness for a given flow rate [98]. To obtain a steady state crystal layer thickness, the crystal removal rate is equal to the crystal production rate. The friction force that is exerted on the crystal layer can be found from the following energy balance:

$$\dot{V}\Delta P = \dot{W}_f \tag{2.2}$$

When it is assumed that the pressure drop is only induced by friction of the fluid with the crystal layer, than the work done by friction can be expressed as:

$$\dot{W}_{rem} = \dot{W}_f = \dot{V} f \frac{L}{d_i - 2\delta_c} \rho v^2 \tag{2.3}$$

The detachment characteristics of TBAB crystals has been investigated by Daitoku and Utaka [13–15]. TBAB crystals were removed from different surfaces and with various scrapping devices. They found that the scrapping force needed to remove initially formed crystals was lower than the scrapping force required to remove repeatedly formed crystals. Also, the material of the adhesion surface and concentration of TBAB in the solution have influence on the required scrapping force.
Matsumato et al. [56] also investigated the detachment characteristics of TBAB on a copper surface. They concluded that the shearing stress increased by decreasing the temperature of the copper surface. Also, the

type of TBAB hydrate crystal which is formed on the heat transfer surface has no influence of the required shear stress.
Another type of heat exchanger which is suitable for the production of some types of hydrate slurries is the plate heat exchanger. Although a plate heat exchanger is limited by its operating conditions, a maximum temperature of 150 °C and pressure of 20 bar [1], it is suitable to produce TBAB hydrate slurry. Ma and Zhang [49] have used a plate heat exchanger to conduct experiments with TBAB hydrate slurry. They investigated the heat transfer- and pressure drop characteristics of TBAB CHS flowing through a plate heat exchanger. A plate heat exchanger combines a large heat transfer area with a small volume and is widely commercially available.

2.3. Storage of TBAB crystals

The TBAB hydrate crystals are stored in a storage vessel after they are produced in the generator. When TBAB hydrate crystals are stored in the storage vessel, several different phenomena should be considered. TBAB hydrate crystals are mainly stored in two modes: heterogeneous and homogeneous storage [22]. Homogeneous storage of TBAB hydrate crystals require agitation to prevent the agglomeration of particles in the storage vessel. Since the crystals are denser compared to the fluid, the crystals tend to settle at the bottom of the storage vessel over time. To prevent agglomeration and settling of the crystals, the slurry should be stirred inside the storage vessel for homogeneous storage. Homogeneous storage of the slurry requires additional power and it is reported for ice slurries that homogeneous storage is possible for maximum ice fractions up to 30-35 wt% [30]. Higher ice fractions resulted in a significant increase of the power consumption. The power consumption to agitate 52 wt% ice slurry was 10 times larger compared to 30 wt%.
Heterogeneous storage of ice slurry is possible up to a maximum solid fraction of 50-60 wt% and the necessary volume of the storage vessel can be reduced compared to homogeneous storage [30]. Different storage methods of TBAB CHS have been compared by Shi and Zhang [74]. They reported a lower COP for the homogeneous storage approach compared to the heterogeneous storage approach. In the heterogeneous storage vessel, the crystals tend to settle at the bottom of the storage vessel which allowed a higher supercooling degree at the outlet of the tank. Furthermore, the lower mass fraction of TBAB CHS pumped from the heterogeneous storage vessel into the heat exchanger was beneficial for reducing the crystal adhesion to the heat exchanger wall.
The storage vessel in the pilot system is a heterogeneous storage vessel, since the TBAB slurry is not agitated. The modelling of a homogeneous storage vessel is less complicated, since it is sufficient to describe to storage vessel with a single volume element. The properties of the TBAB CHS in this type of storage vessel are an average and can be described by a single value when the vessel is well stirred. The modelling of a heterogeneous storage vessel requires more volume elements to describe the gradient of mass fraction and concentration in the storage vessel. Also, the settling behaviour of the hydrate crystals requires more volume elements. Therefore, an overview of several models which describe this behaviour in heterogeneous storage vessels is given. Although some of these models describe ice slurries, which tend to settle on the top instead of the bottom, the general equations of these models stay valid.

Model of Flick et al.

Flick et al. developed a model for an ice slurry storage vessel [24]. Flick et al. modelled an ice slurry tank as a vertical cylinder with an one-dimensional geometry. They made the following assumptions for their model:

- The ice settling and the solution flow are vertical.
- In every horizontal section the slurry is homogeneous: 1D-model is sufficient.
- The volume of the slurry is constant: melting of ice does not change the volume of the slurry.
- There is no agglomeration of the ice crystals.
- The ice crystals are in local equilibrium with the surrounding solution.

The mean velocity at any given height of the storage vessel is calculated from the flow rates entering and leaving the storage vessel. The velocity is expressed as the weighted average of the solution and crystal velocity.

$$v_m = (1-\phi_c)\, v_{sol} + \phi_c\, v_c \tag{2.4}$$

The settling velocity of ice follows from Stocke's law for equivalent spherical particles. When the ice fraction approaches its maximum value, the settling is dumped.

$$v_c = v_{sol} + v_{set} = v_{sol} + \frac{g(\rho_{sol} + \rho_c)d_c^2}{18\mu} f(\phi_c) \tag{2.5}$$

The material balance takes the effect of the diameter distribution into account by an equivalent ice distribution. At any given height, all the ice crystals grow/melt simultaneously. The number of ice crystals per unit of volume is noted: C.

$$\frac{\partial C}{\partial t} + \frac{\partial}{\partial x}\left(C v_c + D_{c,eq}\frac{\partial C}{\partial x}\right) = 0 \tag{2.6}$$

The ice fraction is calculated from the enthalpy balance. Inside the tank the ice crystals can melt because they migrate to a warmer region or because of lateral heat losses.

$$-\Delta h \frac{\partial}{\partial t}\left(A'_{tank}\rho_c\phi_c\right) + \frac{\partial}{\partial x}\left(A'_{tank}\left(\rho_c \Delta h_{lat}\left(D_{c,eq}\frac{\partial \phi_c}{\partial x} - \phi_c v_c\right) - \lambda_{sl}\frac{\partial T}{\partial x}\right)\right) = \alpha\pi d_{tank}(T_{amb} - T_{sol}) \tag{2.7}$$

The mass concentration of ice in the slurry is also calculated with a mass balance. The surrounding solution is in local equilibrium with the ice crystals, so the ice crystal concentration is related to the temperature through the equilibrium curve.

$$\frac{\partial}{\partial t}\left(A'_{tank}\rho_{sol}(1-\phi_c)w_c\right) + \frac{\partial}{\partial x}\left(A'_{tank}\rho_{sol}\left((1-\phi_c)w_c v_{sol} - (1-\phi_c)D_{sol}\frac{\partial w_c}{\partial x}\right)\right) = 0 \tag{2.8}$$

The equations are solved by a semi-implicit finite volume method in this specific order. The volume fractions, ϕ_c, and concentrations, C, are used to recalculate the mean equivalent ice crystal diameter in equation 2.9.

$$\phi_c = C\frac{\pi d_c^3}{6} \tag{2.9}$$

This model is used by Douzet et al. [20] to describe the settling behaviour of TBAB in a storage vessel. Douzet et al. also assumed that only type A TBAB hydrate crystals were present in the storage vessel. The model was validated by settling experiments on a real TBAB storage vessel. The numerical values of the hydrate mass fraction of the model showed a deviation of around 17% from the experiments.

Model of Tamasauskas et al.

Tamasauskas et al. [83] modelled a ice slurry tank as latent storage material for a solar assisted heat pump. They developed a mathematical model using the following assumptions:

- At each time step, the water and ice crystals separate into two distinct layers.
- There are no temperature gradients within the volume elements.
- There is no supercooling in a ice layer: the ice layer is always at phase equilibrium temperature.
- In the ice layer, the density and porosity is constant.

The storage vessel is divided into two separate layers: one control volume for the crystals which settle at the top and one control volume for the solution. Figure 2.3 shows the schematic representation of the control volumes used in the model. For both control volumes, an energy balance is made. The energy balance for the ice crystals is expressed as follows:

$$-\Delta h_{lat}\frac{d\dot{m}_c}{dt} = \dot{m}_{sol,in}c_p(T_{in} - T_c) - \Delta h_{lat}\dot{m}_{c,in} + \alpha A_1(T_{amb} - T_c) + \alpha A_{c,sol}(T_{sol} - T_c) \tag{2.10}$$

The energy balance of the water volume element is expressed as:

$$\dot{m}_{sol} c_p \frac{dT_{sol}}{dt} = \dot{m}_{sol,in} c_p (T_c - T_{sol}) + UA_2 (T_{amb} - T_{sol}) + \alpha A_{c,sol} (T_c - T_{sol}) \tag{2.11}$$

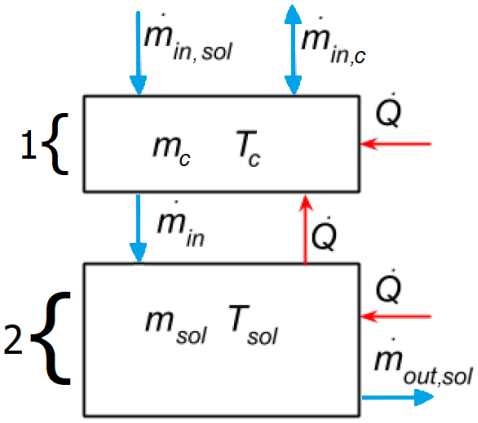

Figure 2.3: Schematic representation of the ice slurry storage vessel model of Tamasauskas et al. [83].

The predicted ice crystal fraction and temperature by the model are in agreement with the experimental data. Although, during the charging process the crystal mass fraction was not well predicted by the model. This was caused by the placement of the temperature sensors at the bottom of the storage vessel, potentially overestimating the actual ice mass fraction. Also, there was no agitation in the storage vessel which may led to a non-uniform temperature distribution in the storage vessel.
The settling velocity of TBAB hydrate crystals is slow [20]. Therefore, a model with only two control volumes is not sufficient enough to model the settling of the crystals.

2.4. Re-laminarization of the TBAB CHS

The solid-liquid two phase flow of TBAB CHS is complexer due to the interactions of the hydrate particles with each other, the tube wall and the carrier fluid compared to single phase flow. Because of the solid particles, the friction of the slurry flow consists out of two parts [55]: mechanical- and viscous friction. The interactions of the hydrate particles cause the mechanical friction. The viscosity of the slurry causes the viscous friction. The dominant friction phenomena of the laminar slurry flow is the viscous friction because the solid particles mainly flow in axial direction. When the slurry flow becomes turbulent, the mechanical friction increases sharply by the enlarged interactions of the solid particles with the tube wall [53]. When the solid mass fraction increases, the mechanical friction of the flow usually also increases. However, the solid particles can also reduce the turbulence of the flow. As the solid mass fraction increases, at a certain velocity the solid particle interactions with the carrying fluid decreases the turbulence intensity, whereby the turbulent kinetic energy is transferred from the turbulent core across the whole flow cross section [62]. This also damps the turbulent eddies. This is called the re-laminarization effect. The re-laminarization of the slurry flow is observed by many studies [40, 41, 49, 50, 53, 76, 82, 93, 97, 100].

2.5. Performance of TBAB in air-conditioning systems

Several studies investigated the energetic performance of air-conditioning systems with TBAB as a secondary loop refrigerant. Zhou et al. [104] found a significant improvement of the COP in a model when TBAB hydrate slurry is used as a latent heat thermal energy storage system (up to 73.5%). Zak [98] modelled a fictional conventional air-conditioning system and a TBAB air-conditioning system with TES and found a system COP of 3.15 and 7.32 respectively. Pronk [68] also modelled a conventional air-conditioning system and a TBAB air-conditioning system with TES based on a physical system and found a COP of 2.96 and 4.0 respectively. Ogoshi and Takao made a trial calculation of the potential energy savings of an office building air-conditiong system by applying TBAB [63]. They reported potential energy savings of 36%. Also by shifting the load from day- to night-time, they calculated potential cost savings of approximately of 42%.

Ma et al. [49] measured the COP during TBAB CHS generation and the pumping power during cold release. The COP mainly decreases for increasing solid mass fraction during generation of TBAB CHS. Due to short piping and low pumping power, no energy saving was achieved using TBAB CHS instead of water.
Shi and Zhang [74, 75] also found a lower COP during generation for increasing solid mass fraction, but an increasing COP for increasing flow rates due to less adhesion of the crystals to the heat transfer surface. They also found varying COPs for different generation strategies.

2.6. Summary

The literature investigated several phenomena which could be encountered in secondary loop air-conditioning system with TBAB as a secondary loop refrigerant. Also, the performance of several operations of TBAB air-conditioning systems are evaluated.
TBAB crystals are produced by cooling crystallization in three steps: supercooling, nucleation and growth. Two distinctive types of TBAB hydrate crystals can form: type A and type B. The type of hydrate which is formed, depends on the initial concentration of TBAB in the solution and the temperature. The main challenge of hydrate production is the adhesion of the crystals to the heat transfer surface.
There are several storage methods for the TBAB slurry. Two main types of storage approaches are discussed: homogeneous- and heterogeneous storage. The heterogeneous storage models of Flick et al. [24] and Tamasauskas et al. [83] can be applied for TBAB slurry. The model of Flick is adjusted by Douzet et al. [20] to describe TBAB slurry in a storage vessel.
The turbulent flow of TBAB slurry has a distinctive feature: the re-laminarization effect. A turbulent TBAB slurry flow at a certain velocity can become laminar when the solid mass fraction increases. The solid particles in the flow damp the turbulence intensity of the flow.
Several studies show the potential energy savings of an air-conditioning system with TBAB as a secondary loop refrigerant. These studies model the air-conditioning system or evaluate a section of the TBAB air-conditioning system.

3

Properties of TBAB

This chapter contains an overview of the relevant properties of TBAB hydrate, TBAB in an aqueous solution and TBAB hydrate slurry. The pilot plant in Twello contains TBAB in an aqueous solution with an initial TBAB mass concentration of 36.5 %. The properties of water, air and R134a are already well known. In the model, the properties of these fluids can be found in the Refprop library [43].

3.1. Phase diagram of TBAB

In this section an overview of several studies about the phase equilibrium temperature will be given. During the crystallization process of TBAB in an aqueous solution, two different kind of hydrates can form from a TBAB aqueous solution [65]. The type of TBAB hydrate crystal that forms, depends on the initial mass concentration of TBAB in the solution and the temperature of the solution. Figure 3.1 shows the phase equilibrium temperature measurements of several studies [16, 40, 65, 103, 105]. The approximate relationships between the TBAB solution saturation temperature and the concentration are expressed by Kumano et al. [40]. The initial concentration was varied from 10 to 30 wt.% while the temperature was varied from 1 to 12 °C in increments of 0.5 °C. Because of the range of the initial concentrations, the polynomials are not representative for higher initial concentrations of TBAB. Furthermore, the correlation of the phase equilibrium temperature of the type B crystals deviates a lot from the measurements of other researchers [16, 65, 103, 105].

$$Type\ A: T_{eq} = 266.64 + 108 w_{TBAB} - 162 w_{TBAB}^2 \tag{3.1}$$

$$Type\ B: T_{eq} = 275.05 + 113.5 w_{TBAB} - 318 w_{TBAB}^2 \tag{3.2}$$

Zak [98] derived better correlations for the phase equilibrium temperature. These correlations are derived from measurements found in the literature. Only the consulted literature for these polynomials is not mentioned explicitly.

$$Type\ A: T_{eq} = 267.98 + 94.91 w_{TBAB} - 127 w_{TBAB}^2 \tag{3.3}$$

$$Type\ B: T_{eq} = 272.75 + 83.36 w_{TBAB} - 150.3 w_{TBAB}^2 - 221.6 w_{TBAB}^3 + 557.4 w_{TBAB}^4 \tag{3.4}$$

Shi and Zhang [76] also derived polynomials from the measurements of Zhang et al. [102], which describe the equilibrium temperature of the TBAB hydrates. These relationships are in good agreement with the measurements of other authors as shown in figure 3.1. Therefore, formula 3.5 will be used to calculate the phase equilibrium temperature of the type A TBAB hydrates.

$$Type\ A: T_{eq} = 267.7 + 96.046 w_{TBAB} - 128.4 w_{TBAB}^2 \tag{3.5}$$

$$Type\ B: T_{eq} = 272.3 + 100.56 w_{TBAB} - 306.14 w_{TBAB}^2 + 291.35 w_{TBAB}^3 \tag{3.6}$$

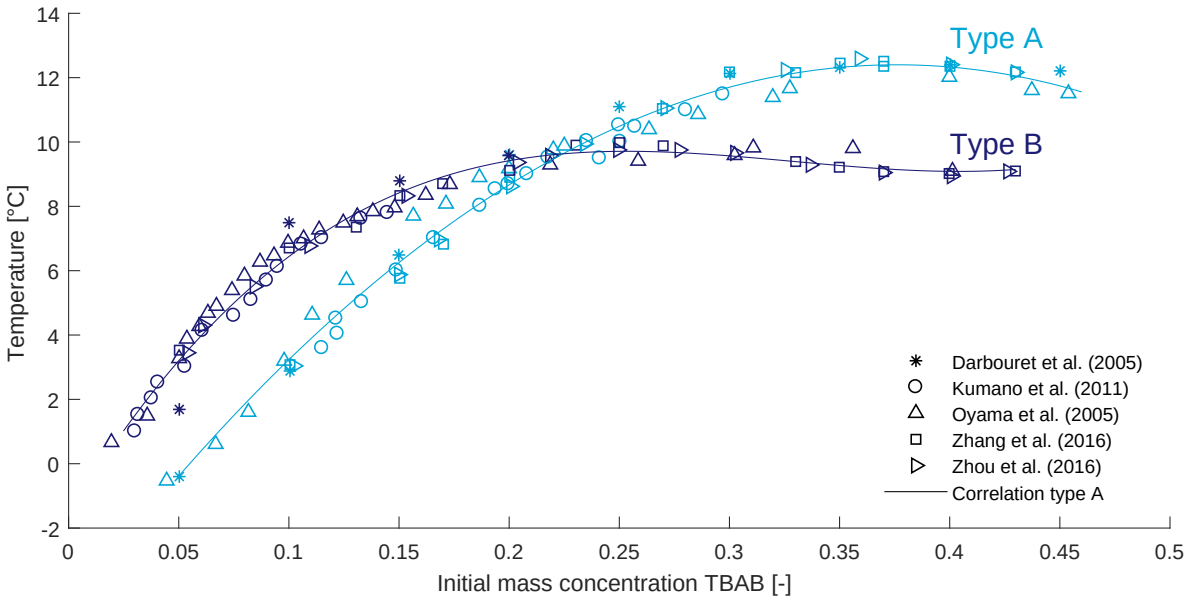

Figure 3.1: The crystallization temperature measurements of TBAB for different initial mass fractions [16, 40, 65, 103, 105]. The Measurements are compared with equation 3.5 and equation 3.6 of Shi and Zhang [76].

3.2. Density

In this section the density of the hydrate crystals and the density correlation of the TBAB aqueous solution and CHS are examined. The density of the hydrates has been investigated by many researchers. The results of these studies are summarized in table 3.1. Most studies agree on the density of the type B hydrate crystals, except the study of Darbouret et al. [16]. Also, most studies agree on the type A hydrate crystal density of 1080 kg/m^3 [53, 63]. This density is also the most used value in further studies [56, 76, 102, 105] and will thus also be used in the present model.

Table 3.1: The density of TBAB hydrates in kg/m^3.

Hydrate	Darbouret et al. [16]	Ma et al. [53]	Ogoshi et al. [63]	Ogoshi et al. [64]	Zhang et al. [103]
Type A	1082	1080	1080	1086	1082
Type B	1067	1030	1030	1030	1030

The density of the solution depends on the initial mass fraction of TBAB in the solution and the temperature of the solution. Zhang et al. [101] and Ogoshi and Takao [63] measured the density of the solution for different temperatures and initial TBAB mass fractions. Zhang et al. derived an empirical relation between the temperature and the mass fraction of TBAB in the liquid phase to determine the density of the solution, equation 3.7. The measurements of the density of the solution of Ogoshi and Takao with initial mass fractions of TBAB of 30.0 and 40.6 wt% are used to fit a function for the density of the solution for an initial mass fraction of 36.5 wt%, equation 3.8. Zhou et al. [105] measured the density of the TBAB solution of 36.5 wt% at different temperatures. The measurements and correlations are shown in figure 3.2.

$$\rho_{sol} = 1003.706 - 0.3959(T - 273.15) + 102.883\, w_{TBAB} \tag{3.7}$$

Figure 3.2 also shows the density measurements of the solution in the pilot plant. Because the purity of the TBAB in the pilot plant, ≥ 96%, it is expected that the density of the solution slightly differs from a TBAB solution prepared with TBAB of a higher purity. Despite that, the correlations are able to predict the density of the solution of the pilot plant. To calculate the density of the solution in the model, the measurements of Ogoshi and Takao are used to make a correlation which depends on the temperature and the mass concentration of TBAB in the liquid phase. Equation 3.8 represents the density of the solution in the pilot plant the most accurately.

$$\rho_{sol} = (12.8758 - 0.162 * (T - 273.15)) * \frac{w_{TBAB} - 0.30}{.106} + 1036.0 - 0.53 * (T - 273.15) \tag{3.8}$$

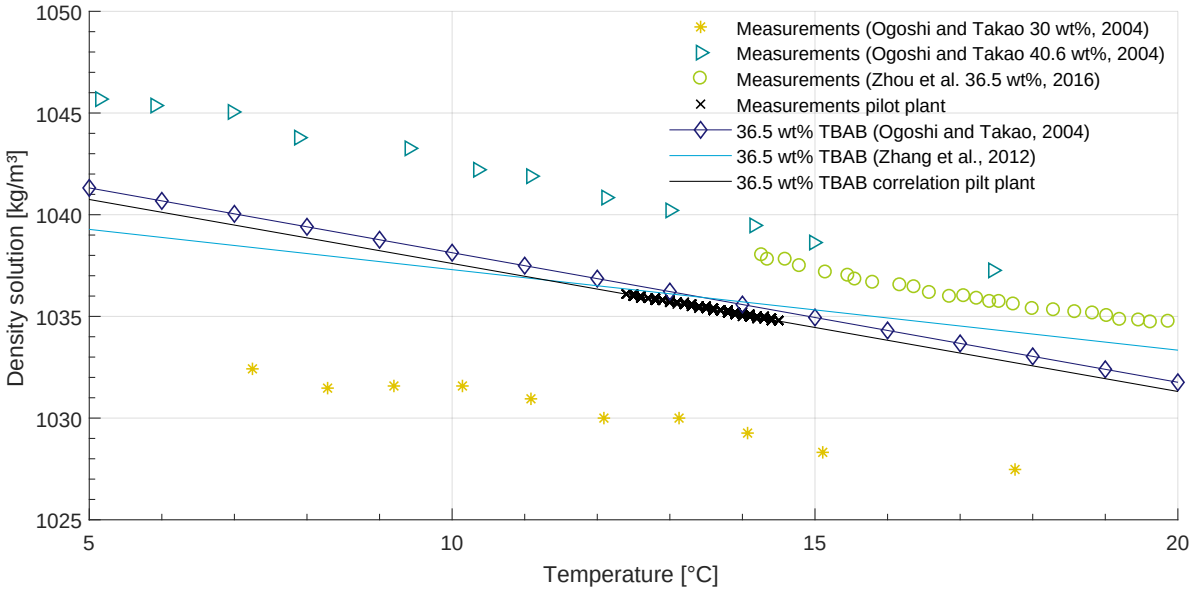

Figure 3.2: Density measurements of TBAB aqueous solution for different temperatures compared with correlations [63, 101, 105].

The density of the TBAB CHS is estimated by using the definition of the volume fraction with the following equation:

$$\rho_{CHS} = \rho_c \phi_c + \rho_{sol}(1 - \phi_c) \tag{3.9}$$

3.3. Hydration number and mass fractions

TBAB forms with water molecules hydrate crystals from a TBAB aqueous solution when the temperature of the solution is below the phase equilibrium temperature. The amount of water molecules that form a hydrate crystal with a TBAB molecule differs by the type of hydrate that is formed. The type of hydrate that forms depends on the initial TBAB mass concentration and the temperature as mentioned in section 3.1. Oyama et al. [65] derived the hydration number of both crystal types from the congruent melting points with equation 3.10. The hydration number from the congruent melting point, defined as the maximum melting temperatures, is 26.0 for type A and 38.0 for type B [16, 47, 65, 77].

$$N = \frac{(1 - w_{TBAB})/M_{H_2O}}{w_{TBAB}/M_{TBAB}} \tag{3.10}$$

Then the hydration number is used in order to estimate the mass fraction of TBAB in the hydrate crystal with equation 3.11.

$$w_H = \frac{M_{TBAB}}{M_{TBAB} + N\, M_{H_2O}} \tag{3.11}$$

The mass fraction of the hydrates in the TBAB CHS is essential for the estimation of the total cooling capacity of the generated TBAB CHS. Equation 3.12 is reported by Ma et al. [53] to estimate the mass fraction of the hydrates in the slurry, which is based on the mass balance of TBAB in both the aqueous solution and the hydrate crystal. The mass fraction of TBAB in the saturated liquid phase of the slurry, w_{liq}, is the concentration on the phase diagram corresponding to the temperature of the slurry.

$$w_c = \frac{w_0 - w_{liq}}{w_H - w_{liq}} \tag{3.12}$$

Figure 3.3 shows the TBAB CHS composition for a given temperature and an initial TBAB mass fraction of 36.5 wt%. Above the phase equilibrium temperature, the solid mass fraction is zero and the mass fraction of TBAB in the liquid phase is 36.5 wt%. When the temperature of the slurry becomes lower than the phase equilibrium temperature, the mass fraction of hydrates in the slurry starts to increase rapidly. The solid mass fraction increases with approximately 0.3 for a temperature change of 0.1 K.

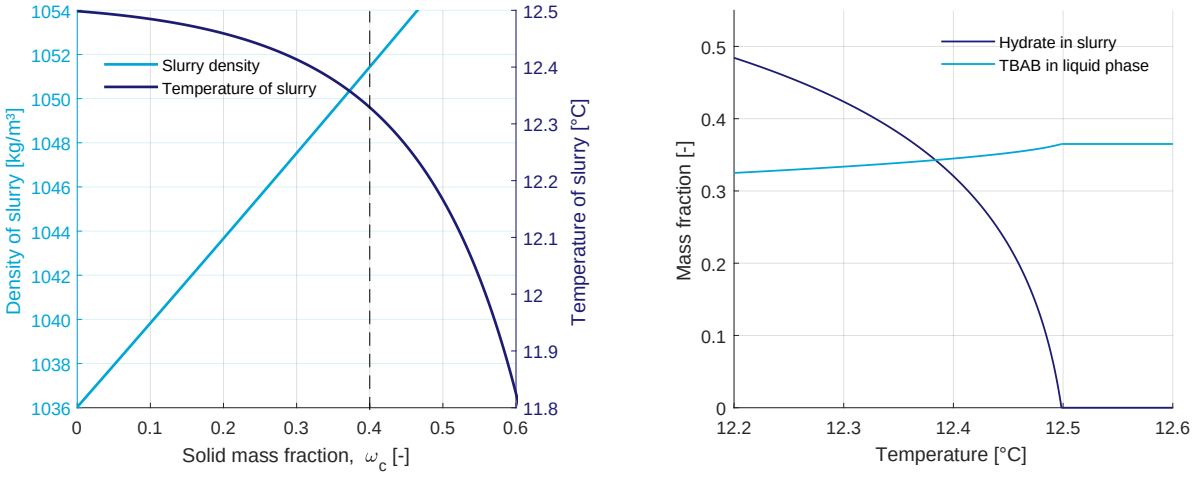

Figure 3.3: Temperature dependency of the TBAB slurry composition and density for $w_0 = 0.365$.

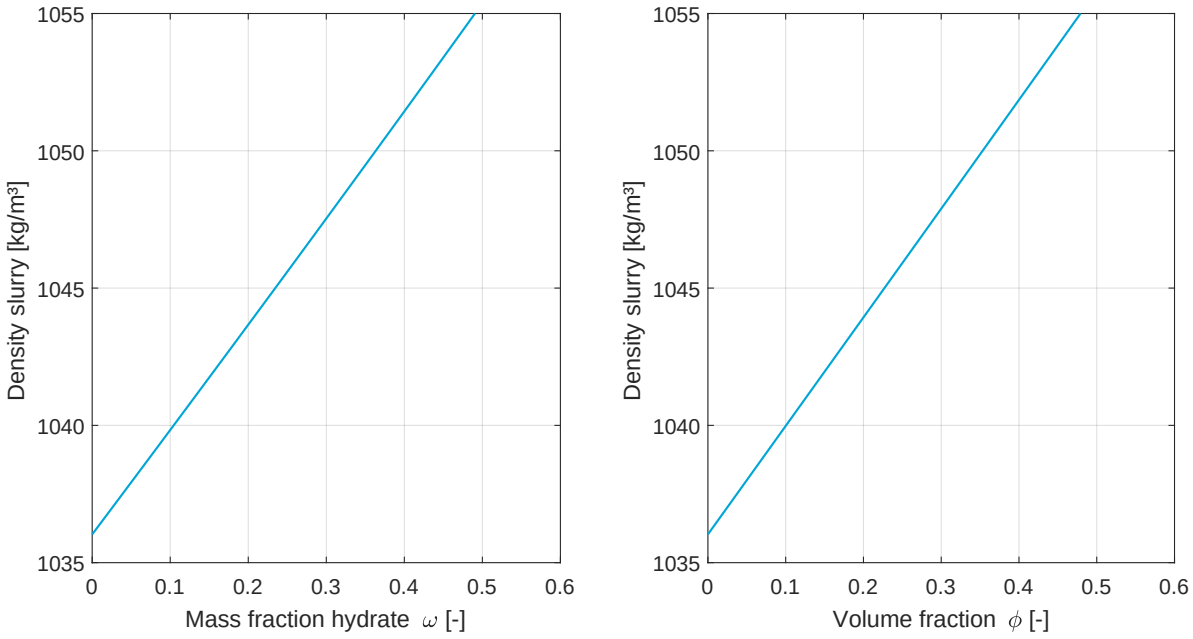

Figure 3.4: The density of TBAB CHS for different hydrate mass fractions and hydrate volume fractions.

3.4. Viscosity

The dynamic viscosity of a fluid is defined as the shear stress divided by the rate of shear deformation.

$$\mu = \frac{\tau}{\dot{\gamma}} \tag{3.13}$$

For a Newtonian fluid, the viscous stresses arising from its flow are linearly proportional to the local rate of

strain. This means that the viscosity of a Newtonian fluid is not dependent on the shear stress and the rate of shear deformation. This is not valid for non-Newtonian fluids. The viscosity of a non-Newtonian fluid depends on the shear stress and the rate of shear deformation. This means that the viscosity of these non-Newtonian fluids is not a constant. The viscosity of these fluids is expressed by the apparent viscosity. The apparent viscosity of a non-Newtonian fluid is the viscosity of this fluid for a given rate of shear deformation. Kumano et al. [39] measured the kinematic viscosity of a TBAB solution. The kinematic viscosity was measured for an initial TBAB mass fraction between 2.5 and 25 wt % at various solution temperatures. They derived equation 3.14 for the kinematic viscosity of the solution at the phase equilibrium temperature. Unfortunately, the viscosity of the solution can only be calculated at the phase equilibrium temperature with equation 3.14 and the correlation is based on measurements of TBAB initial mass fractions between 2.5 and 25 wt %. This makes the correlation less reliable for higher initial mass fractions.

$$Type\ A: \mu_{sol} = \rho_{sol}(3.035 \times 10^{-6} - 1.539 \times 10^{-7}(T_{eq} - 273.15) + 2.73 \times 10^{-8}(T_{eq} - 273.15)^2) \tag{3.14}$$

Zhang et al. [103] also measured the apparent viscosity of a TBAB solution at different temperatures and initial mass fractions of TBAB. They found that TBAB aqueous solution showed Newtonian fluid characteristics and that the viscosity of a TBAB aqueous solution decreased with the increase of the temperature and increased with the increase of the mass concentration of TBAB. They described the viscosity of the TBAB aqueous solution by the Vogel-Tamman-Fulche model. This model uses the dimensionless parameters A, B, C and D as fitting parameters and the temperature T to estimate the viscosity. The fitting parameters A, B, C and D are respectively $0.000298, 87.578, 286.510$ and -47.942 for the TBAB aqueous solution.

$$\mu_{sol} = A \exp^{(\frac{B+Cw}{T-273.15-D})} \tag{3.15}$$

Shi and Zhang [76] measured the viscosity of TBAB aqueous solution and fitted these measurements as an exponential function of the temperature. The viscosity of the TBAB aqueous solution was measured at mass concentrations of 5.0 wt%, 20.0 wt% and 40.0 wt%. The viscosity correlation of TBAB aqueous solution with an initial mass fraction of 36.5 wt% was constructed by interpolating the viscosity correlations of 20 wt% and 40 wt%.

$$\mu_{sol,c20} = 1.34 + 4.07 \exp^{-(\frac{T-273.15}{14.74})} \tag{3.16}$$

$$\mu_{sol,c40} = 2.23 + 17.2 \exp^{-(\frac{T-273.15}{13.64})} \tag{3.17}$$

The models of Zhang et al. and Shi and Zhang are compared with each other and the measurements in figure 3.5. The viscosity from the models is plotted with solid lines and the measurements of Zhang et al. [103] and Kumano et al. [39] are indicated by the markers. The two models deviate slightly from each other. The model of Shi and Zhang is created with a limited range of mass fractions. The Vogel-Tamman-Fulche model is created with measurements from 5.0 to 40.0 wt% and thus provides a more accurate correlation for higher initial mass fractions. This model can also be used to describe the viscosity above and below the phase equilibrium temperature.

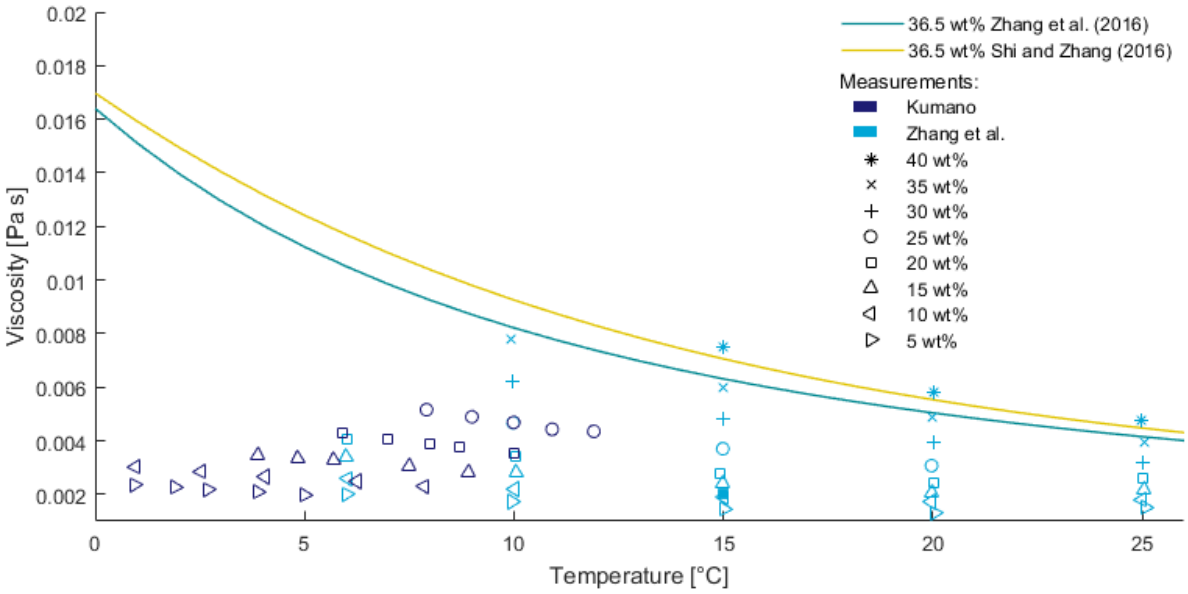

Figure 3.5: The viscosity measurements of TBAB aqueous solution [39, 103] compared with two viscosity correlations [76, 103].

The viscosity of TBAB CHS differs from the viscosity of TBAB aqueous solution. The viscosity of TBAB CHS can be described by some empirical and theoretical models. The dynamic viscosity of a suspension can be calculated by the theoretical Einstein relation 3.18. The dynamic viscosity of the suspension depends in this relation on the solid volume fraction and the dynamic viscosity of the suspending medium. This relation is only appropriate for low solid fractions ($\phi \leq 0.02$). The solid mass fraction in the pilot plant will become higher than $\phi = 0.02$

$$\mu_{CHS} = \mu_{sol}(1 + 2.5\phi) \tag{3.18}$$

For higher solid fractions of $\phi \leq 0.6$ the empirical relation of Thomas can be used. This empirical relation is used to calculate the viscosity of a suspension with spherical particles. Type A TBAB hydrates have rod like structures.

$$\mu_{CHS} = \mu_{sol}(1 + 2.5\phi + 10.05\phi^2 + 0.00273\exp^{16.6\phi}) \tag{3.19}$$

Darbouret et al. [16] proposed to use the model of Graham et al. to calculate the dynamic viscosity of TBAB CHS. Graham et al. introduced a volume fraction of fluid V_0 captured between solid particles forming a cluster. The volume fraction of the fluid is calculated with the generalised Graham model, equation 3.20.

$$V_0 = 1 + \left(\frac{1}{\phi_{max}} - 1\right)\left[1 - \left(\frac{\phi_{max} - \phi}{\phi_{max}}\right)^2\right]^{1/2} \tag{3.20}$$

The corresponding viscosity of the TBAB CHS is given by equation 3.21.

$$\mu_{CHS} = \mu_{sol}(1 - V_0\phi_c)^{-2.5} \tag{3.21}$$

The maximum packing fraction ϕ_{max} depends on the shape of the crystals in the suspension. Darbouret et al. found a maximum packing faction for TBAB type A hydrates of 0.65 by fitting the experimental data to the generalised model of Graham et al..

Zhang et al. [103] measured the viscosity of TBAB CHS for different solid mass fractions and crystal types. They observed non-Newtonian shear-thinning characteristics for TBAB CHS. They used the Eilers (equation 3.22) or K-D model (equation 3.23) and the Senapati model (equation 3.24) to estimate the apparent viscosity of type A TBAB CHS with respectively low and high solid fraction. The transition is about 12.0 wt% for the solid fraction of type A hydrate crystals.

$$\mu_{CHS} = \mu_{sol} \times \left(1 + \frac{0.5[\mu]\phi}{1-\phi/\phi_{max}}\right)^2 \tag{3.22}$$

$$\mu_{CHS} = \mu_{sol} \times \left(1 - \frac{\phi}{\phi_{max}}\right)^{-[\mu]\phi_{max}} \tag{3.23}$$

$$\mu_{CHS} = \mu_{sol} S \times \left[\frac{[\mu]}{\dot{\gamma}}\left(\frac{\phi}{\phi_{max}-\phi}\right)\right]^N \tag{3.24}$$

The proposed value of the intrinsic viscosity of type A hydrate crystals, $[\mu]$, is determined to be 4.692 and 0.44 for the maximum packing fraction, ϕ_{max}, for rod-like crystals. The intrinsic viscosity is a measure for the solute's contribution to the viscosity of a solution. The four models are compared with experimental data from Zhang et al. in figure 3.6. Zhang et al. measured the viscosity of the slurry for different solid mass fractions and shear rates. The Graham Steele Bird model describes the apparent viscosity of the TBAB CHS the most accurately. Also, the Graham Steele Bird model has the best theoretical foundation. The Thomas model underestimates the apparent viscosity of the slurry. The Eilers model and the K-D model both overestimate the apparent viscosity of the TBAB CHS. Both models are developed for non-Newtonian suspensions at a fixed shear stress [103]. This implicates that both models cannot reflect the shear-thinning characteristics of the type A TBAB CHS. The shear-thinning characteristics, the apparent viscosity of the slurry increases more for decreasing shear rates, is mainly prevalent at low shear rates. This behaviour is not described by any of the above mentioned models. However, the shear thinning characteristics are more present at low shear rates, which are less likely to appear during normal operation of the pilot plant. Therefore the Graham Steele Bird model can be used to determine the viscosity of the slurry.

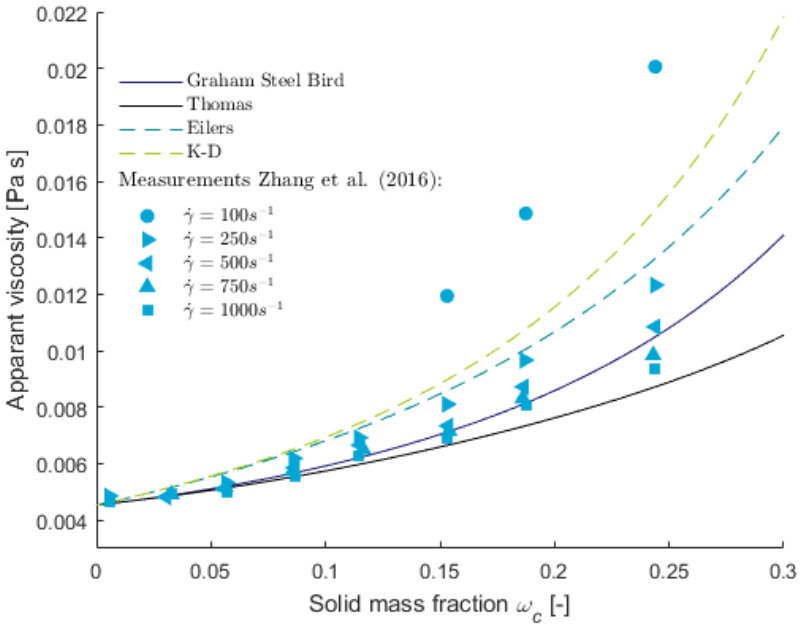

Figure 3.6: Comparison of viscosity models of TBAB CHS for different shear rates and solid mass fractions with experimental data of Zhang et al. [103].

3.5. Specific heat

Ogoshi and Takao [63] reported a specific heat of the type A hydrate crystals of 2220 $Jkg^{-1}K^{-1}$ at unspecified conditions. Oyama et al. [65] measured the specific heat of the two types of TBAB hydrate crystals. In the experiment they produced both crystal types separately. The specific heat of both crystal types was measured seven times using a differential scanning calorimeter. As a result, the specific heat of type A hydrate crystals in $Jkg^{-1}K^{-1}$ can be calculated with the following polynomial.

$$Type\ A: c_{p,c} = -117293 + 1267.5T - 4.554T^2 + 5.5556 \times 10^{-3} T^3 \tag{3.25}$$

Zhang et al. [102] reported a constant value of 4030 $Jkg^{-1}K^{-1}$ for a TBAB aqueous solution for different initial mass fractions of TBAB. The specific heat capacity was determined at 15 °C. Asaoka et al. [7] measured the specific heat of TBAB aqueous solutions with different concentrations. They measured the specific heat of solutions of 8, 25, 27 and 30 wt%. These results can be fitted to a second order polynomial.

$$Type\ A: c_{p,sol} = 4234 - 568 w_{TBAB} - 1016 w_{TBAB}^2 \tag{3.26}$$

The specific heat of the TBAB CHS can be calculated by a mass based average of the specific heat of the type A hydrate crystal and the specific heat of the TBAB aqueous solution.

$$Type\ A: c_{p,CHS} = w_c c_{p,c} + (1 - w_c) c_{p,sol} \tag{3.27}$$

3.6. Latent heat and enthalpy

Several researchers measured the latent heat of the TBAB hydrate crystals. The latent heat of fusion/melting of the hydrate crystals increases the cooling capacity of the TBAB CHS drastically. Ogoshi and Takao [63] measured the latent heat of both crystal types at unspecified conditions. Oyama et al. [65] produced both crystal types separately and stabilized the crystals in liquid nitrogen. The TBAB hydrate crystals were ground to fine powder and the latent heat of the crystals was measured with a differential scanning calorimeter. They repeated the measurements ten and nine times for type A and type B samples respectively. Asaoka et al. [7] also measured the latent heat of both crystal types. They measured the temperature change of the solution after adding crystals in the solution at room temperature. Then the latent heat of the crystals was calculated with an energy balance. Kumano et al. [38] estimated the latent heat by the variation of specific enthalpy of TBAB hydrate slurry. The values of the latent heat found by these researchers is summarized in table 3.2. Since the hydration number of type B hydrate crystals is higher, the latent heat of TBAB type B crystals should be higher too, because of the higher number of water molecules in the hydrate crystal. This makes the results of Kumano et al. [38] less reliable. The measurements of Ogoshi and Takao are supported by Oyama et al.. Therefore, the value of the latent heat of the type A hydrate crystal of Ogoshi and Takao and Oyama et al. will be used.

Table 3.2: The latent heat of TBAB hydrate crystals in kJ/kg.

Hydrate	Ogoshi and Takao [63]	Oyama et al. [65]	Asaoka et al. [7]	Kumano et al. [38]
Type A	193	193.18 ± 8.52	210 ± 10	215
Type B	205	199.59 ± 5.28	224 ± 15	215

The enthalpy of the solution can be determined by using the specific heat of the solution. The reference enthalpy can be determined at any arbitrarily chosen state.

$$h_{sol} = c_{p,sol} T - h_{ref} \tag{3.28}$$

The enthalpy of the TBAB CHS is defined by making use of the latent heat of the crystals [52].

$$h_{sl} = -w_c \Delta h_{melt} + \left(c_{p,sl} T - h_{ref}\right) \tag{3.29}$$

The reference enthalpy that will be used is determined at a temperature of 20 °C and at atmospheric pressure.

$$h_{ref}(T = 293.15\ K,\ w_c = 0\ and\ P = 1\ atm) = 0 \quad kJ\ kg^{-1} \tag{3.30}$$

3.7. Thermal conductivity

Hayashi et al. [31] reported a thermal conductivity of type A TBAB hydrate crystals of 0.42 $Wm^{-1}K^{-1}$ at unspecified temperature and measurement method. Li et al. [44] measured the thermal conductivity from 255 – 283 K and fitted the results explicitly to the following equation.

$$\lambda_c(T) = 217.84542 - 2.37405T + 0.00864T^2 - 1.04767 \times 10^{-5}T^3 \tag{3.31}$$

The conductivity increased at temperatures below 265 K. These low temperatures will not be encountered in the pilot plant. Fujiura et al. [26] also investigated the thermal conductivity of TBAB hydrate crystals. They prepared a solution of an initial mass fraction of 40.52 wt% to ensure that only type A hydrate crystals could form. A transient hot-wire apparatus was used to measure the thermal conductivity of the hydrate crystals. The thermal conductivity was slightly dependent on the temperature, see equation 3.32.

$$\lambda_c(T) = 0.379 + 0.00020 \times (285 - T) \tag{3.32}$$

The thermal conductivity of the TBAB aqueous solution is measured by Fujiura et al. [26] by lowering the temperature with an initial mass fraction of 40.52 wt%. Zhang et al. [102] investigated the thermal conductivity of saturated TBAB aqueous solution along the saturated liquid line. Ma et al. [53] measured the thermal conductivity of the solution for different initial mass fractions at 10 °C. The results of these papers are shown in figure 3.7.

$$\lambda_{sol} = 0.581 - 0.564w_0 \tag{3.33}$$

From the experimental data it follows that the thermal conductivity of the TBAB aqueous solution is more dependent on the initial mass fraction of TBAB than on the temperature. When the initial mass fraction of TBAB goes to zero, the thermal conductivity should be the same as water. This is not the case for a linear fit of the measurements of Zhang et al.. The thermal conductivity of the TBAB CHS will be determined with a Maxwell relation given in equation 3.34 [53].

$$\lambda_{CHS} = \lambda_{sol}\left(\frac{2\lambda_{sol} + \lambda_c + 2\phi_c(\lambda_c - \lambda_{sol})}{2\lambda_{sol} + \lambda_c - \phi_c(\lambda_c - \lambda_{sol})}\right) \tag{3.34}$$

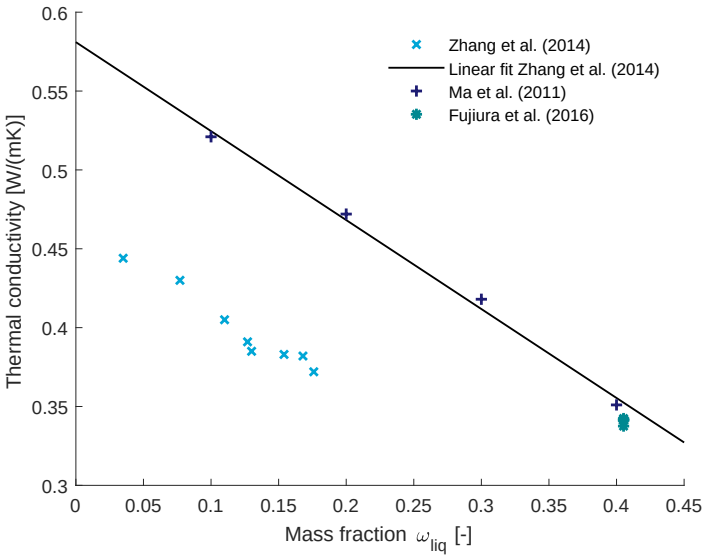

Figure 3.7: Thermal conductivity of the TBAB solution for different TBAB mass fractions.

3.8. Conclusion

The properties of TBAB hydrate crystals, TBAB aqueous solution and TBAB CHS can be described by several different correlations from the literature. The most suitable correlations for the model are summarized in table 3.3.

Table 3.3: Summary of most the suitable correlations for TBAB properties.

	Type A Hydrate	Solution	TBAB CHS
Hydration number	26.0	-	-
Phase equilibrium temperature	-	equation 3.5	-
Density	1080 kg/m³	equation 3.8	equation 3.9
Viscosity	-	equation 3.15	equation 3.21
Specific heat	equation 3.25	equation 3.26	equation 3.27
Enthalpy	-	equation 3.28	equation 3.29
Thermal conductivity	equation 3.32	equation 3.33	equation 3.34

4

Heat transfer and Pressure drop correlations

This chapter gives an overview of the heat transfer and pressure drop correlations of TBAB aqueous solution and TBAB CHS. Many of the transport correlations of TBAB CHS use the modified Reynolds number. First of all, the characteristic velocities which are encountered in the pilot plant and the correlations of the modified Reynolds number will be described. Secondly, the pressure drop correlations of TBAB CHS flowing through straight tubes are discussed. Thereafter, the heat transfer characteristics of TBAB CHS are discussed. Finally, suitable correlations for the pressure drop of the slurry through the plate heat exchanger and the evaporation of the coolant in the plate heat exchanger will be selected. The selected correlations will be used in the current model of the pilot plant.

4.1. Characteristic flow velocities in the pilot plant

The velocities which are encountered in the pilot plant are an import aspect for the determination of the most suitable correlations in this chapter. More detailed information about the pilot plant dimensions and system modelling approach will be discussed in chapter 5. The velocities which are encountered in the main components of the pilot plant such as the generator and the air-cooler are dictated by the pumps in these sections and the local dimensions of the tubes and the plate heat exchanger.
The maximum flow velocity in the air cooler is based on the internal diameter of the tubes in the air-cooler and the number of parallel passages in the air-cooler and the maximum volume flow rate of the pump. The flow velocity in the tubes of the air-cooler will reach a maximum velocity of around $v_{max} \approx 0.69\ m/s$. This maximum velocity results in a laminar flow in the tubes of the air-cooler for the properties of TBAB found in chapter 3.
The maximum flow velocity in the generator is based on the flow passage area between the plates and the number of parallel passages in the generator and the maximum volume flow rate of the pump. The flow velocity between the plates of the generator will reach a maximum velocity of around $v_{max} \approx 0.13\ m/s$ when there is no crystal layer present on the plates. When the distance between the plates decreases due to the increasing crystal layer thickness the flow velocity will also increase. Due to conservation of mass, a halving of the flow passage area will result in a doubling of the flow velocity. This maximum velocity also results in a laminar flow between the plates of the generator for the properties of TBAB mentioned in chapter 3.
When selecting the most suitable correlations for the pressure drop and heat transfer correlations, these maximum velocities will be considered.

4.2. Non-Newtonian fluid behaviour models

TBAB CHS is considered to be a non-Newtonian fluid because of the solid-liquid interactions in the two-phase flow by many researchers [17, 40, 53, 82, 95, 103]. Nevertheless not all researchers agree on the non-Newtonian fluid behaviour of TBAB CHS for every fluid condition. Zhou et al. found that the assumption of Newtonian fluid behaviour of TBAB hydrate slurry can be applied up to solid concentrations of 40 wt% [104, 105]. Zhou et al. obtained the TBAB slurry from a TBAB solution with an initial TBAB mass concen-

tration of 36.5 wt%. Nonetheless, non-Newtonian fluids show various types of non-linearity. These different types of non-linearity can be described by different non-linear relationships between the shear rate and shear stress. Unfortunately, the different researchers did not find an unambiguously non-Newtonian type of flow behaviour for TBAB CHS. Some authors described the flow characteristics of TBAB CHS with a power-law equation as a shear-thinning pseudo plastic fluid [39, 40, 53]. Other authors described TBAB CHS as a Newtonian fluid after overcoming a certain yield stress with the Bingham equation [17, 95]. While there is also evidence for Newtonian fluid behaviour for TBAB CHS under certain conditions as mentioned before [104, 105].
Ma et al. [53] describe the TBAB CHS as a power-law fluid, which can be described by the following equation:

$$\tau = K'\dot{\gamma}^n \tag{4.1}$$

In this equation is K' the fluid consistency index and n the dimensionless flow behaviour index. The dimensionless flow behaviour index, n, indicates the amount a fluid deviates from a Newtonian fluid. The modified Reynolds number can be calculated with the indices K' and n:

$$Re_{mod} = \frac{d^n v^{2-n} \rho}{K' 8^{n-1}} \tag{4.2}$$

To describe some types of non-Newtonian fluids, the modified Reynolds number has been proposed by Metzner and Reed [58]. The dimensionless flow behaviour index and the fluid consistency index are fluid properties which can be determined experimentally. For laminar flow regime of TBAB CHS the Darcy friction factor could be calculated with the following equation:

$$f = \frac{64}{Re_{mod}} \tag{4.3}$$

For the turbulent flow regime, the Darcy friction factor should be calculated with a different correlation. Dodge and Metzner [18] developed a semi-empirical correlation for non-Newtonian fully developed turbulent flows.

$$\frac{1}{\sqrt{f}} = \frac{2.0}{n^{0.75}} \ln\left(Re_{mod} 0.25 f^{\frac{2-n}{2}} \right) - \frac{0.2}{n^{1.2}} \tag{4.4}$$

The fluid consistency index and the dimensionless flow behaviour index

Zhang et al. [103] determined the values of K' and n for various conditions. They measured the pressure drop of the TBAB CHS flow in a horizontal tube. The indices K' and n are related to the pressure drop by equations 4.3 and 4.4 for laminar and turbulent flows respectively. The TBAB solid mass fraction was varied between 0 and 25.0 wt%. Zhang and Ye [100] and Kumano et al. [40] also determined the indices K' and n of the power-law model to describe the non-Newtonian feature of TBAB CHS. The measurements of Zhang et al. [103] are compared with the findings of other studies in figure 4.1. They concluded that the initial mass fraction of TBAB in the solution hardly affects the values of n and K'. Ma et al. [53] found that the diameter of the tube influenced the indices for type B TBAB CHS. This was due to the enhanced particle interactions for the small tube. The influence of the pipe diameter on the indices was not found for type A TBAB CHS. The correlation of the indices is obtained with the data of Zhang et al. [103] in figure 4.1. The fluid consistency index is described by:

$$K' = 0.004564 \exp^{8.219 w_c} \tag{4.5}$$

The dimensionless flow behaviour index is described by:

$$n = 1 - 0.7738 w_c \tag{4.6}$$

Zhang et al. [103] showed like many other authors that TBAB aqueous solution has Newtonian flow characteristics. This implicates that the flow behaviour index of TBAB aqueous solution ($w_c = 0$) should be 1. However, since the linear fit of the measurements of Zhang et al. does not give $n = 1$ for $w_c = 0$, the linear fit is adjusted to meet this criterion.

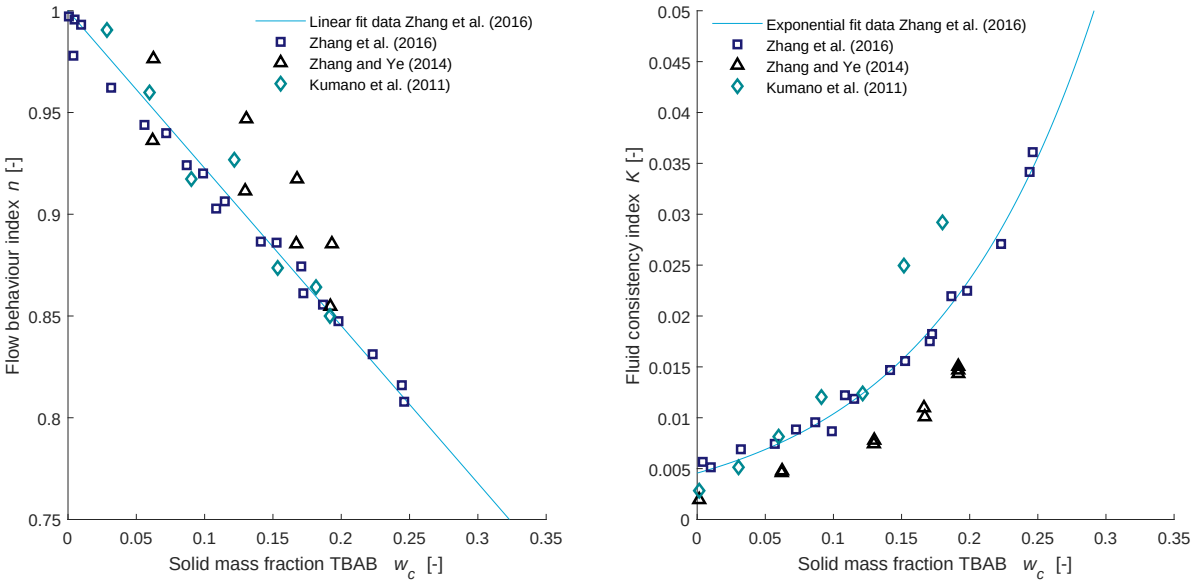

Figure 4.1: The fluid consistency index and the dimensionless flow behaviour index of type A TBAB CHS [40, 102, 103].

Modified Reynolds number

Xiao et al. [95] also studied the rheological behaviour of TBAB hydrate slurry. They rewrote the equation of the modified Reynolds number for power law fluids under the no-slip boundary condition for a laminar flow.

$$Re_{mod} = \frac{\rho v d}{\mu_0[(3n+1)/4n]^n (8v/d)^{n-1}} \tag{4.7}$$

They also measured the pressure drop of TBAB CHS flow in a 2 meter long tube with an internal diameter of 21 mm. They conducted the measurements for TBAB CHS for different solid volume fractions and initial TBAB mass fractions of 22 wt% and 30 wt%. They determined the flow behaviour index n and the apparent viscosity of TBAB CHS with the pressure drop measurements. They found the following relation for the flow behaviour index:

$$n = -2.7\phi_c + 1 \tag{4.8}$$

They also found that under the same solid mass fraction, the apparent viscosity increases with increasing initial concentration.

$$\mu_{app} = 0.8\phi_c^2 + 0.02\phi_c + 0.0036 \quad for \quad w_{0,TBAB} = 0.22 \tag{4.9}$$

$$\mu_{app} = 0.7\phi_c^2 + 0.07\phi_c + 0.0112 \quad for \quad w_{0,TBAB} = 0.30 \tag{4.10}$$

Song et al. [82] also introduced the modified Reynolds number to describe the TBAB CHS flow. They defined the dimensionless Reynolds number according to the Metzner-Reed definition [58].

$$Re_{mod} = \frac{d\rho v}{\mu_{ef}} \tag{4.11}$$

TBAB CHS was treated as a Bingham fluid. The effective viscosity in the equation of the modified Reynolds number is defined as:

$$\mu_{ef} = \frac{d\Delta P/(4L)}{8v/d} = \frac{\tau_w}{8v/d} \tag{4.12}$$

They measured the pressure drop, flow velocity and solid mass fraction to describe the rheological behaviour

of TBAB CHS. They produced Type A TBAB CHS in a plate heat exchanger with solid mass fractions ranging from 0 to 22.2 wt%. The pressure drop was measured in the test tube of 27 mm with a flow velocity between 0.2 and 1.7 m/s. Figure 4.2 shows the results of their experiments. From the experimental data of Song et al. the modified Reynolds number can be determined for a certain solid mass fraction with equation 4.11 and equation 4.12. In this manner, the experimental data of Song et al. shows the influence of the solid mass fraction on the modified Reynolds number.

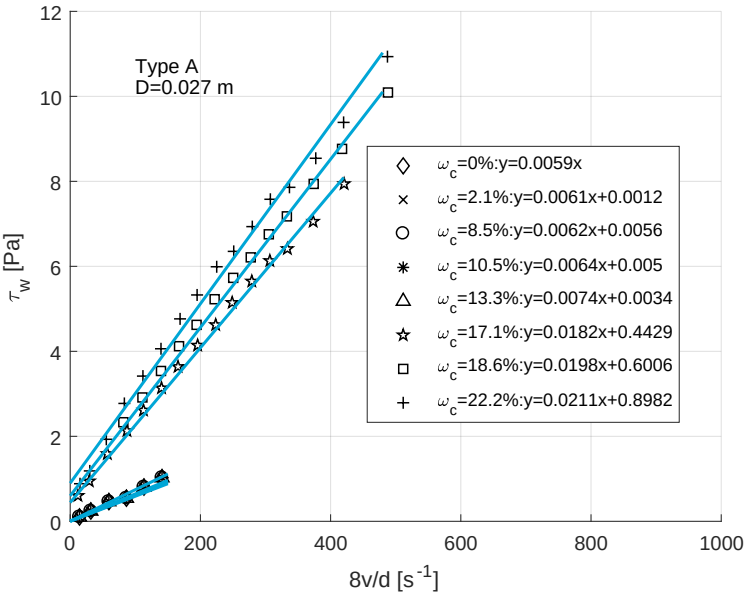

Figure 4.2: Shear stress measurements of Song et al. for different solid mass fractions and flow velocities [82].

Comparison of the models

For comparison, the modified Reynolds number is calculated according to the methods of the different studies for a tube diameter of 10 mm and a flow velocity of 0.5 m/s. This diameter and flow velocity are commonly encountered in the pilot plant. Figure 4.3 shows the modified Reynolds number for two different initial mass fractions. The figure shows that the correlations of Xiao et al. [95] and Zhang et al. [103] show the relaminarization of the TBAB CHS correctly. Due to the relaminarization of the TBAB CHS, the modified Reynolds number should only decrease for increasing solid mass fractions. The correlation of Xiao et al. shows a decreasing modified Reynolds number for an increasing solid mass fraction, but after a certain solid mass fraction the modified Reynolds number starts to increase. This effect is even more present for higher initial mass fractions. This phenomenon does not illustrate the relaminarization effect correctly. Also, the correlation of Xiao et al. does not give a reasonable estimation of the modified Reynolds number for a solid mass fraction of $w_c = 0$. For this solid mass fraction, the modified Reynolds number should be equal with the Reynolds number of the solution and the Reynolds number of the slurry.

The graphs also show no difference between the modified Reynolds number and the normal Reynolds number of the slurry. At higher solid mass fractions, the difference between the modified Reynolds number and the Reynolds number of the slurry starts to deviate more. This is because the only difference between the modified Reynolds number and the normal Reynolds number is that the modified Reynolds number also accounts for non-Newtonian fluid behaviour. The non-Newtonian fluid behaviour of TBAB CHS increases with increasing solid mass fraction and this is noticeable from the graphs.

As mentioned before in section 4.2 the modified Reynolds number depends on the flow behaviour index and the fluid consistency index. Since TBAB aqueous solution behaves as a Newtonian fluid, the flow behaviour index is 1 for a solid mass fraction of 0. As a result, the fluid consistency index should depend on the initial mass fraction of the TBAB aqueous solution because when the flow behaviour index is 1, the fluid consistency index represents the viscosity in equation 4.2. This finding is supported by Xiao et al. [95] and Zhang et al [103]. They stated that the fluid consistency index slightly differs for a different initial mass fraction and that this can be attributed to the difference between the viscosities of TBAB aqueous solutions at different initial mass fractions. The influence of the initial mass fraction of TBAB in the solution on the fluid consistency in-

dex is described with a correction factor. Equation 4.13 shows the fluid consistency index with the correction factor.

$$K' = \left[15.2759 w_{0,TBAB}^3 - 0.4701 w_{0,TBAB}^2 + 1.7108 w_{0,TBAB} + 0.2688\right] 0.004564 \exp^{8.219 w_c} \tag{4.13}$$

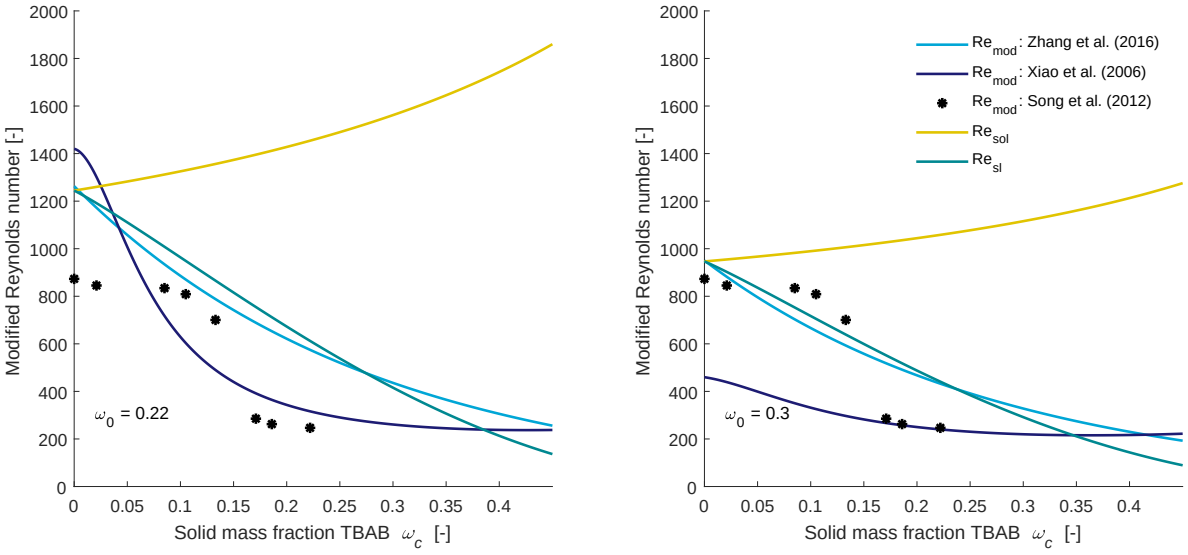

Figure 4.3: Comparison of the different Reynolds number models with the Reynolds number of the solution and the slurry [82, 95, 103].

4.3. The pressure drop of TBAB CHS flowing in straight tubes

Several studies have been carried out to describe the pressure drop of TBAB CHS flowing through a tube. In all of the studies mentioned in section 4.2 the pressure drop was measured in small smooth tubes. The authors used their measurements to determine correlations for the friction factor of TBAB type A CHS pipe flow. An overview of these correlations is shown in table 4.1. Almost all authors are using the modified Reynolds number and Poiseuille's law to calculate the friction factor in the laminar regime. The authors proposed different correlations for the friction factor in the turbulent flow regime. At the critical Reynolds, number the flow transition from laminar to turbulent occurs. The transition from laminar to turbulent does not occur for one specific Reynolds number, but for a range of Reynolds numbers. The critical value depends on a number of other factors, for instance pipe roughness, flow uniformity, crystal particle size and solid mass fraction. In the transition region the flow is neither completely laminar nor completely turbulent. Kumano et al. [41] found that the relation between the critical Reynolds number and critical solid fraction is independent of the hydrate type and the tube diameter and that the critical Reynolds number increases with increasing solid mass fraction. Table 4.1 also shows the range of Reynolds numbers at which the authors observed the flow transition.
Figure 4.4 shows the friction factor correlation of Darcy-Weisbach for the laminar flow regime and the friction factor correlations of the different authors for the turbulent flow regime. Also, the measurements of Zhou et al. [105] are included in the figure. In figure 4.4, the friction factor is plotted against the modified Reynolds number. The correlation of Zhang et al. does not correspond with the other correlations. Zhang et al. used the semi-empirical correlation for fully developed turbulent flows for non-Newtonian fluids of Dodge and Metzner [18], while the other authors fitted experimental data to find an empirical relation. Another problem with the correlation of Zhang et al. is that they only validated the correlation for modified Reynolds numbers till 4000 and for a very small tube diameter. Their equation of the friction factor also needs to be solved iteratively. This can slow down the model.

Table 4.1: An overview of the correlations of the friction factors of TBAB CHS pipe flow.

Authors	Correlations	Critical regime $[Re_{mod}]$
Song et al. [82]	laminair: $f = \frac{64}{Re_{mod}}$ turbulent: $f = 4 \times 0.1021 Re_{mod}^{-0.2708}$	$2000 - 2300$
Xiao et al. [94]	laminair: $f = \frac{64}{Re_{mod}}$ turbulent: $f = 4 \times 0.3226 Re_{mod}^{-0.4271}$	
Zhang and Ye [102], Zhang et al. [103] and Ma and Zhang [51]	laminair: $f = \frac{64}{Re_{mod}}$ turbulent: $\frac{1}{\sqrt{f}} = \frac{2.0}{n^{0.75}} \log\left(Re_{mod}\sqrt{f}\frac{2-n}{2}\right) - \frac{0.2}{n^{1.2}}$	$1500 - 1900$ for $d = 2.0\ mm$ $1400 - 1900$ for $d = 4.5\ mm$
Kumano et al. [40]	laminair: $f = \frac{64}{Re_{mod}}$ turbulent: $f = 0.3164 Re_{sol}^{-1/4}$	$0 < Re_{mod}/Re < 0.5$ $0.5 < Re_{mod}/Re < 1$
Zhou et al. [104, 105]	laminair: $f = \frac{64}{Re_{mod}}$ turbulent: $f = \frac{0.3164}{Re^{0.25}}$	$Re \leq 2300$ $Re > 2300$
Darbouret et al. [17]	laminair: $f = \frac{64}{Re_{mod}}\left(1 + \frac{Bm}{6}\right)$ turbulent: - with $Bm = \frac{\tau_0 d}{\mu_0 v}$	

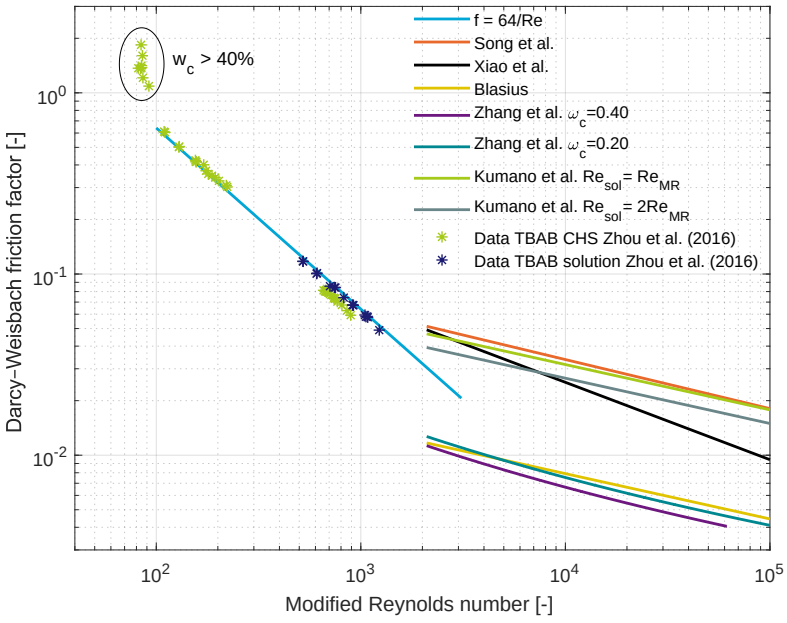

Figure 4.4: Comparison of the different friction factor correlations and the measurements of Zhou et al. [40, 82, 94, 102, 105].

The correlation of Kumano et al. for the turbulent regime uses the normal Reynolds number with the properties of the liquid phase in the slurry. The Reynolds number of the solution can be twice as large as the modified Reynolds number of the slurry for high solid mass fractions [40]. Therefore, the friction factor of Kumano et al. can lie anywhere between the two lines of the correlation of Kumano et al. in the graph.
The friction factor correlation of Zhang et al. also differs from the other correlations. The graph shows that the friction factor of Zhang et al. becomes initially smaller when the flow becomes turbulent. This is not in agreement with the other correlations since the friction factors of the other correlations become initially

larger when the flow becomes turbulent. The correlations based on empirical data are preferable since they are in better agreement with the experimental data. Also, the friction factor correlation of Zhang et al. is implicit. This makes the model slower, since the equation needs to be solved iteratively. However the Blasius equation could be used alternatively, since this explicit correlation resembles the correlation of Zhang et al..

The correlations of the friction factors are compared with the experimental data of Xiao et al. [94, 95] and Ma et al. [53] in order to determine the most suitable correlation for the present model. The correlations differ from each other for the friction factor in the turbulent flow regime and in the prediction of the critical Reynolds number. The pressure drop of TBAB CHS flow through a straight tube with an internal diameter of $d_i = 0.006$ for different solid mass fractions and velocities are measured by Ma et al.. Xiao et al. used an internal tube diameter of $d_i = 0.021$. Figure 4.5 compares the correlations with the experimental data of Xia et al.. The following observations can be made from figure 4.5.

- The correlation of Song et al. predicts the pressure drop quite accurate. The correlation of Song et al. predicts a slightly higher pressure drop in the turbulent flow regime.
- The correlation of Xiao et al. predicts the pressure drop the most accurately. The correlation of Xiao et al. predicts a slightly higher pressure drop in the turbulent flow regime.
- The correlation of Zhang et al. predicts initially a lower pressure drop when the flow becomes turbulent. However, the experimental data do not show this behaviour.
- The solid mass fraction has little influence in the turbulent flow region on the pressure drop. Also, the correlations of Kumano et al. and Zhou et al. do not show a distinct influence of the solid mass fraction on the pressure drop in the turbulent flow regime. This is because the correlations of Kumano et al. and Zhou et al. use the normal Reynolds number with properties of the solution to calculate the friction factor in the turbulent flow regime. The solid mass fraction has almost no influence on the Reynolds number of the solution.
- The correlations are not able to predict the critical Reynolds number accurately.
- The correlations which use the modified Reynolds number predict the pressure drop in the laminar flow regime the most accurate. The correlations with the modified Reynolds number are able to distinguish the pressure drop for different solid mass fractions.

The turbulent TBAB CHS flow can become laminar when the solid mass fraction of the slurry increases. This behaviour can be easily observed when the pressure drop of the slurry flow is measured for increasing solid mass fraction. Figure 4.6 shows that the correlations of Song et al.,Xiao et al. and Kumano et al. can predict the pressure drop of the slurry for increasing solid mass fraction the most accurate. The only correlation which can predict the critical Reynolds number is the correlation of Kumano et al.. However, the criteria of Kumano et al. for the flow to be turbulent is not without any drawbacks. For low solid fractions the Reynolds number of the solution is almost the same as the modified Reynolds number. This implicates that the flow is turbulent for low solid mass fractions, even when the Reynolds number of the flow is very small.

Figure 4.6 shows the pressure drop predicted using the different friction factor correlations for different flow velocities and increasing solid mass fractions. The correlations are compared with the measurements of Ma et al. [53]. The following additional observations can be made from this graph.

- The velocity has more influence on the pressure drop than the solid mass fraction.
- The correlation of Song et al. and Xiao et al. predict the pressure drop of the slurry flow the most accurately as mentioned before.

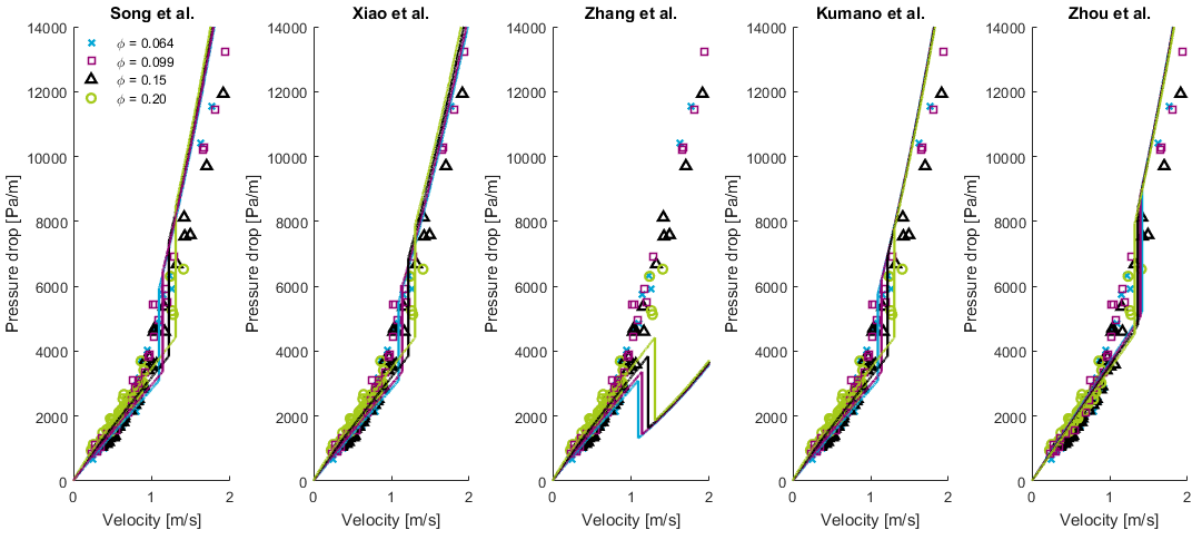

Figure 4.5: Comparison of the pressure drop correlations in a straight tube with $d_i = 0.021m$ and $w_0 = 0.30$ with the experimental data of Xiao et al. [94, 95] for different solid mass fractions.

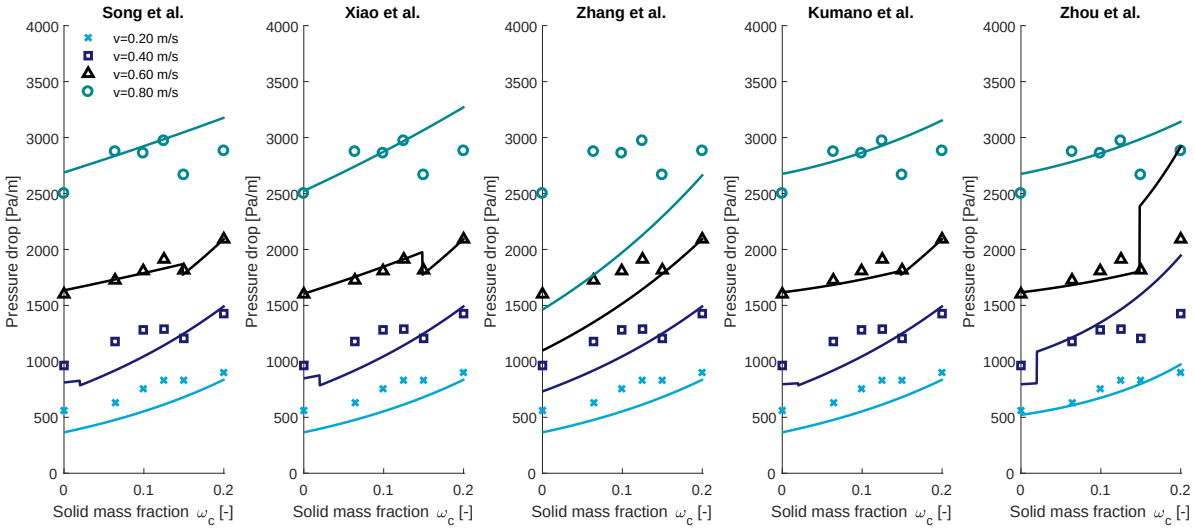

Figure 4.6: Comparison of the pressure drop correlations in a straight tube with $d_i = 0.006m$ with the experimental data of Ma et al. [53] for different velocities.

The correlation of Kumano et al. provides a prediction of the critical Reynolds number which is different for a varying solid mass fraction. However, the prediction of the critical Reynolds number is only valid for a limited range of solid mass fractions and the correlation of Kumano et al. does not show a distinct influence of the pressure drop in the turbulent flow regime for varying solid mass fractions. In consequence the correlation of Xiao et al. for the friction factor is assumed to be the most suitable correlation for the current model.

4.4. Heat transfer characteristics of TBAB CHS

Kumano et al. [41] measured the Nusselt number of melting TBAB CHS for different solid mass fractions. They compared the measured Nusselt number with a theoretical expression for the Nusselt number. For the turbulent flow, the measured Nusselt numbers matched with the calculated Nusselt numbers at low solid fractions. It was found that the Nusselt number of TBAB CHS at low solid fractions corresponded to the Nusselt number of TBAB solution, since the theoretical values of the Nusselt number were calculated with the Colburn's equation based on the TBAB solution. From the measurements of the laminar flow they proposed a correlation based on the modified Reynolds number, the solid mass fraction, tube diameter and Prandtl

number. The Prandtl number is defined as the ratio of momentum diffusivity to thermal diffusivity:

$$Pr = \frac{c_p \mu}{\lambda} \tag{4.14}$$

The heat transfer of melting TBAB in tubes is investigated by several authors. All the authors proposed an empirical correlation to describe the Nusselt number. Table 4.2 gives an overview of the empirical correlations of the Nusselt number of the different authors. These different correlations are compared with the measurements of Kumano et al. [41]. The measurements of the Nusselt number for different solid mass fractions are conducted for a Reynolds number of $Re = 1000$ and $Re = 2500$ in a straight tube with a diameter of $d_i = 0.075\ m$. The initial mass fraction was 22.5 wt% and the flow rate was controlled to maintain a constant Reynolds number throughout the measurements.

Table 4.2: An overview of the correlations for the Nusselt number of melting TBAB CHS in tubes.

Authors	Correlations	Regime
Song et al. [93]	$Nu = 1.231 \times 10^{-5} Re_{mod}^{1.6606} Pr^{0.7073}$	laminar
	$Nu = 5.254 \times 10^{-4} Re_{mod}^{0.9097} Pr^{1.1202}$	turbulent
Kumano et al. [41]	$Nu = 3.33 \left(Re_{mod} Pr \frac{d_i}{x} \right)^{0.18} w_c^{0.42} \left(\frac{d_i}{d_p} \right)^{0.55}$	laminar $120 \leq Gz_{mod} \leq 4300$
		$0.03 \leq w_c \leq 0.18$
	$Nu = 0.023 Re^{0.8} Pr^{1/3}$	turbulent
Ma and Zhang [51]	$Nu = 0.0598 Re_{mod}^{0.711} Pr^{1/3} \left(1 + \frac{\Delta w_c \Delta h_{melt}}{c_p \Delta T} \right)^{0.457}$	$0.10 < w_c < 0.25$
Edwards et al. [21]	$Nu = 3.66 + \frac{0.065 \frac{d_i}{L} RePr}{1 + 0.04 \left(\frac{d_i}{L} RePr \right)^{2/3}}$	laminar

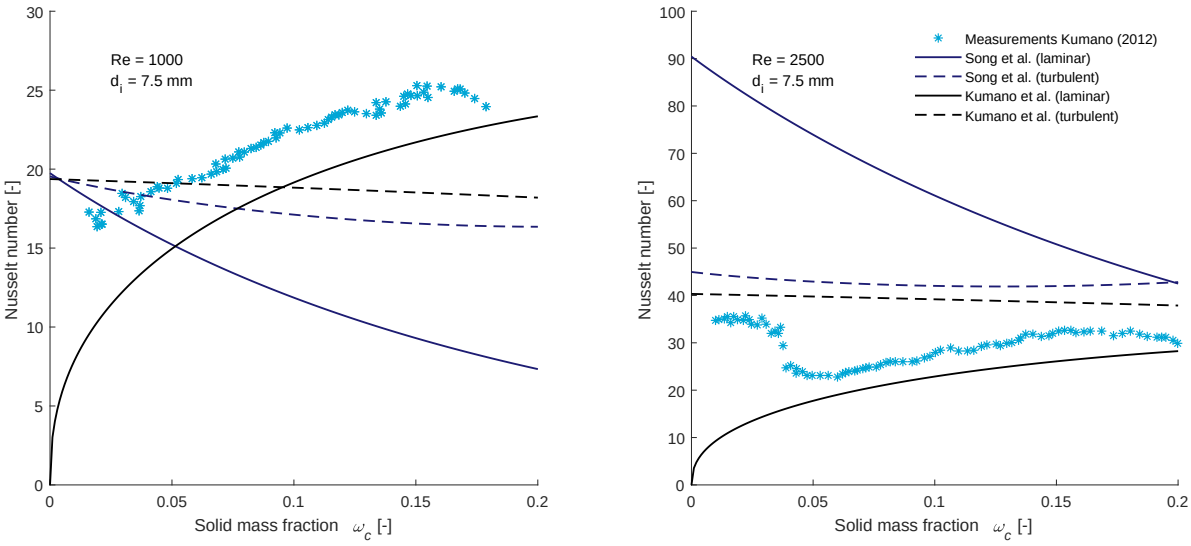

Figure 4.7: The Nusselt number correlations compared with experimental data of Kumano et al. [41].

Figure 4.7 compares the Nusselt number correlations with the measurements of Kumano et al. for two different conditions. The measurements show a drop in the Nusselt number for a solid mass fraction of 0.04 for a Reynolds number of 2500. The sudden drop of the Nusselt number is caused by the relaminarization effect in the slurry flow. The solid lines in figure 4.7 represent the Nusselt number correlations for a laminar flow and the dotted lines for a turbulent flow. The correlation of Kumano et al. [39, 41] has a deviation from the experimental data for the Reynolds number of 1000 and 2500 of around 20%. The paper of Kumano et al.

shows a better match between the data and the correlations. The difference between the results in the paper and in figure 4.7 is caused by the different correlations for the determination of the properties of the slurry. Kumano et al. [39] and Song et al. [93] have measured the heat transfer coefficient. The convective heat transfer coefficient can be expressed as a function of the Nusselt number:

$$\alpha = \frac{Nu\lambda_{sl}}{d_i} \tag{4.15}$$

The experimental data of Song et al. [93] are compared with the convective heat transfer coefficients following from the different correlations of the Nusselt number. During the measurements of Song et al. the hydrate crystals were formed from a solution with an initial TBAB mass concentration of 30.0 wt%. The slurry flowed through a stainless steel tube with a length of 2.8 m, an inside diameter of 14 mm and a wall thickness of 1 mm. A constant heat flux was exposed against the tube wall to measure the heat transfer coefficient. Figure 4.8 and figure 4.9 show a comparison between the heat transfer coefficient correlations and the experimental data. Figure 4.8 also shows the heat transfer coefficient for high flow velocities. Although high velocities are not expected in the system, the crystal layer in the generator could decrease the flow passage area, which could potentially increase the flow velocity drastically. From both figures, the following observations can be made:

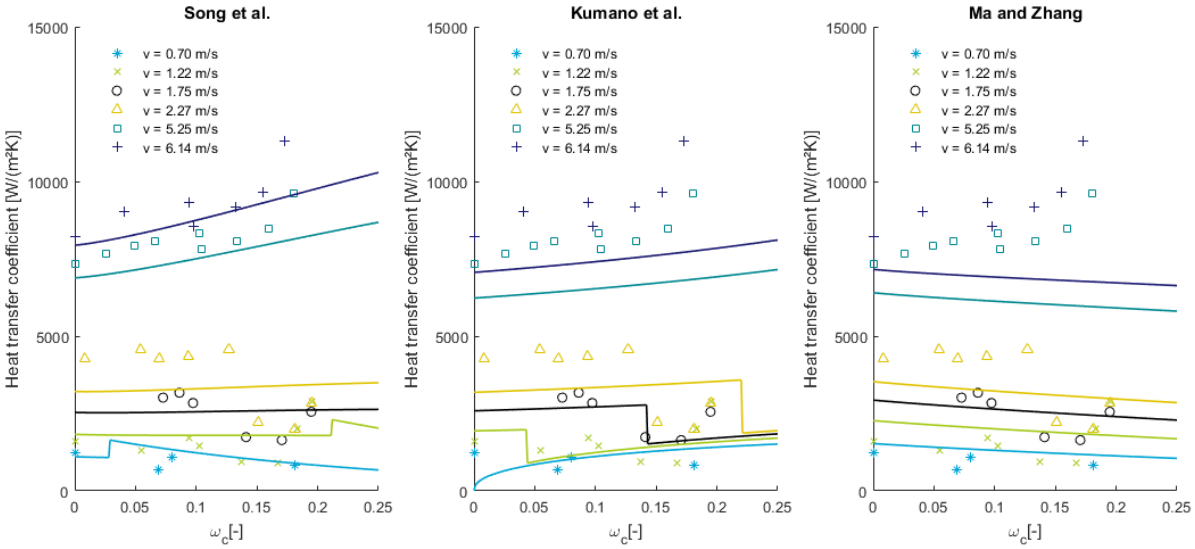

Figure 4.8: Comparison of the heat transfer coefficient correlations with experimental data of Song et al. [93] for increasing solid mass fraction and different velocities.

- All three models provide a reasonable result for the heat transfer coefficient at low velocities. Both for a laminar flow (v = 0.70 m/s) and turbulent flow regime (v = 1.22, 1.75, 2.27, 5.25 and 6.14 m/s).
- The model of Ma and Zhang predicts a negative influence of the solid mass fraction on the heat transfer coefficient for all velocities. Nevertheless, the experimental data shows a slightly positive correlation between the solid mass fraction and the heat transfer coefficient at high velocities.
- The models of Song et al. and Kumano et al. show a positive correlation between the solid mass fraction and the heat transfer coefficient at higher velocities, which is supported by the experimental data.
- The correlation of Song et al. provides the most accurate prediction of the heat transfer coefficient. This is expected since the correlation is created with the very same experimental data. Although the fluid properties are obtained using different correlations than Song et al. used.
- None of the models can accurately predict the relaminarization effect for all conditions.

In conclusion, the correlation of Song et al. provides the most accurate prediction of the heat transfer coefficient. The correlation has a reasonable result for all measured velocities and solid mass fractions.

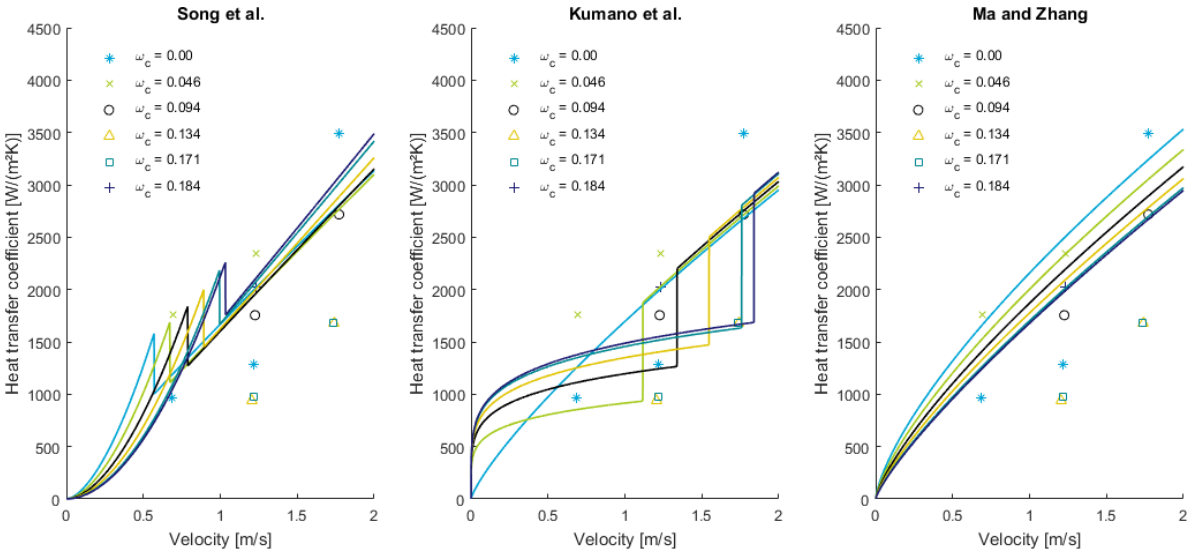

Figure 4.9: Comparison of the heat transfer coefficient correlations with experimental data of Song et al. [93] for increasing velocity and different solid mass fractions.

4.5. Pressure drop of TBAB in plate heat exchangers

The TBAB hydrate crystals are produced in a plate heat exchanger in the pilot plant. Unfortunately, only a few studies have been conducted with regard to the flow behaviour of TBAB CHS in plate heat exchangers. Ma and Zhang [49] measured the pressure drop and heat transfer characteristics of TBAB CHS flowing through a plate heat exchanger. They investigated these properties for different solid mass fractions. They proposed an empirical correlation for the flow friction factor of TBAB CHS flowing through a plate heat exchanger based on their measurements. Ma and Zhang also showed that the correlation was applicable to the case of melting TBAB CHS flow. They found that the pressure drop of 5.0-17.5 vol% TBAB CHS was always higher than the pressure drop of single phase TBAB aqueous solution and increased with increasing solid mass fraction. Due to enlarged particle-tube wall interactions, the relative error increased for higher solid mass fractions. This behaviour was also observed for the pressure drop of ice slurries in plate heat exchangers [9, 78, 79].

Ma and Zhang are the only researchers who studied the behaviour of TBAB CHS flow in plate heat exchangers. Their findings will be compared with pressure drop correlations in plate heat exchangers which are not specific for TBAB CHS flow. The pressure drop of TBAB CHS flowing through a plate heat exchanger can be attributed to three mechanisms:

- The difference in hydrostatic pressure due to a height difference between the inlet and the outlet of the plate heat exchanger.
- The pressure drop due to friction in the plate heat exchanger.
- The difference in dynamic pressure due to the difference of the flow velocity at the inlet and the outlet of the plate heat exchanger.

This report only focusses on the pressure drop due to friction in the plate heat exchanger. The pressure drop in the plate heat exchanger is caused by the pressure drop at the inlet and outlet ports of the plate heat exchanger and the pressure drop over the plates, equation 4.16.

$$\Delta P = \Delta P_{pl} + \Delta P_{pt} \tag{4.16}$$

In the literature most friction factor correlations only describe the pressure drop over the plates. In some correlations the pressure drop over the inlet and outlet ports is also taken into account. The friction factors correlations which include the pressure drop over the ports will be denoted with f while the friction factors that only included the friction over the plates will be indicated with f_p. The pressure loss over the ports is calculated when the correlation does not include this loss with the following equation [42]:

$$\Delta P_{pt} = 1.3\rho \frac{v_{pt}^2}{2} N_p \tag{4.17}$$

The friction factor of the plate heat exchanger is in most cases an empirical correlation. Table 4.3 contains several of these correlations. All of the correlations, except the correlation of Bellas et al. and Ma and Zhang, are not developed for slurries. This makes these correlations maybe not applicable for TBAB CHS flow in plate heat exchangers. However, these correlations are suitable for low Reynolds number flows. Singh and Kachhwaha [79] proposed a thermohydraulic model to predict the pressure drop of chilled water and ice slurries in a plate heat exchanger. They compared their predictions with measurements to validate their model. Bellas et al. [9] also measured the pressure drop of ice slurries with a solid mass fraction of 0 to 20 wt% in a plate heat exchanger. They used a plate heat exchanger of Alfa Laval with a hydraulic diameter of 4 mm, a plate height of 310 mm and 11 channels on each side. From their experimental data, Pronk [68] derived a correlation for the friction factor.

$$f = 46.62 Re^{-0.132} \tag{4.18}$$

Table 4.3 shows the correlations that are used to predict the pressure drop of the actual plate heat exchanger from the pilot plant. Since the chevron angle of the plate heat exchanger in the pilot plant is not specified, a chevron angle of 60° is assumed with respect to the horizontal as shown in figure 4.10. Figure 4.11 shows the different pressure drop correlations for a TBAB solution (dotted lines) and a TBAB CHS (solid lines) in a plate heat exchanger. Figure 4.11 also shows measurements of the pressure drop of a TBAB solution flowing through the plate heat exchanger in the pilot plant.

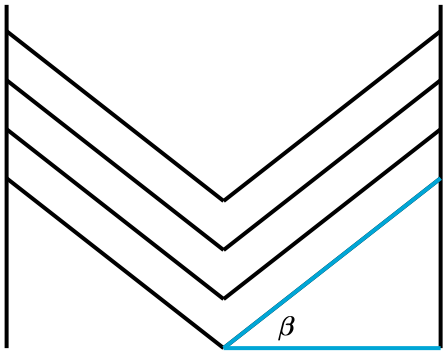

Figure 4.10: Chevron angle beta is considered with respect to the horizontal axis.

The correlation of Bellas et al. and Ma and Zhang show the largest pressure drop of all the correlations. From figure 4.11 and the correlations the following observations can be made:

- The correlation of Ma and Zhang and Bellas et al. are the only correlations which are based on slurry flow. The correlation of Bellas et al. and Ma and Zhang are based on ice slurry flow and TBAB CHS flow respectively.
- The port diameter and the chevron angle is not specified by the research of Ma and Zhang and Bellas et al.. The difference between these correlations and the other studies might also be explained by the equipment size. The other studies obtained the correlations with industrial sized equipment unlike the studies of Bellas et al. and Ma and Zhang.
- Ma and Zhang [49] reported a pressure drop increase from about 30 to 45 kPa for an increasing solid volume fraction of 0 to 0.175. Bellas et al. found [9] a pressure drop increase from 47 to 53 kPa for an increasing ice slurry fraction from 0 to 20wt%. Based on figure 4.11 and the pressure drop increase for the increasing solid mass fractions, it can be concluded that the correlations provided by the VDI heat atlas and Sinnott and Towler are not suitable for slurries.
- The correlations of Focke et al., Thonon et al. and Kumar et al. show a relatively larger increase in pressure drop between the solution and slurry flow. This is caused by the use the normal Reynolds

number instead of the modified Reynolds number in these correlations. The difference between the modified and the normal Reynolds number can be quite significant for higher solid mass fractions. It is more suitable to use the modified Reynolds number, since the normal Reynolds number does not show the non-Newtonian behaviour correctly.

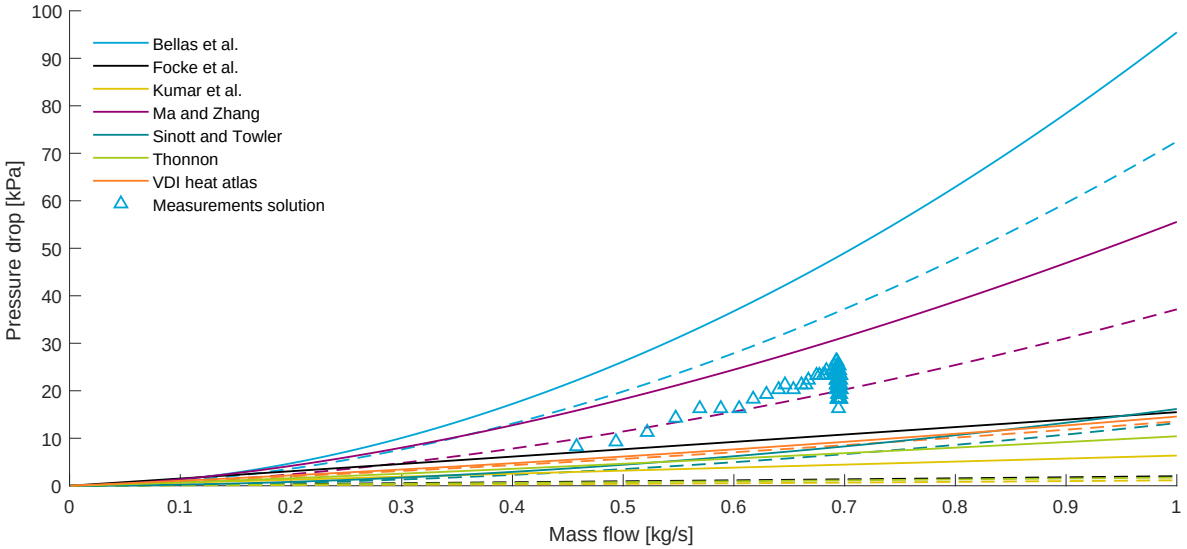

Figure 4.11: Comparison of the correlations for the pressure drop in the plate heat exchanger. The solid lines represent TBAB CHS with a solid mass fraction of $w_c = 0.40$ and the dotted lines TBAB solution. Measurements of pressure drop in the pilot plant are indicated with triangles.

4.6. Evaporation of R134A in plate heat exchangers

In the plate heat exchanger two different boiling mechanisms are present during the evaporation of the coolant: forced convection boiling and pool boiling. In pool boiling, vapour is generated at a heated wall and the motion of the fluid is induced by the boiling process itself. During forced convection boiling, the fluid flows over a heated surface and the flow is induced by an external force. It is unknown which of these two boiling processes dominates during the evaporation of a fluid in a plate heat exchanger [23]. Nevertheless, forced convection boiling is often related with high mass flows and pool boiling with high heat fluxes. The boiling process in the plate heat exchanger can also be characterized by the temperature difference between the plate surface temperature and the saturation temperature, the excess temperature. For the different ranges of temperature differences, several boiling processes can occur. The boiling processes can be divided into four different stages which result from the boiling curve [59]. These are the four boiling regimes for increasing excess temperature:

- Convection boiling: In this regime natural convection is the dominant heat transfer mechanism. The excess temperature range is between the 2 K and 4 K and due to the low heat transfer, convection boiling probably is avoided in evaporators.
- Nucleate boiling: During nucleate boiling, isolated bubbles are formed at the heat transfer surface. The bubbles sweep the hot liquid away from the heat transfer wall, resulting in a high heat transfer coefficient.
- Transition boiling: In this boiling regime the number of nucleation sites increases rapidly causing many bubbles to form. These bubbles start to merge and produce columns of vapour, which feed large slugs of vapour. This vapour layer prevents liquid from reaching the heat transfer surface. Due to the low thermal conductivity of the vapour, the heat transfer becomes smaller in this boiling regime.
- Film boiling: In this boiling regime the heat transfer surface is completely covered with a vapour film. The heat fluxes are much lower since heat is transferred poorly across the vapour film. When the temperature level of the heat transfer surface becomes high enough, radiation heat transfer can become significant across the vapour film.

Table 4.3: An overview of the friction factor correlations for plate heat exchangers with a 60° chevron angle.

Authors	Correlations	Regime
Bellas et al. [9]	$f = 46.62Re^{-0.132}$	
Focke et al. [25]	$57.5/Re + 0.093$	$120 < Re < 1000$
	$0.8975/Re^{0.263}$	$1000 < Re < 42000$
Kumar et al. [42]	$f = 24.0/Re$	$Re < 40$
	$f = 3.24/Re^{0.457}$	$40 \leq Re \leq 400$
	$f = 0.760/Re^{0.215}$	$Re > 400$
Ma and Zhang [49]	$f = \frac{51.002}{Re_{mod}^{0.3}}$	$60 \leq Re_{mod} \leq 400$
		$0.05 \leq \phi \leq .175$
Sinnott and Towler [80]	$f = 4.8Re^{-0.3}$	
	$\Delta p_{pt} = 1.3\rho\frac{v_{pt}^2}{2}$	
Thonon [84]	$26.34Re^{-0.830}$	$Re \leq 550$
	$0.572Re^{-0.217}$	$Re > 550$
VDI Heat Atlas [89]	$f_0 = 64/Re$	$Re < 2000$
	$f_{1,0} = 597/Re + 3.85$	
	$f_0 = (1.8ln(Re) - 1.5)^{-2}$	$Re \geq 2000$
	$f_{1,0} = 39/Re^{0.289}$	
	$\frac{1}{\sqrt{f}} = \frac{cos(\beta)}{\sqrt{0.18tan(\beta) + 0.36sin(\beta) + f_0/cos(\beta)}} + \frac{1 - cos(\beta)}{\sqrt{f_{1,0}}}$	

In the plate heat exchanger of the pilot plant nucleate boiling and transition boiling are expected to be the dominant boiling mechanisms. The convective boiling regime will be avoided due to the low overall heat transfer coefficient. Also, the excess temperature in the plate heat exchanger will not be high enough to facilitate film boiling. Donowski and Kandlikar compared several theoretical and empirical correlations for the evaporation heat transfer coefficient of the refrigerant R-134a flowing through a plate heat exchanger [19]. They found that the correlation schemes proposed by Yan and Lin [96] for evaporation of refrigerant R-134a results in large discrepancies with their own measurements. Donowski and Kandlikar used the data of the experiment of Yan and Lin to improve the correlation of the phase evaporation heat transfer coefficient of R-134a. The new correlation provides an accurate fit to the experimental data of Yan and Lin. Nucleate boiling of a refrigerant in a plate heat exchanger is also described by Amalfi et al. [3, 4], Huang et al. [32] and Longo and Gasparella [48]. Table 4.4 gives an overview of these heat transfer correlations of the refrigerant R-134a. Palmer et al. [66] reported two separate correlations for different types of refrigerant. They stated that the need for two different correlations was attributable to the use of different types of lubricants. Most of the heat transfer correlations of refrigerants in an evaporator use dimensionless number. These dimensionless numbers include the equivalent boiling number:

$$Bo_{eq} = \frac{\dot{Q}_w/A}{G_{eq}\Delta h_{liq,G}} \tag{4.19}$$

The equivalent mass flux:

$$G_{eq} = G\left((1 - X_m) + X_m\left(\frac{\rho_{liq}}{\rho_G}\right)^{0.5}\right) \tag{4.20}$$

Table 4.4: An overview of the Nusselt number correlation for the evaporation of the refrigerant in a plate heat exchanger.

Authors	Correlations	Regime
Amalfi et al. [3, 4]	$Nu = 982\left(\frac{\beta}{70°}\right)^{1.101}\left(\frac{G^2 d_h}{\rho_m \sigma}\right)^{0.135}\left(\frac{\rho_{liq}}{\rho_G}\right)^{-0.224} Bo^{0.320}$	$Bd < 4$
	$Nu = 18.495\left(\frac{\beta}{70°}\right)^{0.248}\left(\frac{X_m G d_h}{\mu_G}\right)^{0.135}\left(\frac{G d_h}{\mu_{liq}}\right)^{0.351}\left(\frac{\rho_{liq}}{\rho_G}\right)^{0.223} Bd^{0.235} Bo^{0.320}$	$Bd \geq 4$
	$Bd = \frac{g(\rho_{liq} - \rho_G) d_h^2}{\sigma}$	
Han et al. [29]	$\alpha = Ge1 Re_{eq}^{Ge2} Bo_{eq}^{0.3} Pr^{0.4}$	
	$Ge1 = 2.81\left(\frac{b}{d_h}\right)^{-0.041}\left(\frac{\pi}{2} - \frac{\beta}{180}\pi\right)^{-2.83}$	
	$Ge2 = 0.746\left(\frac{b}{d_h}\right)^{-0.082}\left(\frac{\pi}{2} - \frac{\beta}{180}\pi\right)^{0.61}$	
Huang et al. [32]	$Nu = 1.87 \times 10^{-3}\left(\frac{Q_w/A}{\lambda_{liq} T_{sat}}\right)^{0.56}\left(\frac{\Delta h_{liq,G} d_o \rho_{liq}^2 c_p L^2}{\lambda_{liq}^2}\right) Pr_{liq}^{0.33}$	
	$d_o = 0.0146 \times 35°\left(\frac{2\sigma}{g(\rho_{liq} - \rho_G)}\right)^{0.5}$	
Longo and Gasparella [48]	$\alpha = 55\left(\frac{P}{P_{cr}}\right)^{(0.12 - 0.2 log_{10} R_p)}\left(-log_{10}\left(\frac{P}{P_{cr}}\right)\right)^{-0.55}\left(\dot{Q_w}/A\right)^{0.67} M^{-0.5}$	
Palmer et al. [66] (R22, R290 and R290/R600a)	$Nu = 2.7 Re_{liq}^{0.55} Pr_{liq}^{0.55}$	
Palmer et al. [66] (R32/R152a)	$Nu = Nu_{liq}^{0.42} Fr^{0.0088} - log_{10}(p/p_{cr}^{1.5} Co^{1.5} M^{1.5})$ $Nu_{liq} = 0.16 Re_{liq}^{0.89} Pr_{liq}^{0.4}$ $Fr = \frac{G^2}{g\rho^2 d_h}$ and $Co = \left(\frac{rho_G}{rho_{liq}}\right)^{0.5}\left(\frac{1-X}{X}\right)^{0.8}$	
Yan and Lin [96]	$Nu = 19.26 Re_{eq} Pr_{liq}^{1/3} Re^{-0.5} Bo_{eq}^{0.3}$	

The equivalent Reynolds number:

$$Re_{eq} = \frac{G_{eq} d_h}{\mu_{liq}} \tag{4.21}$$

As mentioned in section 4.4, the heat transfer coefficient can be linked to the Nusselt number by equation 4.15.

Also the pressure drop of the refrigerant in the plate heat exchanger during evaporation is investigated. The pressure drop due to friction increases with an increasing vapour fraction [23]. Since the vapour has a higher specific volume, the velocity of the vapour through the plate heat exchanger is significantly higher than the velocity of the liquid. Also, the heat flux has no significant influence on the pressure drop and the pressure drop of R-134a can be reduced by increasing the condensation pressure [96]. The pressure drop is calculated by means of the friction factor as mentioned in section 4.3.

$$\Delta P_f = f \frac{L_{pl}}{d_h} \frac{G^2}{2\rho_m} \tag{4.22}$$

Table 4.5 includes several correlations of the friction factor of the evaporating refrigerant. The correlations

mentioned in table 4.5 only include the friction factor for the frictional pressure drop between the plates of the PHE. The pressure drop due to acceleration and the pressure drop in the ports of the PHE are not included.

Table 4.5: An overview of the friction factor correlation for the evaporation of the refrigerant in a plate heat exchanger.

Authors	Correlations	Regime
Amalfi et al. [3, 4]	$f = 4 \times C \times 15.698 \left(\frac{G^2 d_h}{\rho_m \sigma}\right)^{-0.475} \left(\frac{(\rho_{liq}-\rho_G) g d_h^2}{\sigma}\right)^{0.255} \left(\frac{\rho_{liq}}{\rho_G}\right)^{-0.571}$ $C = 2.125 \left(\frac{\beta}{70°}\right)^{9.993} + 0.955$	
Han et al. [29]	$f = Ge3 Re_{eq}^{Ge4}$ $Ge3 = 64.710 \left(\frac{b}{d_h}\right)^{-5.27} \left(\frac{\pi}{2} - \frac{\beta}{180}\pi\right)^{-3.03}$ $Ge4 = -1.314 \left(\frac{b}{d_h}\right)^{-0.62} \left(\frac{\pi}{2} - \frac{\beta}{180}\pi\right)^{-.47}$	
Huang et al. [32]	$f = \frac{3.81 \times 10^4 F_{r,f}}{Re_{pt}^{0.9} (\rho_{liq}/\rho_G)^{0.16}}$ $Re_{pt} = \frac{G d_h}{\mu}$ and $F_{r,f} = 0.183 \left(\frac{\beta}{30°}\right)^2 - 0.275 \frac{\beta}{30°} + 1.10$	
Yan and Lin [96]	$f = 4 \times 6.947 \times 10^5 Re_{eq}^{1.109} Re^{-0.5}$ $f = 4 \times 31.21 Re_{eq}^{0.04557} Re^{-0.5}$	$Re_{eq} < 6000$ $Re_{eq} \geq 6000$

4.7. Conclusion

This chapter discussed some heat transfer and pressure drop correlations of TBAB and the refrigerant R-134a. The non-Newtonian behaviour of the TBAB CHS is often described in these correlations by the modified Reynolds number. In order to calculate the modified Reynolds number in the current model, equation 4.13 and equation 4.6 will be used for the fluid consistency index and the flow behaviour index respectively.

The pressure drop of TBAB CHS flowing through straight tubes is best described by the correlation of the frication factor of Xiao et al. [94, 95]. Unfortunately, none of the investigated correlations provides an accurate prediction of the critical Reynolds number at which the relaminarization effect occurs. The relaminarization effect is observed when the solid mass fraction is increased.

Also, the heat transfer coefficient of melting TBAB CHS has been measured by different researches. Some of the proposed correlations provide an accurate estimation of the Nusselt number, even at higher velocities. At high velocities the solid mass fraction tends to have a positive effect on the heat transfer coefficient. This behaviour is supported by the correlations of Song et al. [93] and Kumano et al. [41].

The correlation of Ma and Zhang [49] describe the pressure drop of a TBAB solution of a TBAB CHS flowing through a plate heat exchanger the most accurately. The correlation of Ma and Zhang also matches the measurements of the pilot plant.

The evaporation of the refrigerant in a plate heat exchanger is also described by several correlations. The most suitable correlation should be selected by a comparison of the correlations with the experimental data of the pilot plant.

5

Modelling of the TBAB air conditioning system

This chapter gives an overview of models that are used to model the TBAB air conditioning system. Zak [98] developed already a model of a general TBAB air conditioning system for large office buildings. This model has been used as a starting point to develop a new model which describes the characteristics of the pilot plant by Pronk [68]. This model is already validated for water as a working fluid in the pilot plant by Pronk. This model will be further improved with the most suitable correlations for the pilot plant with TBAB aqueous solution as a working fluid. The model is developed in Matlab [54]. In this chapter the correlations and equations used to model each component are discussed.

5.1. Air cooler

The hydrate slurry is delivered to the application side of the air conditioning system by making use of an air cooler. The air cooler in the pilot plant is placed at the utilization side of the system. Appendix A contains the specifications of the air cooler provided by the manufacturer. The air cooler cools down the air to a certain temperature level that is then delivered to the room. The air is cooled down by heat exchange with the TBAB hydrate slurry. During this process, the air cools down while the TBAB slurry melts. The air cooler consist out of a header from which the TBAB CHS is distributed into 15 parallel circuits, see figure 5.3a. Each circuit consists out of two columns and six rows. The tubes of a circuit are connected to each other with bends. To increase the heat transfer area of the air cooler, the tubes are connected to aluminium sheets. These aluminium sheets give each tube square fins, see figure 5.3b. When the room needs to be cooled, air is blown over the finned tubes and is cooled down by the melting TBAB CHS. Table 5.1 shows the dimensions of the finned tubes in the pilot plant. The square fins have a width and a height of 25 mm, see figure 5.3c.

Table 5.1: Dimensions of the tubes of the air cooler.

Property	Value	Unit	Symbol
Number of tubes	180	-	N_t
Number of circuits	15	-	–
Tube length	0.6	m	L_t
Outer tube diameter	10.12	mm	d_o
Tube wall thickness	0.4	mm	δ
Internal area	3.16	m²	A_i
External area	31.95	m²	A

Figure 5.1: A segment of the pilot system in Twello before the application of the insulation material. The air cooler is visible in the top with two exposed headers and exposed bends. Two blue peripheral pumps are placed on the ground. The generator stands next to the pumps. Grey tubes connect the various components to each other. Also, the sensors with yellow labels are visible. The sensors are mainly placed in the middle of the connecting pipes.

Figure 5.2: A segment of the pilot system in Twello before the application of the insulation material. At the left, the white storage vessel is visible which contains the majority of TBAB solution/slurry. Also, the red valves and the steel air duct in the background are visible. The black sensor heads measure the pressure and are not placed at equal level.

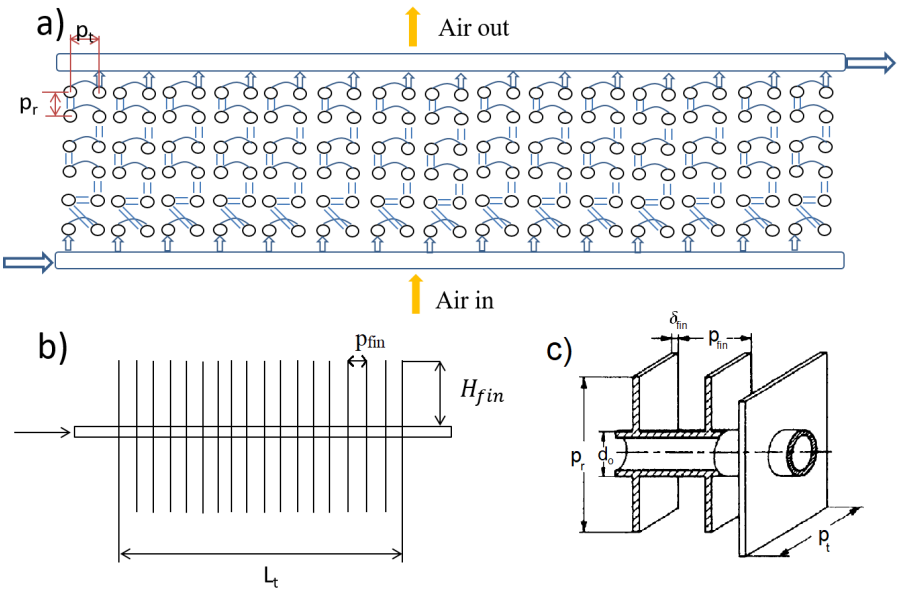

Figure 5.3: a) Tube arrangement of the air cooler. The tube pitch and row pitch are both equal and 25 mm. Therefore, the fins have a square size equal to the tube pitch and row pitch. b) Side view of a tube showing the distance between each fin. c) Detail of the square fins of a tube.

The fins are made of aluminium while the tubes of the air cooler are made of copper. A summary of the properties of the fins and the fin arrangement is given in table 5.2.

Table 5.2: Dimensions of the tube fins.

Property	Value	Unit	Symbol
Tube pitch	25	mm	p_t
Row pitch	25	mm	p_{row}
Fin pitch	4.2	mm	p_{fin}
Fin thickness	0.25	mm	δ_{fin}

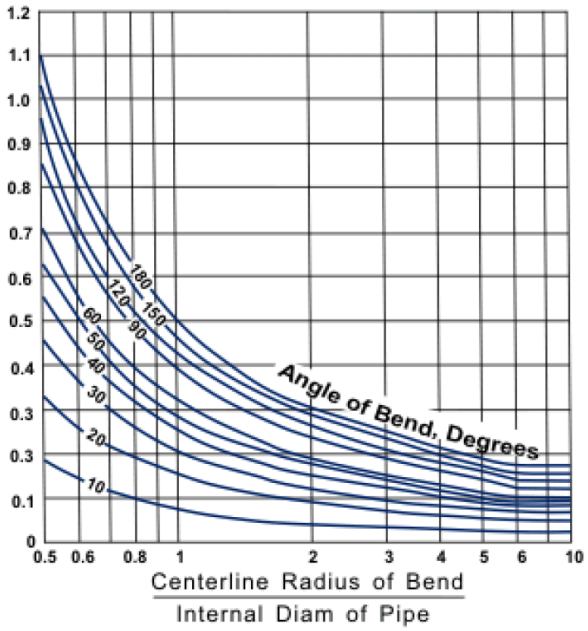

Figure 5.4: Bend loss coefficients for different angles, tube diameters and bend radii [8].

TBAB CHS side of the air cooler

The TBAB hydrate slurry is delivered to the air cooler from the storage vessel. In the air cooler the heat transfer of the melting TBAB hydrate slurry cools down the air. The heat transfer correlations of melting TBAB and the pressure drop correlations of TBAB hydrate slurry flow are already discussed in chapter 4. However, the tubes of the air cooler contain several U-bends which connect the tubes in different rows to each other. Each parallel circuit connects twelve tubes by means of eleven U-bends. These eleven U-bends will have a significant impact in the pressure drop of each circuit. Babcock and Wilcox [8] proposed a correlation which adds a bend loss coefficient to determine the pressure drop in a U-bend. The bend loss coefficient can be determined by using figure 5.4. The bend loss coefficient of the bends in the air cooler is estimated to be 0.28. The pressure drop in a single U-bend can be expressed with the following equation:

$$\Delta P = \frac{1}{2}\rho_{sl} v^2 \left(f\frac{\pi d_b}{2d_i} + \zeta_b \right) \tag{5.1}$$

Air side of the air cooler

The fins on the tubes of the air cooler increase the heat transfer area. However, the heat transfer rate does not scale proportional to the increase of heat transfer area due to the temperature gradient in the fins and the air surrounding the fins. The efficiency factor in equation 5.2 describes the influence of the fins on the heat transfer.

$$\eta_{fin} = \frac{tanh\left(H_{fin}\sqrt{\frac{2\alpha_{air}}{\lambda_{fin}\delta_{fin}}} \right)}{H_{fin}\sqrt{\frac{2\alpha_{air}}{\lambda_{fin}\delta_{fin}}}} \tag{5.2}$$

The equivalent fin height for the square fins in the pilot plant, H_{fin}, is derived from equation 5.3 from Schmidt [71] from the VDI Heat Atlas [89]. For the air cooler in the pilot plant, H_{fin}, is 12.3 mm.

$$H_{fin} = 0.5\left(2\sqrt{\frac{p_t p_{row}}{\pi}} - d_o \right)\left[1 + 0.35 ln\left(2\frac{\sqrt{\frac{p_t p_{row}}{\pi}}}{d_o} \right) \right] \tag{5.3}$$

The efficiency of the fins and heat transfer coefficient of air are used to calculate a virtual convective heat transfer coefficient in equation 5.4. This virtual connective heat transfer coefficient is used to calculate the overall heat transfer coefficient based on the outer surface of the air cooler. The virtual convective heat transfer coefficient takes the total heat transfer area and the fin efficiency into account.

$$\alpha_v = \alpha_{air}\left[\frac{A_{tube}}{A_o} + \eta_{fin}\frac{A_{fin}}{A_o} \right] \tag{5.4}$$

Then the overall heat transfer coefficient of the finned tube air cooler is defined as equation 5.5. The internal heat transfer coefficient, α_i, is calculated with the correlation of the Nusselt number of the TBAB slurry, the thermal conductivity of the slurry and the hydraulic diameter of the tube in equation 4.15 as mentioned in section 4.4.

$$\frac{1}{U_o} = \frac{1}{\alpha_v} + \frac{A_o}{A_i}\left(\frac{1}{\alpha_i} + \frac{d_i}{2\lambda_t} ln\left(\frac{d_o}{d_i} \right) + \frac{d_o}{2\lambda_{fin}} ln\left(\frac{d_o + \delta_{fin}}{d_o} \right) \right) \tag{5.5}$$

The material of the tubes is copper with a thermal conductivity of the tubes, λ_t, of 400 $W\ m^{-1}\ K^{-1}$. As mentioned before, the fins are made of aluminium. Aluminium has a thermal conductivity, λ_{fin}, of 205 $W\ m^{-1}\ K^{-1}$ at ambient conditions.

A fan blows the air through the air cooler. The pressure drop of the air flowing through the air cooler can be related to the power consumption of the fan. The air also flows through some elbow bends and straight tube sections. The pressure drop in this channel is also added to calculate the power consumption of the fan properly. The efficiency of the fan is estimated to be 55 % and the mechanical efficiency of the fan is estimated to be 95 %.

$$\dot{W} = \frac{\dot{V}\Delta P}{\eta_{mech}\eta_{fan}} \tag{5.6}$$

As mentioned in section 5.1 the tube side pressure drop will be determined with the correlations in section 4.3 for the straight tubes and equation 5.1 for the U-bends. For the air side pressure drop, the correlations from the VDI Heat Atlas [89] are taken for the calculation.

5.2. Pumps

The slurry is delivered from the storage vessel to the air cooler and the generator by two different T MAG-M peripheral pumps. Both of the mechanical driven peripheral pumps are speed controlled. The biggest pump, pump 1 (T MAG-M4), has a maximum flow rate of 2.5 m³/h with a maximum pressure drop of 5.0 bar and is used to pump the slurry through the generator. The smaller pump, pump 2 (T MAG-M2), has a maximum flow rate of 2.9 m³/h with a maximum pressure drop of 1.8 bar and is used to pump the slurry through the air cooler.

The pump characteristics of these two pumps provide the relationship between the pressure drop and the flow rate. Appendix B reproduces the pump characteristics of the two pumps provided by the manufacturer. These pump characteristics only show the performance of the pumps at 2900 rotations per minute. Since the pumps are speed controlled, the pump characteristics at other rotational speeds are also needed in the model. The affinity laws can be used to acquire the pump characteristics at these lower rotational speeds. The affinity laws require that the pumps are dynamically similar. Since the geometry of the pumps does not change, the affinity laws can be applied. The affinity laws give a relationship of flow rate for a constant impeller diameter based on the rotational speed and the flow rate at the reference state. The reference state is in this case a pump operating at 2900 rpm, the nominal rotational speed. The volumetric flow rate is proportional to the rotational speed:

$$\dot{V} = \dot{V}_{ref}\left(\frac{\omega}{\omega_{ref}}\right) \tag{5.7}$$

The head loss is proportional to the rotational speed squared:

$$\Delta P = \Delta P_{ref}\left(\frac{\omega}{\omega_{ref}}\right)^2 \tag{5.8}$$

The power is proportional to the rotational speed to the third power:

$$\dot{W} = \dot{W}_{ref}\left(\frac{\omega}{\omega_{ref}}\right)^3 \tag{5.9}$$

The efficiency of the pumps is then equal to:

$$\eta = \frac{\dot{V}\Delta P}{\dot{W}} \tag{5.10}$$

The enthalpy of the slurry after the pump is calculated with equation 5.11.

$$h_{out} = h_{in} + \frac{\dot{W}_{pump}}{\dot{m}} = h_{in} + \frac{\Delta P\dot{V}}{\dot{m}} \tag{5.11}$$

The pump efficiency is assumed to be constant by the affinity for every rotational speed. Pronk [68] proposed to construct the pump characteristic by the method of Van Putten and Colonna [88]. They predicted the head of the pump for different rotational speeds by using dimensionless analysis. The method of Van Putten and Colonna is applied to the pump characteristic provided by the manufacturer at 2900 rpm. The volumetric flow rate at different rotational speeds is calculated with equation 5.7 and the head loss with equation 5.8. Van Putten and Colonna also provided a more accurate equation to calculate the efficiency of the pump:

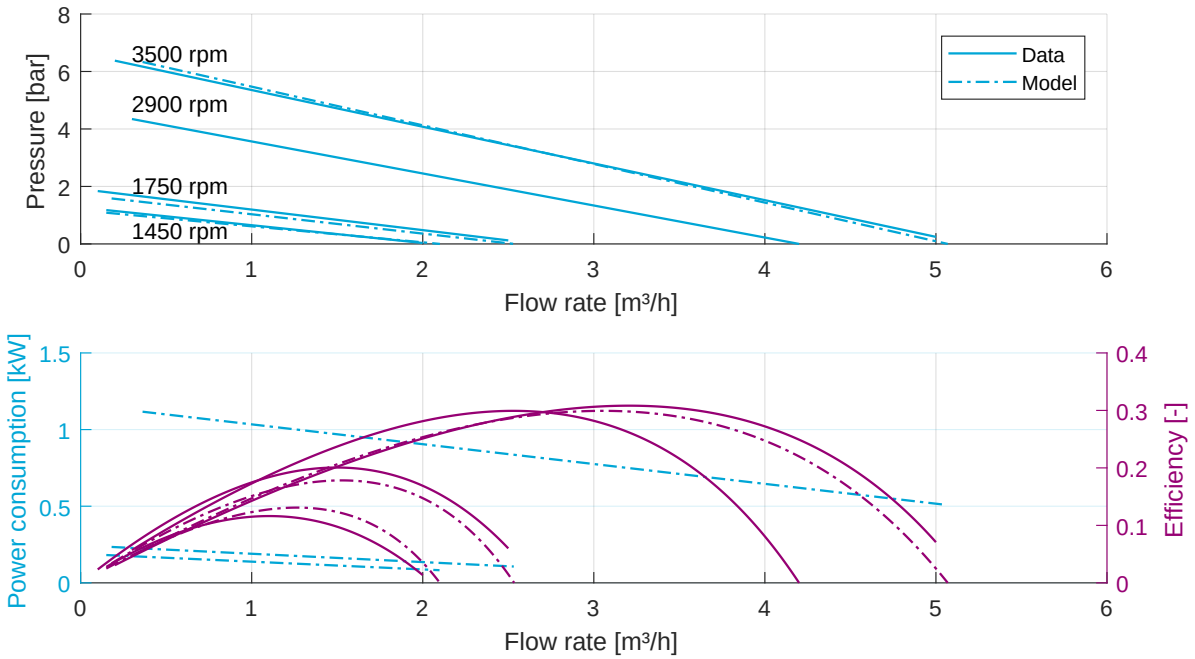

Figure 5.5: Comparison of the pump characteristics of the T MAG-M2 provided by the manufacturer and the modelled pump characteristics.

$$\eta = \eta_{ref}\left[1-\left(1-\frac{\dot{V}}{\dot{V}_{ref}}\frac{\omega}{\omega_{ref}}\right)^2\right] \tag{5.12}$$

The power consumption is then calculated by making use of the efficiency:

$$\dot{W} = \frac{\dot{V}\Delta P}{\eta} \tag{5.13}$$

The older versions of the pump characteristics of the pump, T MAG-M2, are used to validate the model of Van Putten and Colonna. The older version of the pump characteristic includes the performance of the pumps at four different rotational speeds. The pump characteristic at 2900 rpm is used to calculate the pump characteristics at 1450, 1750 and 3500 rpm. Figure 5.5 shows the older pump characteristics provided by the manufacturer and the model predictions. The head pump characteristics are accurately predicted for 1450 and 3500 rpm. The model predicts a slightly lower head for 1750 rpm, but it is unlikely that another model performs better for every rotational speed. The efficiency prediction for a rotational speed of 1750 rpm has also the largest deviation. Because the pump characteristic is provided by the manufacturer in a graph, extracting the data points from the graph, will result in small deviations from the actual data. The predicted efficiency is used to calculate the power consumption of the pumps. Subsequently, the power consumption of the pumps is accurately predicted with the calculated efficiency.
The model of Van Putten and Colonna will be used to calculate the pump characteristics at different rotational speeds with the recent data of the pump manufacturer at 2900 rpm. The recent pump characteristics of the manufacturer and the predicted pump characteristics can be found in appendix B.

5.3. Slurry generator

The TBAB aqueous solution is super-cooled in the plate heat exchanger to generate TBAB hydrate crystals. The slurry generator is a plate heat exchanger produced by Alfa-Laval of the type AC-70X-30M. The properties of this plate heat exchanger are summarized in table 5.3. The hydraulic diameter provided by the manufacturer in table 5.3 is only valid when no crystal layer is present on the surface of the plates. When a crystal layer is formed at the surface of the plate heat exchanger, the hydraulic diameter is expressed by equation 5.14.

Table 5.3: Dimensions and properties of the AC-70X-30M plate heat exchanger.

Property	Value	Unit	Symbol
Height	0.526	m	H
Width	0.112	m	–
Plate length	0.466	m	L_{pl}
Plate width	0.100	m	–
Plate thickness	0.3	mm	δ_{pl}
Number of active plates	30	-	N_{pl}
Average distance between plates	2.0	mm	b
Hydraulic diameter	3.3	mm	d_h
Port diameter	18.0	mm	d_{pt}
Heat transfer area	1.71	m²	A
Surface enhancement factor	1.22	-	Φ

$$d_h = \frac{2(b - 2\delta_c)}{\Phi} \tag{5.14}$$

The total heat transfer surface is calculated according to the surface enhancement factor, the plate geometry and the number of active plates in equation 5.15.

$$A = \Phi L_p l W_p l N_p l \tag{5.15}$$

The pressure drop and heat transfer correlations of the TBAB slurry are already discussed in chapter 4. Because of the crystallization process in the generator, there are additional correlations required to describe this process.

Hydrate growth model

Since the temperature of the surface of the plates in the generator is lower than the temperature of the TBAB solution, the crystals are expected to form firstly on the surface of the plates of the generator. As mentioned before, when the thickness of the crystal layer increases, the flow passage area of the solution to flow though decreases. Due to conservation of mass, the velocity of the solution also increases. When the friction force between the crystal layer and the solution becomes large enough, the crystals detach from the heat transfer surface into the slurry. At this moment, the rate at which crystals are formed at the heat transfer surface is assumed to be equal to the rate at which the crystals are transported from the crystal layer to the slurry. The crystal layer thickness stays equal at this point.

The crystal growth mechanism is described by a modified model of Pronk [69] which is developed by Zak [98] and improved by Pronk [68] and Zhou [104]. The crystal production rate can be described with equation 5.16. The driving force of the crystal growth in this equation is the concentration difference between the solution and the saturation condition of the solution.

$$\dot{m}_{c,prod} = k \rho_c A (w_{sat} - w_{int}) \tag{5.16}$$

The mass transfer coefficient, k, can be derived from the following equation:

$$k = \frac{Sh\ D}{d_{h,c}} \tag{5.17}$$

The mass transfer coefficient can be calculated when the Sherwood number is known. The Sherwood number is a ratio of the convective mass transfer rate and the diffusion rate. The characteristic length in the Sherwood number is in this case defined as the crystal layer thickness.

$$Sh = \frac{k}{D/\delta_c} \tag{5.18}$$

The Sherwood number is expressed as a function of Schmidt number and the Reynolds number. The analogy with heat transfer is made in equation 5.19. This correlation for viscous flows in plate heat exchangers is developed by Warnakulasuriya and Worek [92] and has been used in previous studies.

$$Sh = 0.2875 Re^{0.78} Sc^{1/3} \tag{5.19}$$

In this equation the Schmidt number is defined as the ratio of viscous diffusion rate and molecular diffusion rate:

$$Sc = \frac{\mu}{\rho D} \tag{5.20}$$

The Sherwood number can also be expressed by making an analogy with fouling in plate heat exchangers. Li et al. [46] validated a relation for plate heat exchangers based on the three region model of Von-Karman.

$$Sh = (f/2)ScRe + (f/2)^{0.5} \times (5(Sc-1) + 5ln((5Sc+1)/6)) \tag{5.21}$$

Equation 5.19 is used to calculate the Sherwood number since this correlation includes the effect of the high viscosity of the slurry and the equation is similar to the experimentally validated equation by Gudjonsdottir [28].
The equations mentioned before are applied to the model by making use of a control volume method. The temperature difference of the volume element and the equilibrium temperature will be the driving force of the crystallization process. The crystal volume fraction increases as a function of the rate at which the crystals are produced:

$$\phi_c^{i=1} = \phi_c^i + \frac{\dot{m}_{c,prod}}{\rho_c \dot{V}} \tag{5.22}$$

By making use of an energy balance, the enthalpy of the next volume element can be calculated with the enthalpy of the previous cell and the heat transfer into the volume element.

$$h^{i+1} = h^i + \frac{\dot{Q}}{\dot{m}_{sl}} \tag{5.23}$$

Then, the solid mass fraction of TBAB and the temperature of the slurry in a volume element are a function of the enthalpy and the crystal volume fraction of that particular element.

$$w_{TBAB}^{i+1} = f(h^{i+1}, \phi_c^{i+1}) \tag{5.24}$$

$$T^{i+1} = f(h^{i+1}, \phi_c^{i+1}) \tag{5.25}$$

Hydrate layer thickness

The model to estimate the steady state hydrate production rate is developed by Zak [98]. In the model of Zak, it is assumed that the energy loss due to friction is equal to the hydrate layer removal work. When the hydrate production rate reaches a steady state, the crystal layer thickness will also be constant. In reality, not all the energy loss due to the friction is due to the crystal layer removal work. The energy loss due to friction can be divided into three main categories:

- The friction of the fluid to the crystal layer at surface of the plate heat exchanger.
- The friction of the fluid to the bare surface of the plate heat exchanger. These are the regions at the plates where no crystal layer is present.
- Viscous dissipation of the fluid.

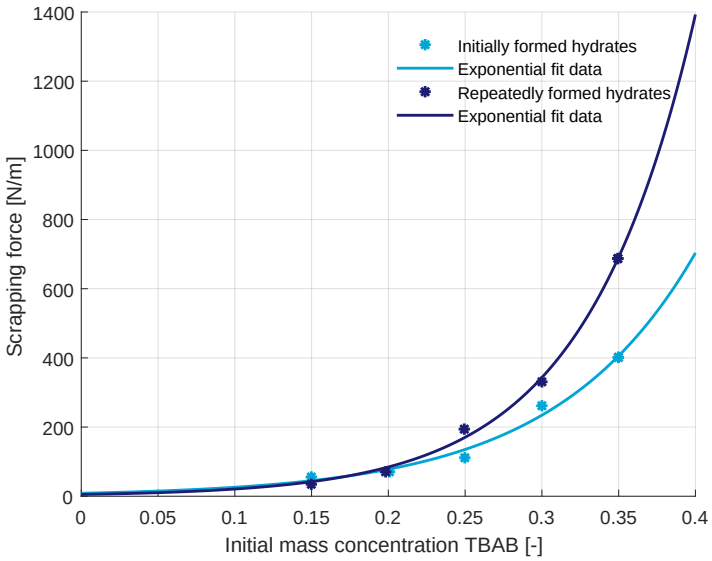

Figure 5.6: Measurements and exponential fit of the scrapping force needed to remove the initially and repeatedly formed TBAB hydrates from a brass surface [14].

The removal rate of the crystal layer is similar to removal rate of a fouling layer, since both removal rates are related to the friction at the walls of a plate heat exchanger. Arsenyeva et al. [5, 6] modelled and described the formation of a fouling layer in a plate heat exchanger. The factor ψ describes the part of the friction losses which attribute to the friction at the wall. The factor ψ depends on the Reynolds number, chevron angle and operant, a. The factor ψ can be found by a correlation proposed by Kapustenko et al. [37]:

$$\psi = \left(\frac{Re}{a}\right)^{-0.15sin(\beta)} \quad for\ Re > a \tag{5.26}$$

$$\psi = 1 \quad for\ Re \leq a \tag{5.27}$$

In these equations the operand, a, is equal to:

$$a = 380/tan(\beta)^{1.75} \tag{5.28}$$

For the characteristic flow velocities in the pilot plant, as mentioned in section 4.1, the factor ψ is equal to 1 for every accessible corrugation angle. A factor ψ of 1 implicates that the energy loss of the flow is equal to the friction losses with the surface. The crystal layer removal forces can now be predicted with equation 5.29.

$$\dot{V}\Delta P = \dot{W}_{rem} \tag{5.29}$$

Daitoku and Utaka [13–15] studied the adhesion and detachment characteristics of TBAB hydrate crystals on a heat transfer surface. They also measured the scrapping force which is needed to remove the crystals from the heat transfer surface. The structure of the initially formed crystals is different from the structure of the crystals which are formed after the first crystals are removed. They also found that the initial mass concentration of TBAB in the aqueous solution has a very large influence on the required removal force. This finding is also supported by Matsumoto et al. [56]. The scrapping force required to remove the initially formed crystals was found to be lower than the scrapping force needed to remove the crystals which are formed after the removal of the initially formed crystals. This effect is visible in figure 5.6.

Daitoku and Utaka also found that the scrapping force was dependent on the crystal layer thickness. Although this effect is present, it will be neglected in the current model since the effect of the initial mass concentration of TBAB has a much larger influence on the required scrapping force. Also, the limited hydraulic diameter of the plate heat exchanger limits the maximum crystal layer thickness which reduces the influence

of this effect. The required scrapping force is also measured for a PTFE heat transfer surface. The effect of the crystal layer thickness on the required scrapping force was not noticeable for the PTFE surface [15]. The PTFE surface is also smoother and the contact angle of the crystal layer with the surface is larger compared to the brass surface. Because of these factors, the scrapping force needed to remove the crystals, was also smaller for a PTFE surface. Because of this, the measurements of the scrapping force of the brass surface are expected to be more representative for the actual stainless steel plate heat exchanger. The exponential fit of the measurements in figure 5.6 resulted in the following correlations:

$$\text{Initially formed crystals: } F_{scrap} = 8.67e^{11.0 w_{0,TBAB}} \tag{5.30}$$

$$\text{Repeatedly formed crystals: } F_{scrap} = 5.14e^{14.0 w_{0,TBAB}} \tag{5.31}$$

The removal work is determined by making use of the removal force. It is assumed that the crystal layer thickness is equal to the average crystal length. Therefore, the average time it takes to remove a crystal from the crystal layer surface can be calculated by making use of the crystal growth rate in equation 5.32.

$$t_{rem} = \frac{\delta_c}{\dot{m}_{c,prod}/(\rho_c A)} \tag{5.32}$$

The removal work is then calculated as a function of the scrapping force and the crystal removal time.

$$\dot{W}_{rem} = \frac{F_{scrap} A}{t_{rem}} \tag{5.33}$$

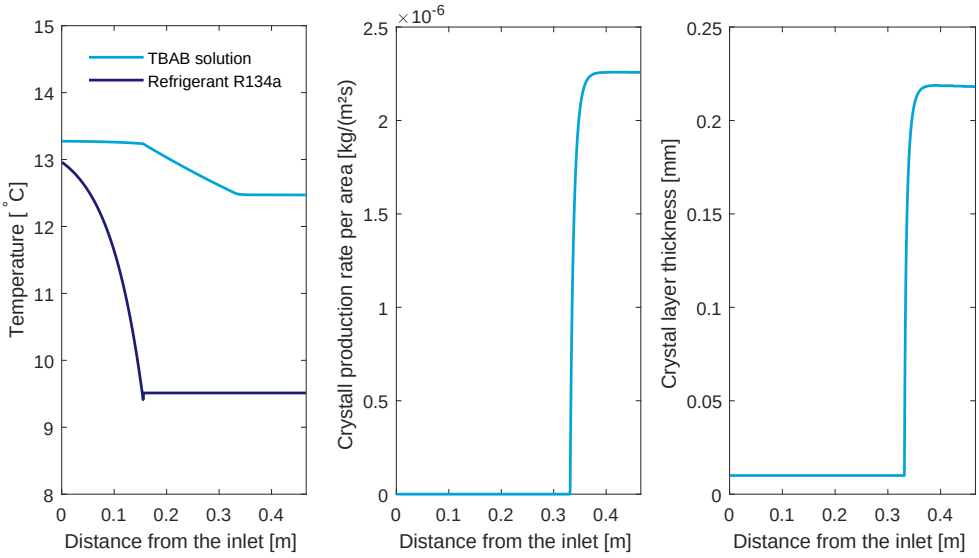

Figure 5.7: Simulation result of the generator with a mass flow rate of 0.69 kg/s.

Complete hydrate generation model

The model of the generator simulates the behaviour of both the refrigerant side as well as the TBAB slurry side of the plate heat exchanger. The generator is divided into control volumes in which properties such as the temperature, crystal layer thickness and crystal production rate are calculated. Figure 5.7 shows the result of a simulation of the generator model. The figure 5.7 shows the following results:

- The crystals start to appear when the solution temperature is cooled to the equilibrium temperature.
- In the superheating region of the refrigerant, the heat fluxes are lower. This results in a slower temperature drop of the TBAB solution or in a slower crystal production rate if the temperature of the TBAB solution is low enough.

- There is an equilibrium between the crystal production rate and the crystal removal rate. Because of this equilibrium, the crystal layer thickness will be constant.

- There is a discontinuity visible in the refrigerant temperature profile around a distance from the inlet of 0.1 m. This discontinuity is present because the temperature of the refrigerant in the super heating zone is calculated with the pressure in the corresponding cell while the temperature in the evaporation zone is based on the inlet pressure.

5.4. Compressor

The condenser unit which is used in the pilot plant is a Bitzer LH44E/2FES-3Y. This condenser unit contains a compressor of the type 2FES-3Y-40S. The properties of the compressor are summarized in table 5.4.

Table 5.4: Dimensions and properties of the 2FES-3Y-40S compressor

Property	Value	Unit	Symbol
Bore	25	mm	B
Stroke	25	mm	l
Number of cylinders	2	-	N_{cyl}

The volumetric and isentropic efficiency of the compressor describe the power consumption of the compressor. These two parameters are both a function of the pressure ratio and the inlet temperature. The manufacturer of the compressor provides a model which gives the volumetric and isentropic efficiency for a given pressure ratio [10]. The data of the model of Bitzer is analysed according to the method of Shi [73].

The data of the model of Bitzer is used to fit a function for the volumetric and isentropic efficiency. Figure 5.8 shows the data points and the fitted function for the volumetric and isentropic efficiencies. Because the inlet conditions remain partially constant during normal operation of the compressor, this influence on the volumetric and isentropic efficiency is neglected. Only the pressure ratio will change, since the pressure ratio depends on the ambient temperature which will change during operation. The isentropic and volumetric efficiency of the compressor are calculated with equation 5.35 and equation 5.35 respectively.

$$\eta_{vol} = -1.198 P_{rat}^{0.1292} + 2.241 \tag{5.34}$$

$$\eta_{is} = 0.6374 e^{-0.004916 P_{rat}} - 0.8995 e^{-1.14 P_{rat}} \tag{5.35}$$

The pressure ratio, the rotational speed and the volumetric efficiency of the compressor determine the volumetric flow rate:

$$\dot{V} = \eta_{vol} \left(N_{cyl} \pi \frac{B^2}{4} l \omega \right) \tag{5.36}$$

The isentropic efficiency is used to calculate the enthalpy at the outlet of the compressor:

$$h_{out} = \frac{h_{out,is} - h_{in}}{\eta_{is}} + h_{in} \tag{5.37}$$

Finally, the electric power consumption can be calculated from the mechanical efficiency of the compressor:

$$\dot{W}_{elec} = \frac{\dot{m}_r (h_{out} - h_{in})}{\eta_{mech}} \tag{5.38}$$

The mechanical efficiency of the compressor, η_{mech}, is assumed to be 0.9670 based on the data provided by the manufacturer. The mechanical efficiency is also assumed to be constant, since the pressure ratio has a very small influence on the mechanical efficiency.

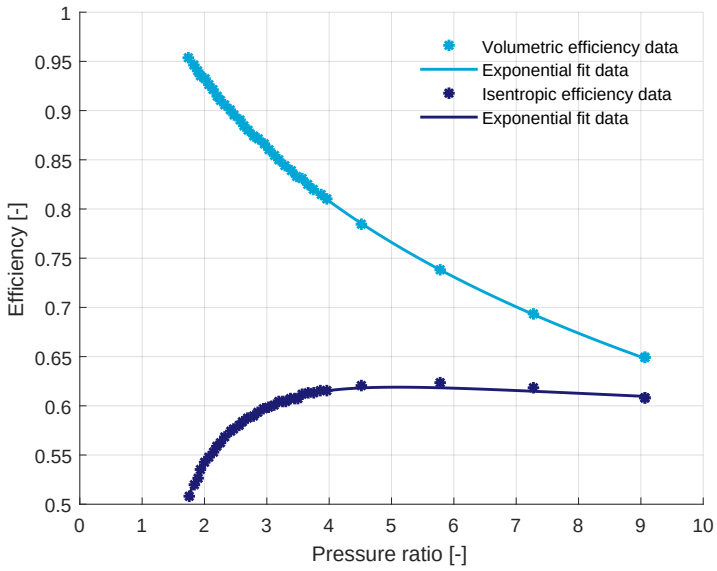

Figure 5.8: Volumetric and isentropic efficiency data points and fitted fuctions for different pressure ratios from the model of Bitzer [10].

5.5. Condenser

The compressor of the pilot plant is a part of the condenser unit as mentioned in section 5.4. The performance of the condenser unit has influence on the energetic performance of the whole system. Bitzer also provides data for the condenser unit in their reference model [11]. The properties of the condenser unit are summarized in table 5.5.

Table 5.5: Properties of the 2FES-3Y-40S condenser unit.

Property	Value	Unit	Symbol
Fan power consumption	155	W	$\dot{P}_{fan}$
Air flow rate	2000	m³/h	$\dot{V}$

Since the dimensions of the equipment are not specified by the manufacturer, it is not possible to make a theoretical model of the heat transfer equipment. The overall heat transfer coefficient of the condenser is determined with the thermal properties included in the model provided by Bitzer. Pronk [68] used the reference model to find the overall heat transfer coefficient for varying operation conditions. Based on the data of the overall heat transfer coefficient for multiple operation conditions, a correlation for the overall heat transfer coefficient is found:

$$UA = -13.14P_{rat} + 146.5P_{rat} + 324.8 \tag{5.39}$$

The correlation of the overall heat transfer coefficient is constructed by relating the capacity of the condenser unit with the logarithmic mean temperature difference, LMTD. The temperature at the inlet and the outlet of the condenser unit and the condensation temperature are used to calculate the LMTD. The correlation is constructed and thus valid for the whole mass flow range encountered in the condenser unit. Also, the pressure ratio is used in the correlation to take the higher super heating conditions into account for high pressure ratios. The power consumption of the fan of the condenser is related to the power consumption of the generator and the compressor. Only the required condensation temperature is still unknown. The desired condensation temperature can be determined with the number of transfer units since the overall heat transfer coefficient is known.

5.6. Storage vessel

The storage vessel of the pilot plant has a capacity of 300 litre. The storage tank is used to store the TBAB hydrate crystals which are produced over night until there is a cooling demand during the day. Properties of

the storage vessel are summarized in table 5.6. Since the TBAB hydrates have a higher density compared to the solution, the crystals will settle over time at the bottom of the tank. To model the settling of the crystals in storage vessel, the models of Douzet et al. [20] and Flick et al. [24] are used as a basis. The model, developed by Pronk [68], neglects diffusion in the storage tank, since diffusion is a very slow process compared to the settling. Also, the possibility of a superheated solution is present in the model. The model of storage vessel gives insight in the settling process inside the storage vessel. Based on the simulations of the storage vessel, the following observations can be made:

- Only when the system is not producing crystals and is not delivering crystals to the application side, the crystals will settle in the storage vessel. With the typical mass flow rate of the system, it takes between 4 and 7 minutes to circulate the whole content of the storage vessel. So, it is expected that there will be a homogeneous slurry after a short time instance when the pumps are operating. Thus, the time step of the model should be very small to capture the settling and mixing behaviour of the slurry. This makes the model slower.
- The typical mass flow of slurry when crystals are produced is 0.70 kg/s. This mass flow limits the time step of the model to simulate the settling accurately. The mass flow of 0.7 kg/s reduces the time step somewhere between 1 and 10 seconds.
- To perform an accurate description of the settling of the crystals, the storage vessel should be divided into at least six volume elements.
- The settling behaviour of the crystals in the storage vessel depends on the crystal size. The size of the crystals is not known beforehand. The production of the crystals in the generator and attrition of the crystals by the pumps in the system will have an influence on the size of the crystals. The average size of the TBAB hydrates is described in earlier research [47, 100, 101], but these crystals are formed in controlled circumstances.

Table 5.6: Dimensions and properties of the storage vessel.

Property	Value	Unit	Symbol
Vessel diameter	0.9	m	d
Vessel height	0.7	m	H
Insulation thickness	13	mm	δ
Thermal conductivity insulation	0.033	W/(m K)	λ

The higher accuracy of an extended model of the crystal settling in the storage vessel does not outweigh the disadvantages. The extended model of the storage vessel will slow down the calculations. Also, the better insight in the behaviour of the storage vessel is not necessary in the model. Therefore, the storage vessel will be modelled as a lumped element.

5.7. Reference building

The slurry in the pilot plant is produced to cool down the room temperature of a space of around 144 m². The cooling load of this space is unknown and is not measured. To simulate the cooling load of the pilot system, a simple model of a reference building is made. This model should find a reasonable estimation of the cooling and heating load during a year. The actual building in Twello is not described by the model since too many variables such as building material, dimensions and occupancy of the room during a year are unknown. The reference building is a fictional building of 144 m² somewhere in the Netherlands. The fictional building has a glass façade and two external walls. The reference building is divided into seven volume elements, each with their own thermal mass, temperature and solar gains. The volume elements represent the walls, the glass façade, the roof and the floor. The energy balance for each volume element is calculated with equation 5.40.

$$\Sigma \dot{Q} = \dot{m} c_p \frac{dT}{dt} \tag{5.40}$$

Each energy balance contains the heat flow due to convection, conduction and mass transfer. The temperature of each volume element is determined each time interval by solving the energy balance. The reference

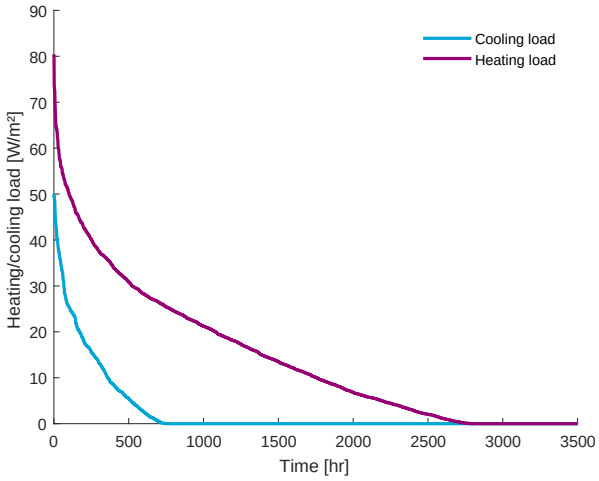

Figure 5.9: Cooling- and heating load of the reference building for a year. The cooling- and heating load is displayed per unit of area at the vertical axis while the duration of the cooling- and heating load is displayed at the horizontal axis.

building is used to simulate the cooling load of one year. The climate data necessary to determine the cooling load is described in the NEN 5060 [61]. The NEN 5060 contains a reference climate year for the Dutch climate. The air change rate per hour, ACH, is assumed to be 36 m³ per hour per person. Also, the infiltration rate is assumed to be 0.5 ACH. The simulation of the reference building results in a total cooling load of 34.40 MJ/m² for 746 hours of cooling demand. ECN reports a cooling energy need between 31.0 MJ/m² and 59.0 MJ/m² for similar building types while the hours with a cooling demand lie between 548 and 778 per year [70]. The report of ECN contains the cooling and heating load for multiple utility buildings. They also investigated how the cooling load is affected by a change in the insulation, internal heating load, thermal mass and sun blinds. The cooling load and hours of cooling demand from the ECN report are in agreement with the model of the reference building. Figure 5.9 shows the cooling and heating demand per square meter.

5.8. Conclusion

The equations and correlations which are used to model the pilot plant are reviewed in this chapter. Each component of the pilot plant is modelled in Matlab as a function. Also, the properties, heat and pressure drop correlations of the fluid from chapters 3 and 4 are implemented in the model. The model is solved iteratively for each time step to simulate the behaviour of the pilot plant.

6

Model validation

The model of the TBAB air conditioning system, as discussed in chapter 5, is validated with measurements from the pilot system in Twello. The sensors that are used to conduct the measurements and the accuracy of the sensors can be found in appendix C. The model is validated by comparing the measurements of the pilot plant to the output of the model for each component by making use of different correlations. In this manner, the most suitable correlations can be selected. Also, the strengths and the weaknesses of the model will be determined and discussed.

6.1. Air cooler

During the cooling operation, the temperature of the TBAB slurry or solution and the air are measured every 10 seconds at the inlet and outlet of the air cooler. The temperature measurements of the air cooler are shown in figure 6.1. The capacity of the air cooler is calculated from the temperatures and the mass flow rates of TBAB flowing through the air cooler. The capacity of the air cooler based on the measurements is used to select the most suitable correlation for the air side heat transfer coefficient. However, the experimental data is partially incomplete:

- The air mass flow rate has been determined by measuring the flow velocity in the air ducts. Since the fan is not speed controlled, a more constant air flow rate is expected.
- The temperature of the air entering the air cooler is measured by a recently placed temperature sensor. However, there is no data available with the new temperature sensor since the ambient temperature has been too low for the condenser to operate. Therefore, the temperature of the air entering the air cooler has been estimated. The air comes from a sports hall.
- The air mass flow rate should be calculated from an energy balance when the air temperatures at the inlet and outlet of the air cooler are known. However, such an energy balance does not include the condensation effect since the humidity of the air is unknown. Also since the amount of condensation depends on the surface temperature of the air cooler and the local air temperature, it is difficult to predict.

The mass flow rate of TBAB flowing through the air cooler is used to calculate the cooling capacity of the air cooler. The capacity of the air cooler is also determined with several different correlations for the convective heat transfer coefficient of air flowing through the air cooler. Figure 6.2 shows the results of these correlations and the capacity of the air cooler based on the measurements. The correlations are well able to predict the capacity of the air cooler. This is because the capacity of the air cooler is not limited by the heat transfer mechanisms but by the flow rates.
During operation of the air cooler, the flow rate of TBAB is constant for 30 minutes and thereafter the flow rate changes rapidly resulting in a lower capacity estimation by the correlations. During normal operation, for instance from 13:00 to 13:30, the correlations from the VDI heat atlas [89] and the course refrigeration technology and applications [33] predict the capacity the most accurately. The correlation of Briggs and Young

[12] underestimates the capacity of the air cooler. Based on figure 6.2 and results from a previous study [68] the correlation from the VDI heat atlas is selected to describe the air side heat transfer in the air cooler.

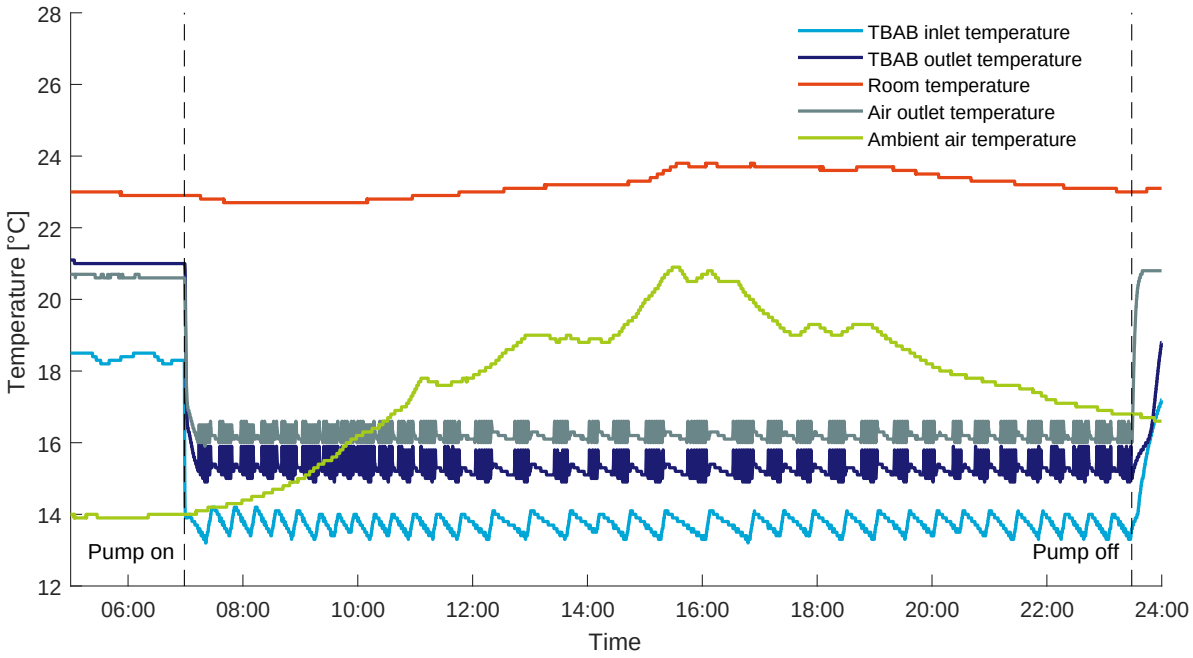

Figure 6.1: Temperature measurements while cooling the air in the air cooler with the TBAB solution.

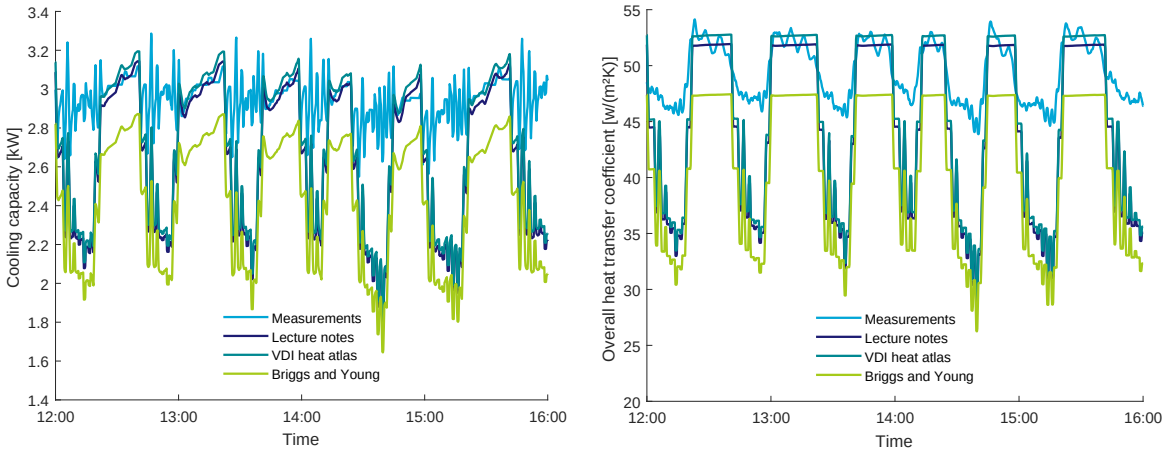

(a) Cooling capacity of air cooler during operation.

(b) Overall heat transfer coefficient of air cooler.

Figure 6.2: Cooling capacity and overall heat transfer coefficient of the air cooler. The measurements are compared with several correlations [12, 33, 89]. The overall heat transfer coefficient is based on the external heat transfer area of the finned tubes.

6.2. Generator

The generator is a plate heat exchanger in which the slurry or solution is cooled down while evaporating the primary refrigerant. The flow rate of the primary- and secondary loop refrigerant are measured. Also, the inlet and outlet temperatures of the TBAB flow are measured. The capacity of the generator can be calculated by an energy balance of both flow sides:

$$\dot{Q} = \dot{m}\Delta h \tag{6.1}$$

The energy balance is solved for both sides of the generator. Figure 6.3 shows the capacity of the generator

calculated from the energy balances of both sides. The capacity of the generator calculated from both sides is not exactly equal. This is probably caused by the following phenomena:

- Initially the temperature of the plate heat exchanger is higher compared to the refrigerant temperature. In the beginning a part of the energy transferred from the refrigerant is absorbed by the thermal mass of the plate heat exchanger. When the compressor is turned off, the same phenomenon will take place. This is not noticeable from figure 6.3 since the mass flow and thus the heat transfer rate from the energy balance becomes zero when the pump and the compressor are turned off.

- The enthalpy is based on measurements of sensors which are not placed directly at the inlet and outlet of the generator. Friction losses and heat transfer to the environment have influence on the calculated enthalpy at the inlet and outlet of the generator.

- The mass flow at the refrigerant side is influenced by the throttle valve. This gives the heat transfer rate from the energy balance of the primary refrigerant side an oscillating behaviour. The mass flow rate at the TBAB side of the generator is kept constant.

- The heat transfer rate at the TBAB side shows some 'jumps'. These are caused by the resolution of 0.1 K of the temperature sensors.

The temperatures at the inlet and outlet of the generator are also measured, see figure 6.4a. The TBAB flow cools down during operation while the refrigerant flow heats up. The valve controls the mass flow of the refrigerant in order to control the desired superheating degree of 2 K. Figure 6.4b shows the throttling of the valve and the superheating degree of the refrigerant. The valve shows an oscillating behaviour causing the superheating degree to move around the 2 K. The control of the valve should be adjusted to allow a more constant superheating degree. The valve is able to control the refrigerant flow in order to reach the desired superheating degree: the valve is not constantly 100% open.

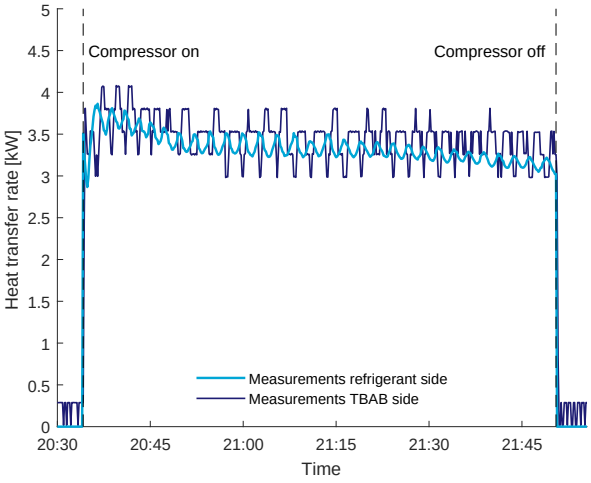

Figure 6.3: Heat transfer rate in the generator based on an energy balance and experimental data for the refrigerant side and TBAB side.

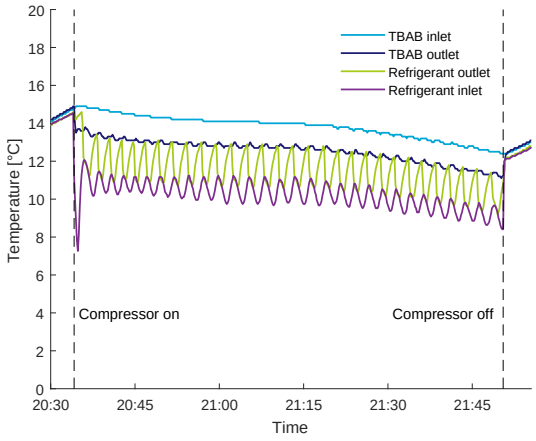

(a) Temperatures measurements at the inlet and the outlet of the generator.

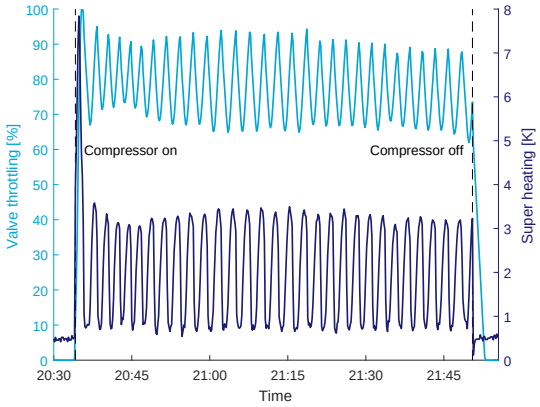

(b) Superheat measurements of refrigerant and valve throttling.

Figure 6.4: Temperature levels in the generator during operation and valve throttling behaviour.

Pressure drop correlations

The model also calculates the pressure drop across the generator for both the primary and secondary refrigerant side. The pressure drop correlation for the TBAB side, the secondary refrigerant, is already validated in section 4.5. The pressure drop correlation of TBAB slurry and solution flowing through a plate heat exchanger of Ma and Zhang is considered to be the most suitable correlation [49]. The pressure drop of the primary refrigerant side has been measured for different flow rates. Figure 6.5 shows a comparison between the pressure drop measurements and several pressure drop correlations. These pressure drop calculations neglect the pressure drop in the super heating zone. The properties which are used, are average values of the refrigerant flow in the generator. The total pressure drop of the refrigerant in the generator consists out of three parts: friction in the ports, friction between the plates and friction due to acceleration.

$$\Delta P = \Delta P_f + \Delta P_{pt} + \Delta P_a \tag{6.2}$$

The pressure drop due to acceleration is calculated with the following equation:

$$\Delta P_a = G^2 \Delta X (1/\rho_G - 1/\rho_L) \tag{6.3}$$

The pressure drop across the inlet and outlet ports of the generator is calculated with the correlation suggested by Shah and Focke [72]:

$$\Delta P_{pt} = 0.75 \left(\frac{G_{pt}^2}{2\rho_{liq}} + \frac{G_{pt}^2}{2\rho_m} \right) \tag{6.4}$$

Figure 6.5 shows a comparison of the pressure drop measurements and correlations of the refrigerant R134a flowing through the generator. From the figure it follows that the precision of pressure drop sensors is 1.0 kPa. The correlation of Yan and Lin [96] is based on data of R134a flowing through a plate heat exchanger at higher mass flow rates. The correlation of Han et al. [29] is based on the refrigerants R410a and R22 instead of R134a. The correlation of Amalfi et al. [4] matches the experimental data of R134a flowing through the generator the most accurately. Therefore, the correlation of Amalfi et al. will be selected to calculate the pressure drop in the model of the primary refrigerant in the generator.

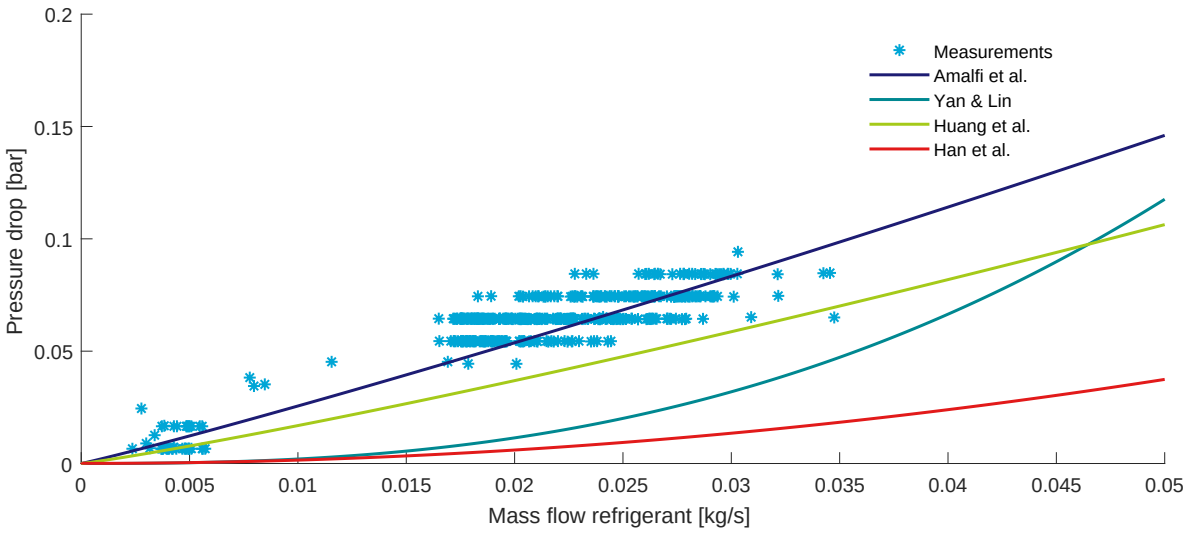

Figure 6.5: Comparison of the pressure drop measurements and correlations of the refrigerant flowing through the generator [3, 4, 29, 32, 96].

Heat transfer correlations

In the generator the TBAB solution or slurry is cooled down by evaporating the primary refrigerant R134a. Firstly, the primary refrigerant is evaporated in the generator and then superheated. During the evaporation of the refrigerant, a phase change is taking place. During the superheating of the refrigerant, there is no phase change. These phenomena divide the generator into two sections: the evaporating zone and the superheating zone. The heat transfer rate from equation 6.1 is used to calculate the overall heat transfer coefficient. The Nusselt number correlations of several studies, as mentioned in section 4.6, are used to calculate the convective heat transfer coefficient for the evaporation in the plate heat exchanger. In order to calculate the convective heat transfer coefficient of the refrigerant from the overall heat transfer coefficient, it is assumed the heat transfer of the refrigerant in the super heating zone is negligible compared to the heat transfer of the refrigerant in the evaporating zone. The convective heat transfer rate of the refrigerant follows from equation 6.5. Figure 6.6 shows the convective heat transfer coefficient of the refrigerant for varying mass flow rates of the refrigerant.

The correlation of Han et al. [29] overestimates the heat transfer coefficient. This correlation is based on measurements of the refrigerants R410A and R22 and is thus less suitable for the model. The correlations of Amalfi et al. [4] and Huang et al. [32] seem to provide the best result. The correlation of Amalfi et al. is selected for the current model because this correlation matches the experimental data the most accurately.

$$\frac{1}{U} = \frac{1}{\alpha_{r,evap}} + \frac{\delta_{pl}}{\lambda_{pl}} + \frac{1}{\alpha_{TBAB}} \tag{6.5}$$

The generator model uses the correlation of Thonon [84] for the refrigerant in the superheating zone, equation 6.6, and the correlation of Amalfi et al. [4] for the evaporation of the refrigerant. Table 6.1 shows the output of the model for a given mass flow rate of the primary- and secondary refrigerant. The model slightly underestimates the heat transfer rate, but the error seems to be around 5% for these operating conditions.

$$Nu = 0.2267 Re^{0.687} Pr^{1/3} \tag{6.6}$$

Table 6.1: Output of the generator model for varying mass flow rates.

Time stamp	Refrigerant	$\dot{m}$[kg/s]	T_{in} [°C]	T_{out} [°C]	$\dot{Q}_{data}$ [kW]	$\dot{Q}_{model}$ [kW]
21:45:00	TBAB	0.695	12.8	11.5	3.10	3.04
	R134a	0.016	8.9	10.9		
20:45:10	TBAB	0.70	14.8	13.3	3.25	3.10
	R134a	0.019	10.5	11.8		
21:17:50	TBAB	0.69	13.9	12.6	3.22	3.05
	R134a	0.017	9.7	12.1		

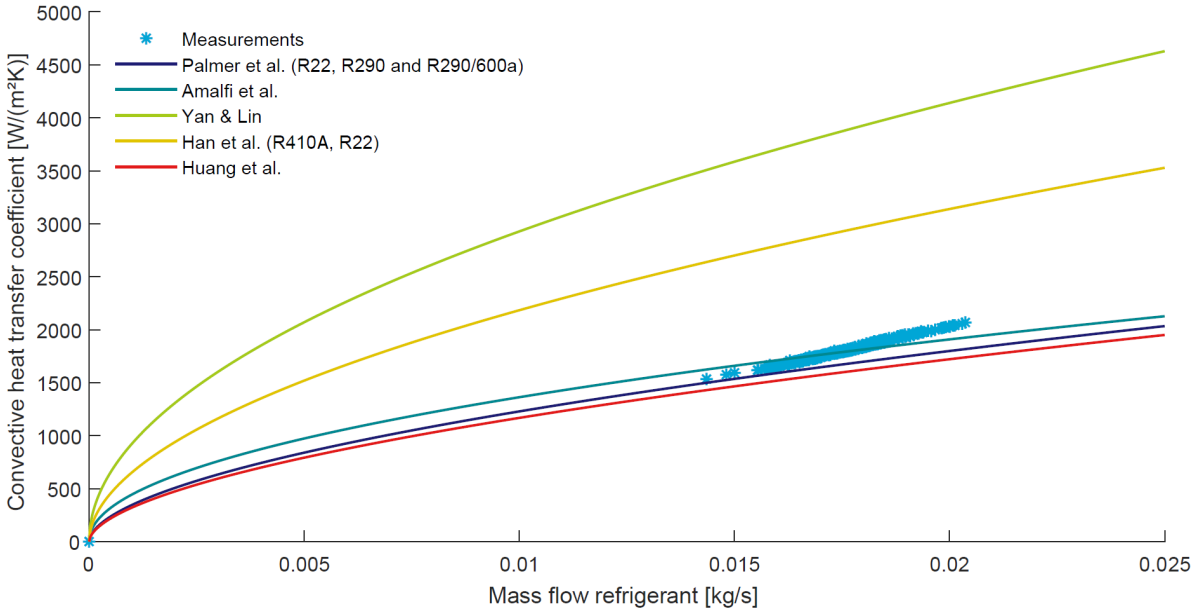

Figure 6.6: Convective heat transfer coefficient of R134a in the generator for varying mass flow rates compared with several Nusselt number correlations for the evaporation primary refrigerant [4, 29, 32, 66, 96].

Hydrate crystal production

During the experiments hydrates crystals were produced. The solid mass fraction of the slurry can be determined from the slurry temperature and density. However experimental data of continuous hydrate crystal production for a longer period is not yet available. Figure 6.7 shows the pressure drop measurements over the generator during the crystal production process. During this process the TBAB solution was cooled down to 9 °C. A smaller supercooling degree is preferable. The large supercooling degree results in a rapid uncontrolled crystal layer growth process. The pressure drop rises to 4 bar at 8:22 while the density rises. At 8:22 the compressor is turned off. From 8:30 to 8:35 the pressure drop and flow rate in the generator stay almost constant and a more steady state hydrate crystal production process is expected. Table 6.2 shows the predicted pressure drop during the generation process. A lower pressure drop is expected. Although the higher pressure drop might be assigned to the too rapid crystal layer growth due to the too high supercooling degree. When the crystal layer growth is limited by a lower supercooling degree, the experimental results may vary.

The model predicts a crystal layer thickness of 0.26 mm for steady state crystal production. A crystal layer thickness of 0.32 mm results in a pressure drop prediction by the model of 115 kPa. However more measurements of the crystal production process under desirable operating conditions should validate the crystal production model.

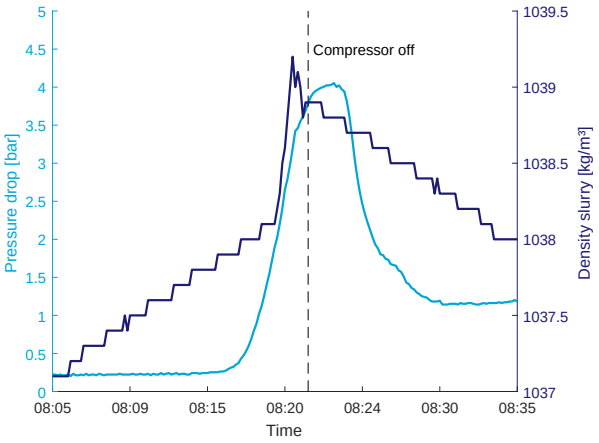

Figure 6.7: Pressure drop measurements of the generator during hydrate production. The generator pump is turned off at 32:55.

Table 6.2: Pressure drop measurement and model prediction during hydrate generation process.

Time stamp	Density [kg/m³]	ω_c [-]	ΔP data [kPa]	ΔP model [kPa]
8:18	1038	$\pm$ 0.05	115	85

6.3. Compressor

During the experiments, the power consumption of the compressor is measured. The model, as mentioned in section 5.4, calculates the power consumption of the compressor by taking the volumetric- and isentropic efficiencies into account. The power consumption of the compressor can also be calculated from an energy balance:

$$\dot{W} = \frac{\dot{m}\Delta h}{\eta_{mech}} \tag{6.7}$$

The model is compared with the power consumption measurements and the energy balance of equation 6.7.

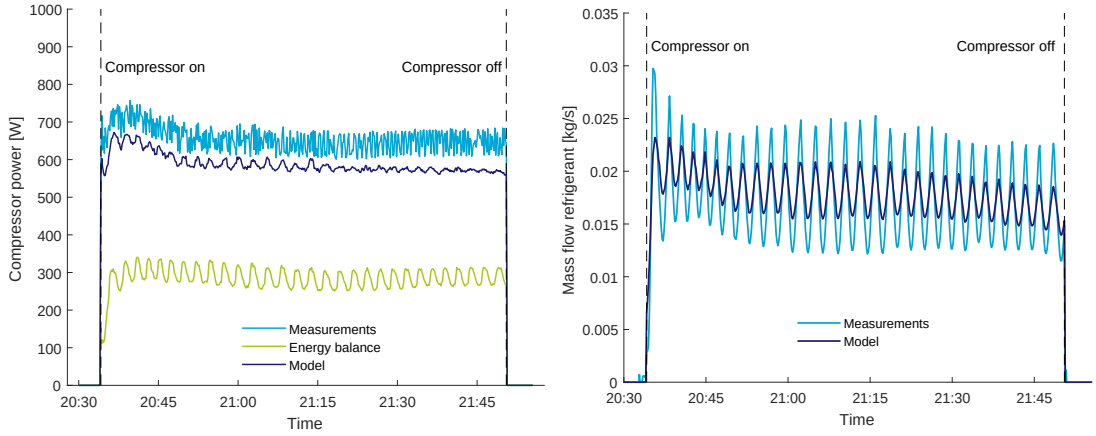

(a) Power consumption comparison of the compressor. (b) Mass flow comparison of the primary refrigerant.

Figure 6.8: Performance comparison of the compressor during operation.

The mechanical efficiency in the model in equation 6.7 is estimated to be $\eta_{mech} = 0.9670$ based on the data obtained from the model of manufacturer [10]. Figure 6.8a shows the power consumption measurements, the power consumption of the model and the power consumption based on the energy balance. The model is able to predict the power consumption of the compressor with an error of approximately 5-10%. The energy balance is not able to accurately predict the power consumption of the compressor. The pressures and temperatures are not directly measured at the inlet and the outlet of the compressor. This allows energy to be transferred to the environment. Also, the pressure losses due to transportation of the refrigerant effect the pressure measurements. Based on the experimental data, the model provides a reasonable accurate result for the power consumption of the compressor. The model of Bitzer [10] for the isentropic efficiency is in good agreement with the experimental data.
The modelled and measured flow rate of the primary refrigerant are shown in figure 6.8b. The measurements of the refrigerant flow rate show an oscillating behaviour caused by throttling of the expansion valve. The model is able to predict the average mass flow of the refrigerant. The amplitude of the mass flow rate of the model does not match the measurements. Since the valve throttling shows this oscillating behaviour, it is expected that the mean value of this curve is the desired mass flow rate of the refrigerant. Also, since the time step of the model will be larger than the 10 second time interval of the measurements, the correct average value of the mass flow is sufficient for the model. Therefore, the volumetric efficiency is considered to be well predicted by the model under these operating conditions.

6.4. Condenser

The superheated primary refrigerant is condensed in the condenser. In order to facilitate the desired heat transfer, the difference between the ambient air temperature and the condensation temperature must be sufficient. Therefore the operating pressure in the condenser should ideally be controlled based on the ambient air temperature and the capacity. Figure 6.9 shows a comparison of the measured and modelled condensation pressure. The condensation pressure is accurately predicted by the model until 21:15. Then the model underestimates the condensation pressure with an error of approximately 5% while the ambient temperature lowers gradually during the experiment from 12.8 to 11.8 °C. The actual system seems to react slower to changes in the ambient temperature. This is probably due to the control parameters of the system.
Figure 6.10 shows the measured pressure at the inlet and the outlet of the condenser. Since there is too little data available of the condenser to make an accurate estimation of the pressure drop, the pressure drop in the condenser in the model is neglected. However, the measurements show a relative constant pressure drop of approximately 0.33 bar. It is not certain whether the pressure drop in the condenser is the same for different operation conditions. Measurements at different mass flow rates show a pressure drop of 0.7 bar at 0.0361 kg/s. The pressure at the inlet of the condenser can be calculated by using the following correlation for the pressure drop obtained from the measurements:

$$\Delta P = 3.276 \times 10^4 \left(\frac{\dot{m}_r}{0.0175} \right) \tag{6.8}$$

The pressure at the inlet of the condenser follows from the condensation pressure of the refrigerant and the pressure drop in the condenser.

$$P_{in} = \Delta P + P_{cond} \tag{6.9}$$

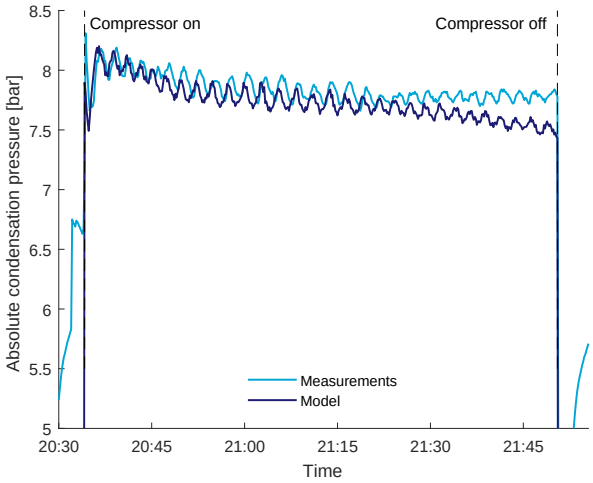

Figure 6.9: Condensation pressure of the refrigerant from measurements and model. The condensation pressure is the pressure at the outlet of the condenser. The ambient temperature lowers during the experiment from 12.8-11.8 °C.

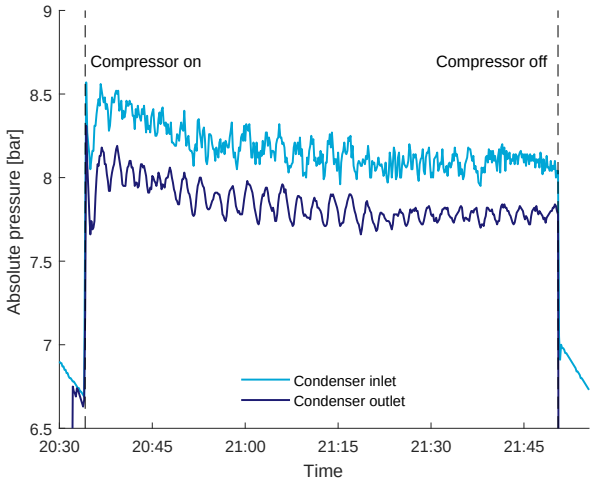

Figure 6.10: Pressure measurements at the inlet and outlet of the condenser.

6.5. Pumps

The pump characteristics are used to model the pumps in the pilot system. As mentioned before in section 5.2, the model of Van Putten and Colonna [88] is used to calculate the pump characteristics at different rotational velocities. The pressure data acquisition of the pilot system measures the pressure levels with a precision of 1.0 kPa. The larger pump, T MAG-M4, pumps the slurry through the generator. The smaller pump, T MAG-M2, pumps the slurry through the air cooler.
Table 6.3 shows the measurements and model results of the air cooler pump. The model is able to accurately predict the mass flow rate. The pressure measurements are probably incorrect, since only a pressure is measured for a pump frequency of 60%.

Table 6.3: Comparison of measurements and model of the air cooler pump, T MAG-M2

Time stamp	Frequency [%]	ΔP data [kPa]	ΔP model [kPa]	$\dot{m}$ data [kg/s]	$\dot{m}$ model [kg/s]
08:20:00	20	0.00	0.06	0.16	0.18
07:32:00	32	0.00	0.15	0.28	0.29
20:33:00	60	0.08	0.4	0.58	0.59

Table 6.4 shows the measurements and model results of the generator pump. The pressure drop in the generator is calculated with the correlation of Ma and Zhang [49] as mentioned in section 4.5. This correlation is based on TBAB flowing through a plate heat exchanger. The model overestimates the mass flow. This is probably due to the underestimation of the total pressure drop in the circuit of the generator or a slight deviation of the modelled pump characteristic. Therefore, the performance of the sensors should be assessed in order to determine the source of these deviations.

Table 6.4: Comparison of measurements and model of the generator pump, T MAG-M4

Time stamp	Frequency [%]	ΔP data [kPa]	ΔP model [kPa]	$\dot{m}$ data [kg/s]	$\dot{m}$ model [kg/s]
13:53:00	60	0.20	0.21	0.69	0.83
13:53:00	62	0.21	0.20	0.7	0.79

6.6. Conclusion

The model of each component of the pilot system in Twello has been validated with experimental data of the pilot system:

- The current experimental data of the air cooler is insufficient to make an accurate validation of all the correlations. Measurements with the added temperature sensor allow for a more accurate validation.

However, the model is able to describe the capacity of the air cooler with the correlation of the VDI heat atlas [89].

- The heat transfer and pressure drop measurements of the primary refrigerant in the generator have been compared with several correlations. The correlation of Amalfi et al. describes the heat transfer and pressure drop of the refrigerant during evaporation the most accurately [4]. The correlation of Thonon is selected to describe the heat transfer of the refrigerant in the superheating zone. The model underestimates the pressure drop and thus the crystal layer thickness during the crystal generation process. However, the experimental data is very limited and more experimental data during continuous crystal production is desired to validate the crystal generation model.
- The model is able to predict the power consumption of the compressor with an error of 5-10%. The mass flow of the primary refrigerant flowing through the compressor is also accurately predicted by the model. The model of the isentropic and volumetric efficiency based on the data of Bitzer [10] is in agreement with the measurements.
- The modelled condensation pressure adapts better to ambient temperature changes compared to the measured condensation pressure. This can be an indication that the system can be further optimized. Overall the modelled condensation pressure matches the measurements quite accurately. The measurements of the pressure drop over the condenser provide data for a pressure drop correlation which is implemented in the current model.
- The frequency of the pumps has been used as input for the model to determine the flow rate and the pressure drop. The pressure drop measurements on the air cooler side of the circuit show unrealistic values. However, the model describes the mass flow rates in the air cooler quite accurately. At the generator side the pressure drop over the generator is accurately predicted. The model predicts a higher mass flow rate. This can be caused by an underestimation of the pressure drop of the whole generator circuit or deviations in the modelled pump characteristics.

7

Optimization of the model parameters

The model of the pilot system will be used to determine the performance of the TBAB secondary loop air-conditioning system. Since the overall performance of the system heavily depends on the control parameters of the system components, it is necessary to select the right parameters to obtain the best overall system efficiency. This chapter considers the most optimal control parameters for each component in respect to the overall performance of the system.

7.1. Optimal generator mass flow rate

During the cooling operation of the secondary refrigerant, the mass flow rate of the secondary refrigerant can be varied. A higher mass flow rate generally results in a higher cooling capacity of the generator but also in a higher power consumption of both the condensing unit and secondary refrigerant pump. The power consumption of the compressor depends on the mass flow rate of the primary refrigerant. The power consumption of the fan of the condensing unit is constant, since the fan is not speed controlled.
In order to determine the optimal mass flow rate of the slurry in the generator, the slurry mass flow is varied while the super heating degree of the primary refrigerant is kept constant at 3 K. To determine the influence of the ambient air temperature, the ambient air temperature is kept at 10, 20 and 30 °C. In these simulations, the solid mass fraction of the slurry entering the generator is kept at $w_c = 0.20$. Figure 7.1 shows the results of these simulations.
Figure 7.1a shows the cooling capacity of the generator. The cooling capacity increases with increasing TBAB slurry mass flow rate. The power consumption of the slurry pump is calculated by making use of the pump characteristics. The slurry flow rate and the pressure drop over the generator circuit determine the power consumption of the pump. Figure 7.1b shows the power consumption of the pump. The ambient air temperature has a negligible influence on the power consumption of the slurry pump and very little influence on the cooling capacity of the generator. Figure 7.1c shows the power consumption of the condensing unit. The power consumption of the condensing unit also increases for an increasing TBAB slurry mass flow rate.

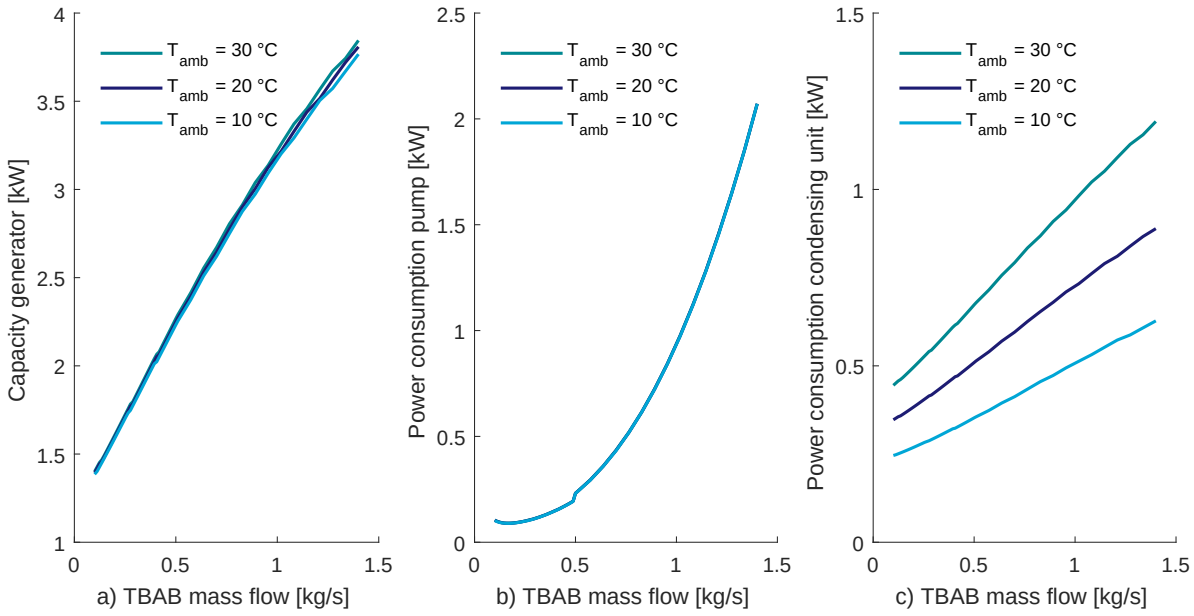

Figure 7.1: The cooling capacity of the generator, power consumption of the pump and power consumption of the condensing unit for increasing TBAB mass flow rate and different ambient temperatures. The super heating degree of the primary refrigerant is kept at 3 K.

In order to determine the most optimal mass flow rate, the cooling capacity of the generator and the power consumption of the pump are used to calculate the useful cooling capacity in equation 7.1. Firstly, the TBAB slurry is heated up in the pump and thereafter the slurry is cooled down in the generator.

$$\dot{Q}_{cool} = \dot{Q}_{gen} - \dot{W}_{pump} \tag{7.1}$$

The optimal mass flow rate maximizes the ratio between the useful cooling capacity and the total power consumption of the generator loop. This ratio is calculated in equation 7.2.

$$ratio = \frac{\dot{Q}_{gen} - \dot{W}_{pump}}{\dot{W}_{pump} + \dot{W}_{fan} + \dot{W}_{comp}} \tag{7.2}$$

Figure 7.2 shows the ratio from equation 7.2 for varying mass flow rates and different ambient temperatures. The solid mass fraction of the slurry at the inlet is kept at 0.20. The optimal mass flow rate is around 0.25 kg/s for these operating conditions.

The influence of the solid mass fraction of the slurry and the maximum temperature difference at the inlet of the generator on the optimal mass flow rate is also investigated. The maximum temperature difference between the slurry and the primary refrigerant at the inlet of the generator is set at 4 and 5 K. In the generator lower evaporating temperatures should be avoided since a too low wall temperature results in very rapid crystallization may causing blockages [105]. Table 7.1 shows the optimal mass flow rate and the corresponding ratio for different operating conditions. The maximum ratio of 4.44 is achieved for a TBAB solution and mass flow rate of 0.26 kg/s and an ambient air temperature of 10 °C. Under these favourable operating conditions, the ratio is lower than expected. This is mainly due to low pump efficiency. The low pump efficiency results in a lower useful cooling capacity and a higher energy consumption. The pumps of the actual system should be replaced with more efficient pumps.

In addition, the optimal mass flow rate corresponds to a capacity of the generator. This capacity should be sufficient to meet the cooling demand. During night time, the hydrate crystal production rate should be sufficient to meet the solid mass fraction requirement. In this case, the efficiency should dictate the mass flow rate unless the solid mass fraction requirements cannot be met. During the day, the capacity should meet the cooling demand when the crystal mass fraction reaches the set minimum. In this case, the capacity should dictate the mass flow rate.

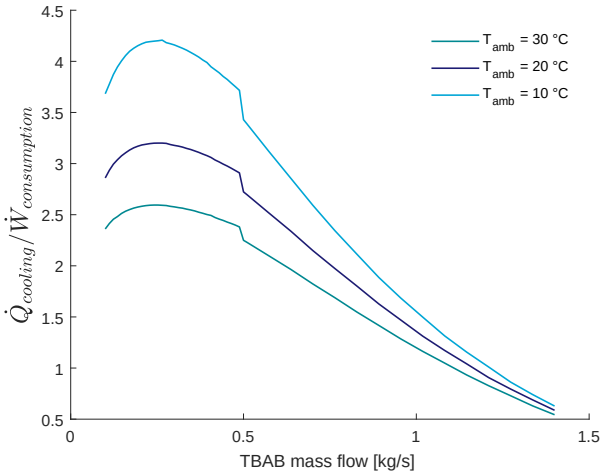

Figure 7.2: Ratio between the cooling capacity of the generator and power consumption of the generating side. The solid mass fraction at the inlet is kept at 0.20 while the maximum temperature difference at the inlet of the generator is kept at 4 K. The slurry flow becomes turbulent in the connecting tubes around 0.5 kg/s.

Table 7.1: Optimal mass flow rate of TBAB in the generator for different operating conditions.

$w_{c,in}$ [-]	$\Delta T_{evap,max}$ [K]	T_{amb} [°C]	$\dot{m}_{opt}$ [kg/s]	ratio [-]
0.00	4	10	0.26	4.44
		20	0.26	3.34
		30	0.26	2.68
	5	10	0.25	4.36
		20	0.26	3.32
		30	0.26	2.65
0.20	4	10	0.25	4.23
		20	0.25	3.22
		30	0.26	2.61
	5	10	0.25	4.28
		20	0.26	3.28
		30	0.25	2.63
0.40	4	10	0.21	3.90
		20	0.21	3.01
		30	0.20	2.47
	5	10	0.20	4.22
		20	0.21	3.22
		30	0.20	2.61

7.2. Optimal air cooler mass flow rate

The mass flow of the air cooler is also optimized by minimizing the ratio between the cooling capacity and the power consumption of the utilization side. The slurry mass flow rate is varied in these simulations. The solid mass fraction of the slurry at the inlet of the air cooler is set at 0.00, 0.05, 0.10 and 0.20. The air temperature at the inlet of the air cooler is kept at a constant temperature of 21.0 °C. The air mass flow rate is also kept constant at 0.5 kg/s based on the velocity measurements in the air ducts.

Figure 7.3 shows the results of these simulations. Figure 7.3a shows an increasing cooling capacity for an increasing slurry mass flow rate. At high slurry mass flow rates, the cooling capacity approaches a constant value. At this point the capacity of the air cooler is limited by the air mass flow rate and the temperature difference between the slurry and the air. Also, the capacity of the air cooler initially increases for a higher solid mass fraction, but when the solid mass fraction keeps increasing the capacity slightly decreases because of the reduced convection: the flow velocity is lower at higher solid mass fraction for an equal mass flow rate and hydrate crystals stabilize the flow reducing the modified Reynolds number.

Figure 7.3b shows that the power consumption of the distribution pump mainly depends on the mass flow

rate. The solid mass fraction has little influence on the power consumption of the pump compared to mass flow rate. However, solid mass fractions above 40 wt% should be avoided because of a sudden increase in the pressure drop [105]. The results of the simulation are used to determine the optimal TBAB mass flow rate.

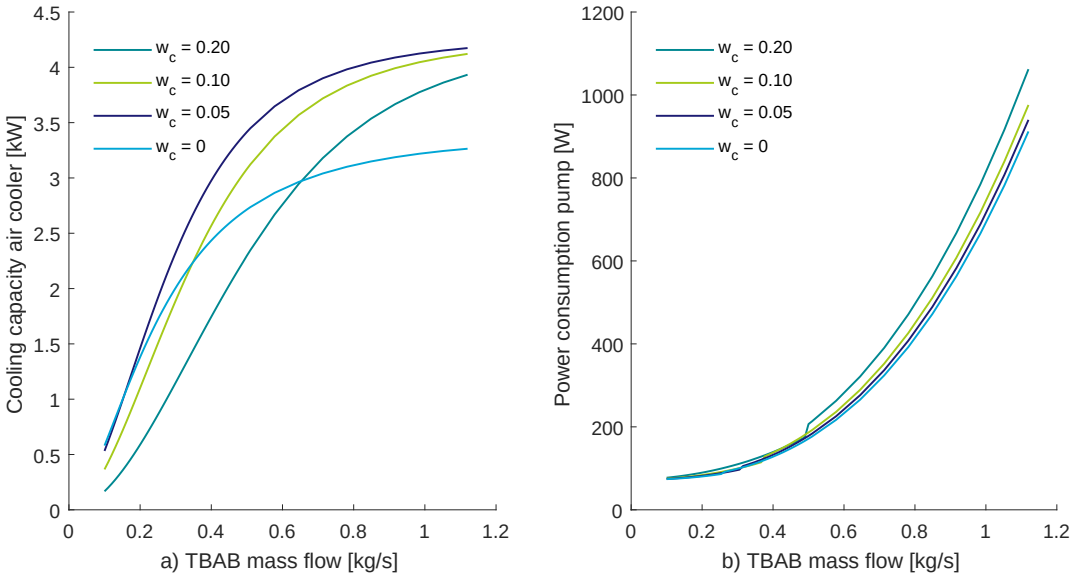

Figure 7.3: The cooling capacity of the air cooler and power consumption of the pump for increasing slurry mass flow rate and varying solid mass fractions.

The optimal mass flow rate maximizes the ratio between the cooling capacity and the power consumption of the utilization side of the system. This ratio is calculated in equation 7.3. Figure 7.4 shows this ratio for different solid mass fractions and the same operating conditions as mentioned before. Initially the ratio increases for increasing solid mass fraction. When the solid mass fraction of the slurry exceeds 0.10 the ratio decreases due to reduced convection. Figure 7.3 also shows some discontinuities. These discontinuities are caused because the slurry flow becomes turbulent in the connecting pipes at the utilization side of the system. The flow in the connecting tubes becomes turbulent at higher mass flow rates for increasing solid mass fractions because of the relaminarization effect.

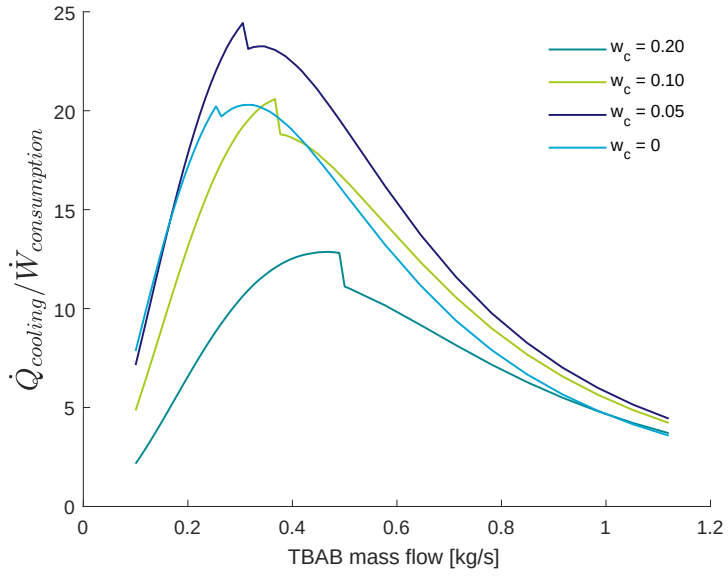

Figure 7.4: Ratio between the cooling capacity of the air cooler and power consumption of the utilization side. The solid mass fraction at the inlet of the air cooler is varied.

$$ratio = \frac{\dot{Q}_{cool}}{\dot{W}_{pump} + \dot{W}_{fan}} \tag{7.3}$$

In order to determine the influence of the air mass flow rate on the optimal TBAB mass flow rate, simulations with different air mass flow rates are carried out. Table 7.2 shows the results for several operating conditions. The optimal mass flow rate increases with increasing air mass flow. However, the ratio decreases for higher mass flow rates and solid mass fractions. Although a high ratio is preferable, the mass flow rate should be dictated by the cooling demand. Also, a low solid mass fraction is not preferable: when the solid mass fraction is below the set point during the day, the generator needs to cool down the slurry during the day when the ambient temperatures are higher. This results in a higher overall energy consumption as mentioned in section 7.1. Therefore, the solid mass fraction should be sufficient to meet the cooling requirement during the day.

Table 7.2: Optimal mass flow rate of TBAB in the air cooler for different operating conditions.

$w_{c,in}$ [-]	$\dot{m}_{air}$ [kg/s]	capacity [kW]	$\dot{m}_{opt}$ [kg/s]	ratio [-]
0.00	0.20	0.73	0.14	85.0
	0.35	1.46	0.24	38.9
	0.50	1.75	0.25	20.1
0.05	0.20	0.78	0.15	79.7
	0.35	1.55	0.26	41.6
	0.50	2.03	0.31	24.2
0.10	0.20	0.87	0.17	54.4
	0.35	1.63	0.28	31.8
	0.50	2.31	0.37	20.2
0.20	0.20	1.01	0.21	22.8
	0.35	1.77	0.33	16.9
	0.50	2.64	0.47	12.3

7.3. Optimal storage vessel volume

The storage vessel could be optimized by changing the volume of the storage vessel. By changing the volume of the storage vessel, the cooling capacity of the system can be changed. During the day, the crystals will melt in the air cooler. Eventually the solid mass fraction of the slurry reaches a certain level and the generator starts working during the day. When the volume of the storage vessel is sufficient, less efficient day time operation of the compressor can be avoided. However, increasing the storage vessel volume also increases the initial investment costs since a larger storage vessel and more TBAB is required. Because the volume of the storage vessel affects the performance of the whole system, the influence of the volume on the overall efficiency of the system will be discussed in section 8.3.4.

7.4. Conclusion

The mass flow rate of TBAB is varied to minimize the ratio between the cooling capacity and the power consumption of the system. The optimal mass flow rate of the generation side of the system lies between 0.20-0.26 kg/s depending on the operating conditions. During night-time, the mass flow rate should be dictated by the efficiency unless the hydrate production rate is not sufficient to meet the solid mass fraction requirements at the end of the night. During the day, the cooling demand should dictate the mass flow rate when the solid mass fraction becomes lower than the minimal allowed solid mass fraction.
The optimal mass flow rate of the utilization side of the system lies between 0.14-0.47 kg/s depending on the operating conditions. However, the mass flow rate of the utilization side of the system should be determined by the desired cooling capacity of the air cooler. The cooling capacity corresponding to the optimal mass flow rate is in most cases insufficient.
The efficiency of the system is mainly limited by the high power consumption of the pumps. The peripheral pumps should be replaced in the end by more efficient pumps.

8

Results of simulations and Discussion

This chapter evaluates the output of the model described in chapter 5. The energetic performance of the model of the air-conditioning system with water as a secondary refrigerant is compared with energetic performance of the model of the air-conditioning system with TBAB hydrate slurry as a secondary refrigerant. In the first section, the input data of the model will be presented. Thereafter the input parameters of the models are discussed and finally the output of the models is presented. Also, the considerations arising from the results will be discussed.

8.1. Cooling demand of reference building

The air-conditioning system in Twello is used to control the room temperature of a space of around 144 m². As mentioned in section 5.7, the cooling load of the pilot system is simulated with a simple model of a reference building. This model aims to find a reasonable cooling load and room temperature during a year. The climate data necessary to determine the cooling load is described in the NEN 5060 [61]. The NEN 5060 contains hourly data of a reference climate year for the Dutch climate. More details about the reference building are discussed in section 5.7. Figure 8.1 shows the cooling and heating load of the reference building for one year. The simulation of the reference building results in a total cooling load of 34.40 MJ/m² for 746 hours of cooling demand. The ECN reports a cooling energy demand between 31.0 MJ/m² and 59.0 MJ/m² for similar building types while the hours with a cooling demand lie between 548 and 778 per year [70]. The total amount of cooling energy is estimated to be 1,376 kWh by the model.

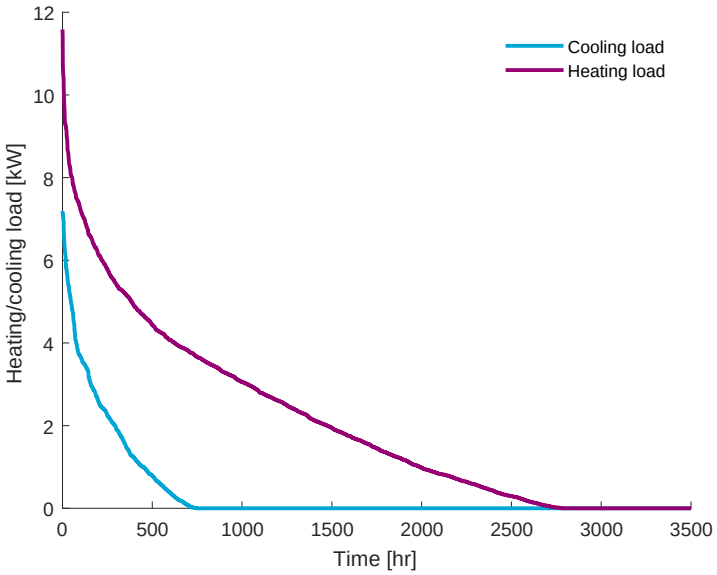

Figure 8.1: Cooling- and heating load of the reference building for a year. The cooling- and heating load is displayed per unit of area at the vertical axis while the duration of the cooling- and heating load is displayed at the horizontal axis.

8.2. Model parameters

Some of the model parameters already have been discussed in chapter 7. The capacity of the generator is usually larger for the water system compared to the TBAB system. Because of this the compressor will probably operate at partial load for the TBAB system. Therefore, it is desirable to control the fan speed of the condenser unit when the compressor operates at partial load to minimize the power consumption. Also, the efficiency of the current pumps in the system is very low. To make the simulation results for the actual system more representative, a higher pump efficiency is selected. Table 8.1 shows the input parameters of the model for the simulation. The air-conditioning system is active from 1 May till 30 September. A time step of 300 s is used for the simulations.

Table 8.1: The model parameters which are used for the simulations

Parameter	Symbol	Unit	Water system	TBAB system
Mass flow generator	$\dot{m}_{gen}$	kg/s	0.40	0.30
Mass flow air cooler	$\dot{m}_{aircooler}$	kg/s	0.05-0.5*	0.4
Pump efficiency	η_{pump}	-	0.60	0.60
Mass flow air	$\dot{m}_{air}$	kg/s	0.05-0.5**	0.05-0.5*
Evaporation temperature	T_{evap}	K	$T_{tank}-4$	$T_{tank}-4$
Start generation	T_{tank}, w_c	K, -	T_{tank} ≥8°C or t = 23:00 h	$w_{c,tank}$ = 0.05 or t = 23:00 h
Stop generation	T_{tank}, w_c	K, -	T_{tank} ≤6°C	$w_{c,tank}$ ≥ 0.40 (night) $w_{c,tank}$ ≥ 0.10 (day)

* Controlled to reach the desired cooling capacity
** Controlled to reach an outlet air temperature of 16 °C

8.3. Simulation results

The simulations are carried out for the model of the air-conditioning system with water and TBAB hydrate slurry as secondary distribution fluid. Figure 8.2 shows the desired cooling capacity during four days in the summer. The delivered cooling capacity of the TBAB air-conditioning system is also showed.

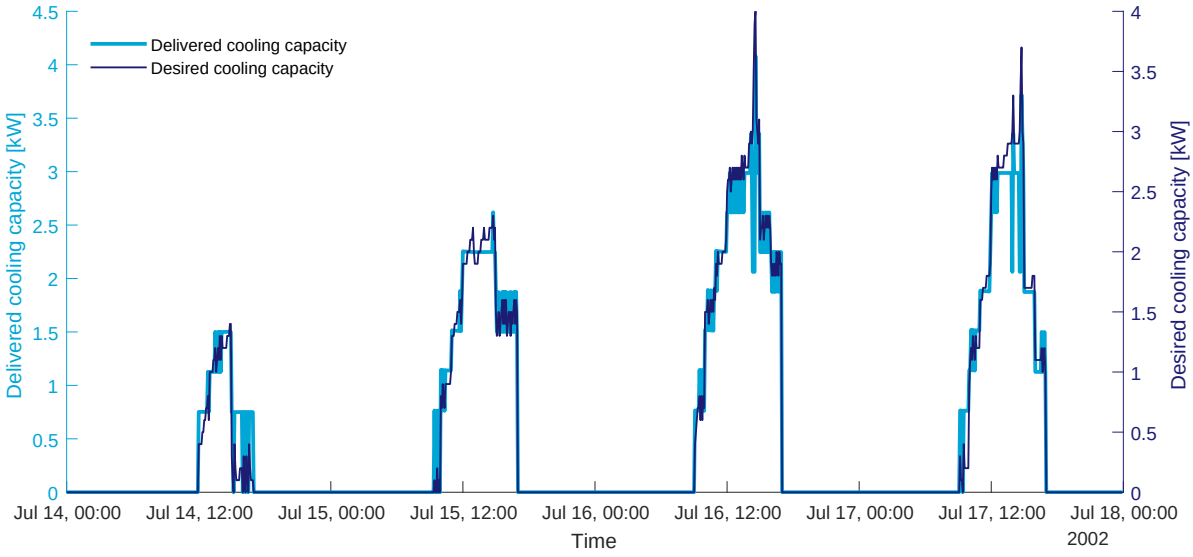

Figure 8.2: The desired and delivered cooling capacity of the TBAB air-conditioning system. The cooling demand and the cooling capacity of the air cooler are calculated by the model for four days in the summer.

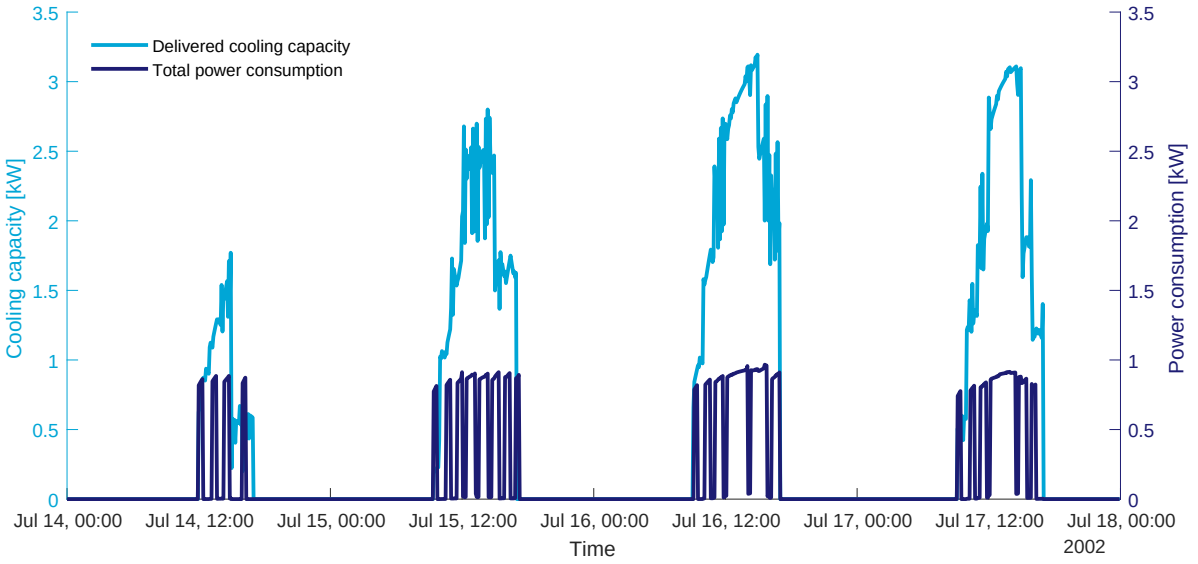

Figure 8.3: The cooling capacity and total power consumption of the water air-conditioning system.

Figure 8.3 shows the delivered cooling capacity and the total power consumption of the water air-conditioning system for four consecutive days in the summer. The system only becomes active when there is a cooling demand. Therefore, the system mainly operates during the day when ambient air temperatures are higher. This affects the total performance of the water air-conditioning system.

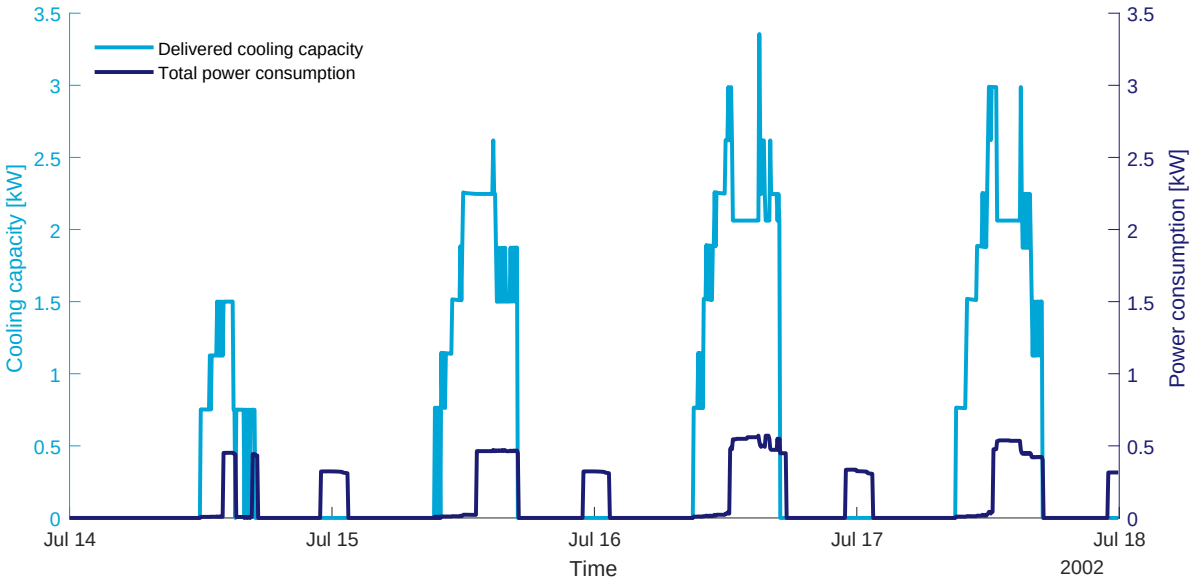

Figure 8.4: The cooling capacity and total power consumption of the TBAB air-conditioning system. The power consumption is partially shifted to night-time.

Figure 8.4 shows the delivered cooling capacity and the total power consumption of the TBAB air-conditioning system for the same period. The load of the system is partially shifted to night-time when ambient temperatures are lower. This results in an overall higher system efficiency compared to the water system. The TBAB system starts at 23:00 the crystal generation process until the solid mass fraction reaches 40%. During the day when there is a cooling demand, the crystals melt in the air cooling. When the solid mass fraction of the slurry reaches 5% during the day, the generator starts producing crystals until the solid mass fraction reaches a certain level. This process repeats itself every day.

8.3.1. Power consumption

During the simulations the power consumption of each component is calculated. The power consumption of each component is shown in table 8.2 for the TBAB and water air-conditioning system. The simulation is carried out for the cooling period from May till October. Table 8.2 shows that the compressor mainly accounts for the power consumption of the system. The compressor accounts for 84.1 % of the total energy consumption for the water system. By making use of 36.5 wt% TBAB solution the power consumption of the compressor reduces by 24.8 %. However, the TBAB system requires more power for distribution of the fluid. The overall system efficiency increase of the TBAB system will be evaluated by comparing the COP of both systems. The COP of the air-conditioning system is defined as:

$$COP = \frac{\dot{Q}_{cool}}{\Sigma \dot{W}_{elec}} \tag{8.1}$$

The COP of the air-conditioning system increases from 3.27 to 4.30

Table 8.2: The power consumption of the components of the air-conditioning system during one cooling period from May till October.

Component	Water system [kWh]	TBAB system [kWh]	Reduction [%]
Compressor	320.3	240.8	24.8
Condenser fan	35.9	28.6	20.3
Generator pump	7.2	17.3	-140.3
Air cooler pump	2.1	4.5	-114.3
Air cooler fan	15.3	18.7	-22.2
Electricity consumption generation side	363.5	286.7	21.1
Electricity consumption utilization side	17.4	23.2	-33.3
Total electricity consumption	380.8	309.9	18.6
COP [-]	3.27	4.30	

8.3.2. Initial TBAB mass fraction

The initial concentration of TBAB in the aqueous solution dictates the phase change temperature. The phase change temperature has influence on the overall efficiency of the air-conditioning system. The initial concentration of 36.5 wt% corresponds to the highest crystallization temperature of a TBAB aqueous solution and ensures that only type A hydrates can form. Therefore, the initial mass fraction of 36.5 wt% has been selected. However, such a high initial TBAB mass fraction has also some drawbacks:

- The hydrate phase diagram becomes very flat for higher initial TBAB mass fractions: very small temperature changes correspond to large variations in the hydrate mass fraction [16].
- The investment cost increases with increasing initial TBAB mass fraction.
- The pressure drop of the fluid increases with increasing initial TBAB mass fraction [103].
- The hydrate crystals adhere more strongly for increasing initial TBAB mass fraction resulting in a larger pressure drop in the generator [14].

Therefore the influence on the initial TBAB mass fraction on the air-conditioning system performance is also investigated. A 36.5 wt% TBAB solution results in the highest possible phase change temperature, see figure 3.1. Thus, higher initial TBAB mass fractions result in a lower phase equilibrium temperature and the disadvantages mentioned above to an increased extent. A lower initial TBAB mass fraction is also limited because of the formation of the type B hydrate crystals. The model is no longer valid when type B hydrate crystals are formed. Therefore, the lowest initial TBAB mass fraction is limited to 25 wt%. The simulations for different initial TBAB mass fractions are carried out for the period of May till October.
Figure 8.5 shows the COP of the air-conditioning system for varying initial TBAB mass fractions. Also, the total energy consumption and the energy consumption of the pumps of the air-conditioning system are shown.

The total power consumption of the system is mainly dependent on the power consumption of the compressor. The best way to maximize the COP of the air-conditioning and minimize the power consumption of the compressor is to maximize the evaporation temperature. However, a higher initial TBAB mass fraction also results in a higher shear force required to remove the TBAB hydrates. This results in a thicker crystal layer

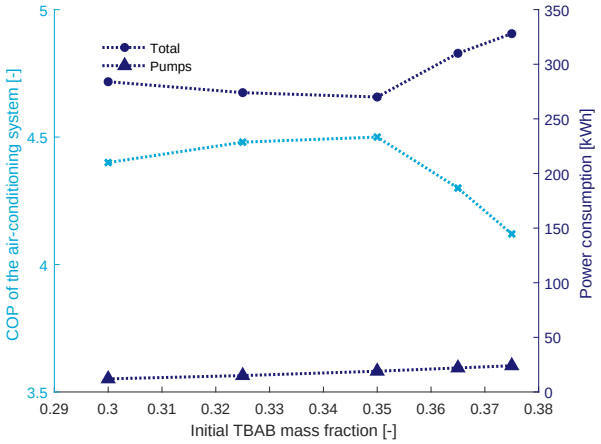

Figure 8.5: The performance of the air-conditioning for varying initial TBAB mass fractions.

in the generator. Because of the increased crystal layer thickness, the power consumption of the compressor increases due to an increased thermal resistance.

The simulations predict the highest COP of 4.50 for an initial mass fraction of 35 wt%. The COP of the air-conditioning system suddenly decreases for higher initial mass fractions. This is probably caused by the increased shear force required to remove the crystals as shown in figure 5.6 and the increased viscosity described by the Vogel-Tamman Fulche model as shown in figure 3.5.

8.3.3. Generation starting time

The crystal generation process generally starts at 23:00 when the cooling capacity of the crystals in the storage vessel is sufficient during the day. However, the ambient temperatures are not at the lowest possible level at 23:00. Therefore, the starting time of the night-time crystal generation process is evaluated. The time it takes to reach a solid mass fraction of 0.40 should also be taken into account. Simulations show it takes around 3 hours to reach a solid mass fraction of 0.40 from the lowest allowable solid mass fraction of 0.05 dictated by the operating conditions in section 8.2.

Figure 8.6 shows the COP for varying starting times of the generation process. The reduction of the total energy consumption is marginal. This results in very small improvements of the overall performance of the system. The COP of the system increases from 4.30 to 4.36 when the generation starting time shifts from 23:00 to 2:00. The slightly higher temperature of the slurry in the tank before the generation process, due to the lower solid mass fraction, does not reduce the energy losses of the storage vessel. Although the performance increase is very small, the performance increase can be acquired by only adjusting the starting time of the crystal generation process.

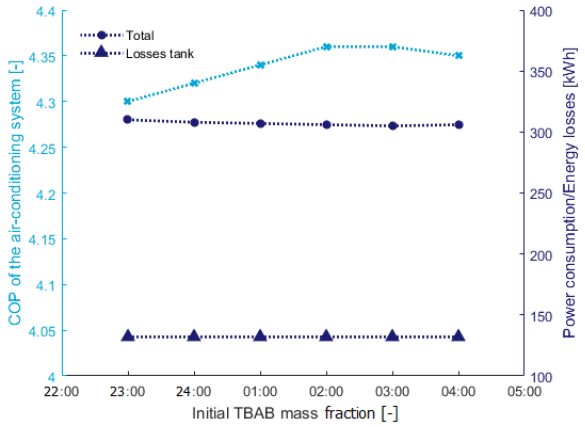

Figure 8.6: The performance of the air-conditioning for varying starting times of the crystal generation process. The energy losses in the storage vessel do not change for varying generation starting times. The total power consumption reduces slightly.

8.3.4. Capacity of storage vessel

The capacity of the storage tank is not every day sufficient to cover the cooling demand. Therefore, the capacity of the storage tank should be considered. The capacity of the storage tank depends on the volume of the storage tank, the solid mass fraction of the slurry, the initial TBAB mass fraction and the hydrate types in the slurry. In this research only initial TBAB mass fractions are considered for which type A TBAB hydrates are formed. Type B hydrate generally forms at lower temperatures, reducing the overall performance of the air-conditioning system. Also the solid mass fraction of the slurry should not exceed 40 wt% to maintain the slurry pumpable [104, 105]. Therefore, only the volume of the storage vessel is considered. The solid mass fraction of the slurry varies between 5-40 wt% as mentioned in section 8.2.
The simulations show a COP of 4.06 and 4.34 for a storage vessel volume of 150 l and 600 l respectively. Since the increase of the performance is limited for a larger storage vessel, the storage vessel should be minimized in order to reduce the initial investment costs. However, a small storage vessel limits the energetic advantages of the hydrate crystal generation during night-time. An optimum storage vessel size should be considered from an economic perspective.

8.4. Conclusion

The results of the simulations are presented in this chapter. The cooling load is calculated with a simple model of a building with a floor space of 144 m². The climate data from the NEN5060 are used as input data for the calculation of the cooling load. The cooling load corresponds to the cooling load of similar building types.
The model predicts an increased COP from 3.27 to 4.30 when TBAB hydrate slurry is used as a secondary distribution fluid instead of water. The total power consumption of the air-conditioning system is reduced by 18.6 %. This is mainly due to the reduced energy consumption of the compressor.
The COP of the air-conditioning system is also calculated for varying initial TBAB mass fractions. The simulations show the highest COP of 4.50 for an initial TBAB mass fraction of 35wt%.
The starting time of the crystal generation processes also influences the overall performance of the system. The COP can be increased from 4.30 to 4.36 by changing the starting time of the generation process from 23:00 to 2:00. Although the performance increase is small, it can be easily achieved by changing one setting.
To improve the performance of the air-conditioning system the volume of the storage vessel is also considered. Increasing the volume of the storage tank prevents the compressor from operating during the day. However, the increased performance comes at the expense of higher investment costs. The simulations showed a COP of 4.06 and 4.34 for a storage vessel of 150 l and 600 l respectively.

9

Conclusions and Recommendations

In this thesis the main researched question includes the quantification of the coefficient of performance of the air-conditioning system in Twello by using TBAB clathrate hydrate slurry as a secondary loop refrigerant instead of water. The energetic performance of the air-conditioning system is calculated by the model for both water and a 36.5wt% TBAB solution as secondary loop refrigerant and the conclusions of every chapter will be summarized in this chapter. Also, recommendations to improve the pilot system, continue the current research and new research topics which follow from the current research will be addressed in this chapter.

9.1. Conclusions from previous chapters

The chapters in this thesis highlight different aspects of the research in order to verify the hypothesis. The following conclusions are made in the previous chapters:

- The properties of TBAB hydrate crystals, TBAB aqueous solution and TBAB CHS are described by several different correlations from the literature. The most suitable correlations for the model are summarized in table 3.3.
- The heat transfer and pressure drop characteristics of TBAB aqueous solution and CHS are also described by several different correlations from the literature.
- The equations and correlations which are used to model the pilot plant are reviewed in chapter 5. Each component of the pilot plant is modelled in Matlab as a function. Also, the properties, heat and pressure drop correlations of the fluid from chapters 3 and 4 are implemented in the model. The model is solved iteratively for each time step of 300 s to simulate the behaviour of the pilot system.
- Each component of the model is validated with experimental data of the pilot system in Twello. The model is able to predict the behaviour of the compressor, the condenser and the pumps. The capacity of the air cooler is also predicted by the correlation of the VDI heat atlas [89]. The heat transfer and pressure drop characteristics of the primary refrigerant, R134a, are best described by the correlations of Amalfi et al. [3, 3]. The crystal production process in the generator requires more experimental data under the desired operating conditions to validate this component properly. In this manner, the crystal formation process in the generator can be further investigated.
- The mass flow of the slurry in the utilization- and generation loop of the system is optimized in order to minimize the ratio between the power consumption and the cooling capacity. During night-time, the efficiency should dictate the mass flow rate at the generation side. When the generator needs to operate during the day, the cooling demand should determine the flow rate at the generation loop. The optimal mass flow rate of the utilization side of the system lies between 0.14-0.47 kg/s depending on the operating conditions. However, the mass flow rate of the utilization side of the system should be determined by the desired cooling capacity of the air cooler. The cooling capacity corresponding to the optimal mass flow rate is in most cases insufficient to deliver the desired cooling capacity. Therefore, the flow rate must be adjusted to meet the desired cooling capacity.

These findings resulted in the final model which is used to validate the hypothesis. The conclusions following from the results of the simulations are discussed in section 9.2.

9.2. Energetic system performance

The pilot air-conditioning system in Twello is modelled with both water and a 36.5 wt% TBAB solution as secondary distribution fluid. The model is used to evaluate the energetic performance of the air-conditioning system for both secondary distribution fluids. The simulations were carried out for a period from May to October. In this period there is a cooling demand in the Netherlands. The cooling load of the model is acquired by a model of a building of 144 m² in the Netherlands. Climate data from the NEN5060 are used as input data for the dynamic model of the cooling load [61]. The climate data give a hourly description of the conditions while the model calculates for every 300 seconds the conditions of the system and the building.

- The simulations show a COP of the air-conditioning system of 3.27 when water is used as a secondary distribution fluid. The COP of the system increases to 4.30 when a 36.5 wt% TBAB solution is used as secondary distribution fluid. The simulations show a reduction of 18.6 % of the total energy consumption for the TBAB system.
- The compressor contributes the most to the total power consumption of both systems. The compressor accounts for 84.1 % of the total energy consumption for the water system. By making use of TBAB hydrate slurry as a secondary distribution fluid the power consumption reduces with 24.8 % and accounts for 77.7 % of the total energy consumption. The higher evaporation temperature of the primary refrigerant in the generator and the lower condensation temperature in the condenser cause this energy reduction of the compressor. Shifting the compressor load to night-time allows the lower condensation temperature, while the phase equilibrium temperature of the TBAB solution enables a higher evaporation temperature in the generator compared to water as a secondary distribution fluid. The energy consumption of the pumps increases with 134 % for the TBAB system. However, the energy consumption of the pumps accounts only for 7 % of the total energy consumption.
- The initial mass fraction of TBAB in the solution determines the phase equilibrium temperature. Also, the TBAB hydrate crystals adhere less strongly to the generator surface for lower initial TBAB mass fraction. A lower initial TBAB mass fraction reduces the friction losses in the generator and the crystal layer thickness. Therefore, the heat transfer process in the generator works more efficiently lowering the power consumption of the compressor. On the other hand, lowering the initial TBAB mass fraction lowers the phase equilibrium temperature. Because of the the lower evaporating temperature, the compressor uses more power. An initial TBAB mass fraction of 35 % shows the best trade-off between these phenomena and a COP of 4.50 could be achieved.
- The storage vessel size has a small influence on the performance increase of the system. Increasing the storage vessel size from 300 l to 600 l increases the COP from 4.30 to 4.34 when 36.5 wt% TBAB solution is used. Increasing the storage vessel size prevents the system to start the generation process during the day, when ambient temperatures are higher and more compressor work is required to cool down the slurry. Although increasing the storage vessel size has a positive effect on the performance of the system, the initial investment costs also increase. The amount of TBAB which is needed to prepare the solution, the larger storage vessel and the additional space which is required for the larger storage vessel increase the initial investment costs.
- By shifting the time when the crystal generation process starts to a time when ambient temperatures are even lower, the overall performance of the system can be increased. The model predicts a COP increase from 4.30 to 4.36 when the generation starting time is shifted from 23:00 to 2:00. Although this performance increase can easily be achieved, the benefits may vary day by day. The period of the lowest ambient temperatures varies every night. Also, the time it takes to reach a solid mass fraction of 0.40 should be considered. The model predicts a time of around 2.75 hours to increase the solid mass fraction from 0.05 to 0.40.

9.3. Hypothesis

The results of the simulations are used in order to validate the hypothesis as defined in chapter 1. The hypothesis of this thesis is as follows:

The coefficient of performance of the air-conditioning system in Twello can significantly be increased by using TBAB clathrate hydrate slurry as a secondary loop refrigerant instead of water.

The hypothesis is validated by a model of the air-conditioning system in Twello. The model simulations predict a COP of 4.30 and 3.27 for the air-conditioning system with TBAB clathrate hydrate slurry with an initial TBAB mass fraction of 36.5 wt% and water as a secondary loop refrigerant respectively. This corresponds to an energy reduction of 18.6% when a 36.5 wt% TBAB solution is used as secondary loop refrigerant. The hypothesis holds under the operating conditions presented in section 8.2 and the assumptions from chapter 5.

9.4. Recommendations

During this research several new insights were gained to improve or expand on current or further research. First of all, possible improvements of the pilot system are discussed. Secondly, possibilities of the continuation of the current research will be addressed. Lastly, topics which result from the current research and might be suitable for future studies are discussed.

9.4.1. Improvements of the pilot system

- As for now, the crystal generation process during the night-time starts at 23:00. By shifting the starting time of the generation process to a later time when the ambient temperatures are generally even lower, a higher system performance could be achieved. Also, this adjustment decreases the thermal losses of the storage tank.
- The pilot system currently uses peripheral pumps with a low efficiency. These pumps should be replaced in the end by more efficient ones in order to increase the system performance.
- The condensation pressure of the primary refrigerant should be further reduced for lower ambient temperatures.
- The evaporation pressure of the primary refrigerant is set at a specific level. The compressor is controlled by the desired evaporation pressure. However, the operating conditions of the generator can be further improved by controlling the evaporation pressure. Also, too rapid crystallization can be prevented by controlling the evaporation pressure.
- The fan of the condensing unit is not speed controlled. Controlling the speed of the condenser fan increases the performance of the system when for instance the compressor operates at partial load.
- The capacity of the equipment of the pilot system is based on water as a secondary distribution fluid. Therefore, the compressor usually operates at partial load when a TBAB solution is used as a secondary distribution fluid. It should be assessed if the compressor operates efficiently under these conditions.
- It should be considered to slightly lower the TBAB mass fraction of the solution. The simulations show a higher COP for an initial TBAB mass fraction of 35 wt%. An additional advantage of the lower TBAB mass fraction is a less flat phase diagram. Therefore, the solid mass fraction of the slurry does not change very rapidly for a very small temperature change.

9.4.2. Continuation of the current research

- The model assumes that the TBAB solution or slurry is always at phase equilibrium. The possibility of a supercooled solution or slurry is not implemented in the model. Therefore, the crystals are only produced in the generator and do not grow for instance in the storage vessel. The implementation of supercooling of the solution and slurry should be considered.
- The most suitable correlation of the Sherwood number which describes the mass transfer inside the generator should be evaluated. Additional experimental data of the hydrate generation process should help in the determination of the most suitable correlation.

- The model assumes a crystal layer with a similar thickness on the entire surface of the generator. Therefore, the crystal production rate is perhaps overestimated. Additional experimental data should give a clear insight in the crystal production rate.
- The cooling load is obtained by a dynamic model of a reference building in the Netherlands. The hourly climate data of one year from the NEN5060 are used as input data for this model [61]. The model for the cooling load could be extended or replaced by a more advanced modelling approach. Also, the resolution of the climate data could be increased.

9.4.3. Future research topics

- The correlation of scrapping force which is required to remove the initially and repeatedly formed TBAB hydrates is based on a brass surface [14]. The required scrapping force for different initial TBAB mass fractions on a stainless steel surface should be examined.
- The correlations of the properties of a TBAB slurry and solution, which are used in the model, are based on studies which have been using TBAB of a higher purity. The influence of the purity of the TBAB on the properties of the solution and slurry should be investigated.
- The TBAB which is used in the pilot system has a purity of at least 96%. The main contaminant is silicon dioxide. It is not known how this contaminant influences the lifespan of the air-conditioning system.
- An economic analysis of the whole system lifespan should be carried out in order to determine the feasibility of the large scale application of air-conditioning systems with TBAB hydrate slurry as a secondary refrigerant.
- The performance of systems with other clathrate hydrate slurries and microencapsulated phase change materials slurries such as TBAC and TBAF should be investigated [97].
- The TBAB hydrate production in a generator in a controlled environment is not investigated yet. Ma and Zhang investigated the heat transfer and pressure drop characteristics of TBAB hydrate slurry in a plate heat exchanger [49]. The pressure drop was measured for varying flow rates and solid mass fractions while the heat transfer characteristics were determined by melting the hydrate slurry in the generator by a hot water flow.
- The hydrate generation process starts during night-time. However, with the increasing adoption of alternative energy resources such as solar- and wind energy, an energy surplus can arise during the day. Therefore, it can become economically feasible to start the generation process during the day when there is an excess of energy. The implementation of these energy storage systems in a smart grid can be investigated.
- The possibilities of further improvements of the system should be evaluated. Varying the starting time of the crystal generation process and initial mass fraction of TBAB influence the performance of the system. For instance, different mass flow rates for varying solid mass fraction and cooling capacities might also further improve the system performance.

Bibliography

[1] Abu-Khader, M. M. Plate heat exchangers: Recent advances. *Renewable and Sustainable Energy Reviews*, 16(4):1883 – 1891, 2012. ISSN 1364-0321. doi: https://doi.org/10.1016/j.rser.2012.01.009. URL http://www.sciencedirect.com/science/article/pii/S136403211200010X.

[2] Agyenim, F., Hewitt, N., Eames, P., and Smyth, M. A review of materials, heat transfer and phase change problem formulation for latent heat thermal energy storage systems (lhtess). *Renewable and Sustainable Energy Reviews*, 14(2):615 – 628, 2010. ISSN 1364-0321. doi: https://doi.org/10.1016/j.rser.2009.10.015. URL http://www.sciencedirect.com/science/article/pii/S1364032109002469.

[3] Amalfi, R. L., Vakili-Farahani, F., and Thome, J. R. Flow boiling and frictional pressure gradients in plate heat exchangers. part 1: Review and experimental database. *International Journal of Refrigeration*, 61:166–184, 2016. ISSN 0140-7007. doi: http://dx.doi.org/10.1016/j.ijrefrig.2015.07.010. URL http://www.sciencedirect.com/science/article/pii/S014070071500208X.

[4] Amalfi, R. L., Vakili-Farahani, F., and Thome, J. R. Flow boiling and frictional pressure gradients in plate heat exchangers. part 2: Comparison of literature methods to database and new prediction methods. *International Journal of Refrigeration*, 61:185–203, 2016. ISSN 0140-7007. doi: http://dx.doi.org/10.1016/j.ijrefrig.2015.07.009. URL http://www.sciencedirect.com/science/article/pii/S0140700715002078.

[5] Arsenyeva, O. P., Crittenden, B., Yang, M., and Kapustenko, P. O. Accounting for the thermal resistance of cooling water fouling in plate heat exchangers. *Applied Thermal Engineering*, 61(1):53–59, 2013. ISSN 1359-4311. doi: http://dx.doi.org/10.1016/j.applthermaleng.2013.02.045. URL http://www.sciencedirect.com/science/article/pii/S1359431113001877.

[6] Arsenyeva, O. P., Tovazhnyanskyy, L. L., Kapustenko, P. O., Khavin, G. L., Yuzbashyan, A. P., and Arsenyev, P. Y. Two types of welded plate heat exchangers for efficient heat recovery in industry. *Applied Thermal Engineering*, 105:763–773, 2016. ISSN 1359-4311. doi: http://dx.doi.org/10.1016/j.applthermaleng.2016.03.064. URL http://www.sciencedirect.com/science/article/pii/S135943111630357X.

[7] Asaoka, T., Kumano, H., and Serita, M. Measurement of latent heat of tetra-n-butylammonium bromide (tbab) hydrate. *International Journal of Refrigeration*, 36(3):992–997, 2013. ISSN 0140-7007. doi: http://dx.doi.org/10.1016/j.ijrefrig.2012.12.011. URL http://www.sciencedirect.com/science/article/pii/S0140700712003544.

[8] Babcock, and Company, W. Steam, its generation and use. Technical Report Number v. 39, Babcock and Wilcox, 1978.

[9] Bellas, J., Chaer, I., and Tassou, S. A. Heat transfer and pressure drop of ice slurries in plate heat exchangers. *Applied Thermal Engineering*, 22(7):721–732, 2002. ISSN 1359-4311. doi: http://dx.doi.org/10.1016/S1359-4311(01)00126-0. URL http://www.sciencedirect.com/science/article/pii/S1359431101001260.

[10] Bitzer. Bitzer ecoline software, September 2017. URL https://www.bitzer.de/gb/en/products/Technologies/Reciprocating-Compressors/Semi-hermetic/For-standard-refrigerants/ECOLINE//.

[11] Bitzer. Lhe series with ecoline compressors„ September 2017. URL https://www.bitzer.de/fi/en/products/Technologies/Condensing-Units/With-semi-hermetic-compressors/Air-cooled/LHE-series-with-ECOLINE-compressors//.

[12] Briggs, D. E., and Young, E. H. Convection heat transfer and pressure drop of air flowing across triangular pitch banks of finned tubes. In *Chem. Eng. Prog. Symp. Ser*, volume 59, pages 1–10, 1963.

[13] Daitoku, T., and Utaka, Y. An effect of scraper shapes on detachment of solid adhered to cooling surface for formation of clathrate hydrate slurry. *Heat Transfer—Asian Research*, 36(8):489–500, 2007. ISSN 1523-1496. doi: 10.1002/htj.20179. URL http://dx.doi.org/10.1002/htj.20179.

[14] Daitoku, T., and Utaka, Y. Adhesion and detachment characteristics of a tbab hydrate solid on a heat transfer surface (effect of concentration of tbab solutions). *Heat Transfer—Asian Research*, 38(6):370–384, 2009. ISSN 1523-1496. doi: 10.1002/htj.20254. URL http://dx.doi.org/10.1002/htj.20254.

[15] Daitoku, T., and Utaka, Y. Separation characteristics of clathrate hydrates from a cooling plate for efficient cold energy storage. *Applied Energy*, 87(8):2682–2689, 2010. ISSN 0306-2619. doi: http://dx.doi.org/10.1016/j.apenergy.2010.03.025. URL http://www.sciencedirect.com/science/article/pii/S0306261910000899.

[16] Darbouret, M., Cournil, M., and Herri, J.-M. Crystallisation and rheology of an hydrate slurry as secondary two-phase refrigerant for air-conditioning application. In *nd Phase Change Material and Slurry Workshop & 6th IIR Ice Slurry Workshop, Switzerland*, June 2005. URL https://hal.archives-ouvertes.fr/hal-00125080.

[17] Darbouret, M., Cournil, M., and Herri, J.-M. Rheological study of tbab hydrate slurries as secondary two-phase refrigerants. *International Journal of Refrigeration*, 28(5):663–671, 2005. ISSN 0140-7007. doi: http://dx.doi.org/10.1016/j.ijrefrig.2005.01.002. URL http://www.sciencedirect.com/science/article/pii/S0140700705000216.

[18] Dodge, D. W., and Metzner, A. B. Turbulent flow of non-newtonian systems. *AIChE Journal*, 5(2):189–204, 1959. ISSN 1547-5905. doi: 10.1002/aic.690050214. URL http://dx.doi.org/10.1002/aic.690050214.

[19] Donowski, V. D., and Kandlikar, S. G. Correlating evaporation heat transfer coefficient of refrigerant r-134a in a plate heat exchanger. In *Engineering Foundation Conference on Pool and Flow Boiling, Alaska*, 2000.

[20] Douzet, J., Kwaterski, M., Lallemand, A., Chauvy, F., Flick, D., and Herri, J.-M. Prototyping of a real size air-conditioning system using a tetra-n-butylammonium bromide semiclathrate hydrate slurry as secondary two-phase refrigerant – experimental investigations and modelling. *International Journal of Refrigeration*, 36(6):1616–1631, 2013. ISSN 0140-7007. doi: http://dx.doi.org/10.1016/j.ijrefrig.2013.04.015. URL http://www.sciencedirect.com/science/article/pii/S0140700713001047.

[21] Edwards, D. K. D. K., Denny, Vernon E, j. a., and Mills, Anthony F, j. a. *Transfer processes : an introduction to diffusion, convection, and radiation*. New York : Holt, Rinehart and Winston, 1973. ISBN 003085167X. Includes bibliographical references.

[22] Egolf, P. W., Kitanovski, A., Ata-Caesar, D., Vuarnoz, D., and Meili, F. Cold storage with ice slurries. *International Journal of Energy Research*, 32(3):187–203, 2008. ISSN 1099-114X. doi: 10.1002/er.1340. URL http://dx.doi.org/10.1002/er.1340.

[23] Eldeeb, R., Aute, V., and Radermacher, R. A survey of correlations for heat transfer and pressure drop for evaporation and condensation in plate heat exchangers. *International Journal of Refrigeration*, 65:12–26, 2016. ISSN 0140-7007. doi: http://dx.doi.org/10.1016/j.ijrefrig.2015.11.013. URL http://www.sciencedirect.com/science/article/pii/S0140700715003758.

[24] Flick, D., Doursat, C., and Lakhdar, M. B. Modelling and numerical simulation of ice slurry storage tank. *Computer Aided Chemical Engineering*, 24:1169–1174, 2007. ISSN 1570-7946. doi: http://dx.doi.org/10.1016/S1570-7946(07)80219-7. URL http://www.sciencedirect.com/science/article/pii/S1570794607802197.

[25] Focke, W. W., Zachariades, J., and Olivier, I. The effect of the corrugation inclination angle on the thermohydraulic performance of plate heat exchangers. *International Journal of Heat and Mass Transfer*, 28(8):1469–1479, 1985. ISSN 0017-9310. doi: http://dx.doi.org/10.1016/0017-9310(85)90249-2. URL http://www.sciencedirect.com/science/article/pii/0017931085902492.

[26] Fujiura, K., Nakamoto, Y., Taguchi, Y., Ohmura, R., and Nagasaka, Y. Thermal conductivity measurements of semiclathrate hydrates and aqueous solutions of tetrabutylammonium bromide (tbab) and tetrabutylammonium chloride (tbac) by the transient hot-wire using parylene-coated probe. *Fluid Phase Equilibria*, 413:129–136, 2016. ISSN 0378-3812. doi: http://dx.doi.org/10.1016/j.fluid.2015.09.024. URL http://www.sciencedirect.com/science/article/pii/S0378381215301291.

[27] GISTEMP Team. Giss surface temperature analysis (gistemp), 2016. URL https://data.giss.nasa.gov/gistemp/.

[28] Gudjonsdottir, V. Analysis of external influences on an otec cycle. Master thesis, Delft University of Technology, The Netherlands, 2015.

[29] Han, D.-H., Lee, K.-J., and Kim, Y.-H. Experiments on the characteristics of evaporation of r410a in brazed plate heat exchangers with different geometric configurations. *Applied Thermal Engineering*, 23 (10):1209 – 1225, 2003. ISSN 1359-4311. doi: http://dx.doi.org/10.1016/S1359-4311(03)00061-9. URL http://www.sciencedirect.com/science/article/pii/S1359431103000619.

[30] Hansen, T. M., Radosevic, M., Kauffeld, M., and Zwieg, T. Investigation of ice crystal growth and geometrical characteristics in ice slurry (rp-1166). *HVAC&R Research*, 9(1):19–32, 2003. doi: 10.1080/10789669.2003.10391054. URL http://www.tandfonline.com/doi/abs/10.1080/10789669.2003.10391054.

[31] Hayashi, L., Takao, S., Ogoshi, H., and Matsumoto, S. Research and development on high-density cold latent-heat medium transportation technology. In *IEA annex 10, phase change materials and chemical reactions for thermal energy storage, the fifth workshop*, pages 1–9, 2000.

[32] Huang, J., Sheer, T. J., and Bailey-McEwan, M. Heat transfer and pressure drop in plate heat exchanger refrigerant evaporators. *International Journal of Refrigeration*, 35(2):325–335, 2012. ISSN 0140-7007. doi: http://dx.doi.org/10.1016/j.ijrefrig.2011.11.002. URL http://www.sciencedirect.com/science/article/pii/S0140700711002702.

[33] Infante Ferreira, C. Lecture notes wb4427 refrigeration technology and applications, 2016.

[34] International Energy Agency. World energy outlook 2016, 2016.

[35] Isaac, M., and van Vuuren, D. P. Modeling global residential sector energy demand for heating and air conditioning in the context of climate change. *Energy Policy*, 37(2):507 – 521, 2009. ISSN 0301-4215. doi: https://doi.org/10.1016/j.enpol.2008.09.051. URL http://www.sciencedirect.com/science/article/pii/S0301421508005168.

[36] Jian-Bin, H., Shao-Wu, W., Yong, L., Zong-Ci, Z., and Xin-Yu, W. Debates on the causes of global warming. *Advances in Climate Change Research*, 3(1):38 – 44, 2012. ISSN 1674-9278. doi: https://doi.org/10.3724/SP.J.1248.2012.00038. URL http://www.sciencedirect.com/science/article/pii/S1674927812500043.

[37] Kapustenko, P. O., Arsenyeva, O. P., and Dolgonosova, O. The heat and momentum transfers relation in channels of plate heat exchangers. 2011. URL http://repository.kpi.kharkov.ua/handle/KhPI-Press/27664.

[38] Kumano, H., Saito, A., Okawa, S., and Goto, Y. Study on fundamental characteristics of tbab hydrate slurry. *Transactions of the Japan Society of Mechanical Engineers Series B*, 72(724):3089–3095, 2006. doi: 10.1299/kikaib.72.3089.

[39] Kumano, H., Hirata, T., and Kudoh, T. Experimental study on the flow and heat transfer characteristics of a tetra-n-butyl ammonium bromide hydrate slurry (second report: Heat transfer characteristics). *International Journal of Refrigeration*, 34(8):1963–1971, 2011. ISSN 0140-7007. doi: http://dx.doi.org/10.1016/j.ijrefrig.2011.06.003. URL http://www.sciencedirect.com/science/article/pii/S0140700711001435.

[40] Kumano, H., Hirata, T., and Kudoh, T. Experimental study on the flow and heat transfer characteristics of a tetra-n-butyl ammonium bromide hydrate slurry (first report: Flow characteristics). *International Journal of Refrigeration*, 34(8):1953–1962, 2011. ISSN 0140-7007. doi: http://dx.doi.org/10.1016/j.ijrefrig.2011.06.002. URL http://www.sciencedirect.com/science/article/pii/S0140700711001423.

[41] Kumano, H., Hirata, T., and Kobayashi, Y. Flow and heat transfer characteristics of a tetra-n-butyl ammonium bromide hydrate slurry in the transition region. *International Journal of Refrigeration*, 35(8):2085–2092, 2012. ISSN 0140-7007. doi: http://dx.doi.org/10.1016/j.ijrefrig.2012.08.011. URL http://www.sciencedirect.com/science/article/pii/S0140700712001983.

[42] Kumar, H. The plate heat exchanger: construction and design. *Institute of Chemical Engineering Symposium Series*, 86:1275–1288, 1984.

[43] Lemmon, E., Huber, M., and McLinden, M. Refprop: Reference fluid thermodynamic and transport properties. *NIST standard reference database*, 2007.

[44] Li, D., Liang, D., Peng, H., and Wan, L. Thermal conductivities of methane–methylcyclohexane and tetrabutylammonium bromide clathrate hydrate. *Journal of Thermal Analysis and Calorimetry*, 123(2): 1391–1397, 2016. ISSN 1588-2926. doi: 10.1007/s10973-015-5065-3. URL http://dx.doi.org/10.1007/s10973-015-5065-3.

[45] Li, G., Hwang, Y., and Radermacher, R. Review of cold storage materials for air conditioning application. *International Journal of Refrigeration*, 35(8):2053–2077, 2012. ISSN 0140-7007. doi: http://dx.doi.org/10.1016/j.ijrefrig.2012.06.003. URL http://www.sciencedirect.com/science/article/pii/S0140700712001491.

[46] Li, W., Li, H.-x., Li, G.-q., and Yao, S.-c. Numerical and experimental analysis of composite fouling in corrugated plate heat exchangers. *International Journal of Heat and Mass Transfer*, 63:351–360, 2013. ISSN 0017-9310. doi: http://dx.doi.org/10.1016/j.ijheatmasstransfer.2013.03.073. URL http://www.sciencedirect.com/science/article/pii/S0017931013002913.

[47] Lipkowski, J., Komarov, V. Y., Rodionova, T. V., Dyadin, Y. A., and Aladko, L. S. The structure of tetrabutylammonium bromide hydrate (c4h9)4nbr·21/3h2o. *Journal of Supramolecular Chemistry*, 2 (4–5):435–439, 2002. ISSN 1472-7862. doi: http://dx.doi.org/10.1016/S1472-7862(03)00054-6. URL http://www.sciencedirect.com/science/article/pii/S1472786203000546.

[48] Longo, G. A., and Gasparella, A. Refrigerant r134a vaporisation heat transfer and pressure drop inside a small brazed plate heat exchanger. *International Journal of Refrigeration*, 30(5):821–830, 2007. ISSN 0140-7007. doi: http://dx.doi.org/10.1016/j.ijrefrig.2006.11.011. URL http://www.sciencedirect.com/science/article/pii/S0140700706002520.

[49] Ma, Z. W., and Zhang, P. Pressure drop and heat transfer characteristics of clathrate hydrate slurry in a plate heat exchanger. *International Journal of Refrigeration*, 34(3):796–806, 2011. ISSN 0140-7007. doi: http://dx.doi.org/10.1016/j.ijrefrig.2010.12.022. URL http://www.sciencedirect.com/science/article/pii/S0140700710002975.

[50] Ma, Z. W., and Zhang, P. Pressure drops and loss coefficients of a phase change material slurry in pipe fittings. *International Journal of Refrigeration*, 35(4):992–1002, 2012. ISSN 0140-7007. doi: http://dx.doi.org/10.1016/j.ijrefrig.2012.01.010. URL http://www.sciencedirect.com/science/article/pii/S0140700712000114.

[51] Ma, Z. W., and Zhang, P. Pressure drop and heat transfer characteristics of tetra-n-butyl ammonium bromide clathrate hydrate slurry during flow melting and generating in a double-tube heat exchanger. *Experimental Thermal and Fluid Science*, 44:227–234, 2013. ISSN 0894-1777. doi: http://dx.doi.org/10.1016/j.expthermflusci.2012.06.012. URL http://www.sciencedirect.com/science/article/pii/S0894177712001768.

[52] Ma, Z. W., and Zhang, P. Modeling the heat transfer characteristics of flow melting of phase change material slurries in the circular tubes. *International Journal of Heat and Mass Transfer*, 64:874–881, 2013. ISSN 0017-9310. doi: http://dx.doi.org/10.1016/j.ijheatmasstransfer.2013.05.026. URL http://www.sciencedirect.com/science/article/pii/S001793101300416X.

[53] Ma, Z. W., Zhang, P., Wang, R. Z., Furui, S., and Xi, G. N. Forced flow and convective melting heat transfer of clathrate hydrate slurry in tubes. *International Journal of Heat and Mass Transfer*, 53(19–20):3745–3757, 2010. ISSN 0017-9310. doi: http://dx.doi.org/10.1016/j.ijheatmasstransfer.2010.04.025. URL http://www.sciencedirect.com/science/article/pii/S0017931010002097.

[54] MATLAB. *version 9.2.0 (R2017a)*. The MathWorks Inc., Natick, Massachusetts, 2017.

[55] Matousek, V. Pressure drops and flow patterns in sand-mixture pipes. *Experimental Thermal and Fluid Science*, 26(6):693 – 702, 2002. ISSN 0894-1777. doi: https://doi.org/10.1016/S0894-1777(02)00176-0. URL http://www.sciencedirect.com/science/article/pii/S0894177702001760.

[56] Matsumoto, K., Murase, M., Ehara, K., Sakamoto, J., and Ueda, J. Investigation on adhesion force of tbab hydrate to cooling copper surface. *International Journal of Refrigeration*, 2017. ISSN 0140-7007. doi: http://dx.doi.org/10.1016/j.ijrefrig.2017.03.005. URL http://www.sciencedirect.com/science/article/pii/S0140700717301007.

[57] Mehling, H., and Cabeza, L. F. *Heat and cold storage with PCM : an up to date introduction into basics and applications*. Springer, 2008. ISBN 9783540685579 354068557X 9783540685562 3540685561; 1860-4846.

[58] Metzner, A. B., and Reed, J. C. Flow of non-newtonian fluids—correlation of the laminar, transition, and turbulent-flow regions. *AIChE Journal*, 1(4):434–440, 1955. ISSN 1547-5905. doi: 10.1002/aic.690010409. URL http://dx.doi.org/10.1002/aic.690010409.

[59] Mills, A. F. *Basic Heat and Mass Transfer*. Pearson Education Limited, second edition edition, 2014. ISBN 978-12-292-04248-0.

[60] National Center for Biotechnology Information. Compound summary for cid 74236. Technical report, National Institutes of Healt, 2005. URL https://pubchem.ncbi.nlm.nih.gov/compound/Tetrabutylammonium_bromide#section=Top.

[61] NEN. *Hygrothermische eigenschappen van gebouwen - Referentieklimaatgegevens*. Stichting Nederlands Normalisatie-instituut, 2008.

[62] Niezgoda-Żelasko, B., and Zalewski, W. Momentum transfer of ice slurry flows in tubes, experimental investigations. *International Journal of Refrigeration*, 29(3):418 – 428, 2006. ISSN 0140-7007. doi: https://doi.org/10.1016/j.ijrefrig.2005.09.007. URL http://www.sciencedirect.com/science/article/pii/S0140700705001842. Issue with Special Emphasis on Cryobiology.

[63] Ogoshi, H., and Takao, S. Air-conditioning system using clathrate hydrate slurry. *JFE Tech. Rep*, 3:1–5, 2004.

[64] Ogoshi, H., Matsuyama, E., Miyamoto, H., Mizukami, T., Furumoto, N., and Sugiyama, M. Clathrate hydrate slurry, chs thermal energy storage system and its applications. In *International Symposium on Next-generation Air Conditioning and Refrigeration Technology, Tokyo, Japan*.

[65] Oyama, H., Shimada, W., Ebinuma, T., Kamata, Y., Takeya, S., Uchida, T., Nagao, J., and Narita, H. Phase diagram, latent heat, and specific heat of tbab semiclathrate hydrate crystals. *Fluid Phase Equilibria*, 234(1–2):131–135, 2005. ISSN 0378-3812. doi: http://dx.doi.org/10.1016/j.fluid.2005.06.005. URL http://www.sciencedirect.com/science/article/pii/S0378381205001937.

[66] Palmer, S. C., Payne, W. V., Domanski, P. A., et al. *Evaporation and condensation heat transfer performance of flammable refrigerants in a brazed plate heat exchanger*. US Department of Commerce, Technology Administration, National Institute of Standards and Technology, 2000.

[67] Pérez-Lombard, L., Ortiz, J., and Pout, C. A review on buildings energy consumption information. *Energy and Buildings*, 40(3):394 – 398, 2008. ISSN 0378-7788. doi: https://doi.org/10.1016/j.enbuild.2007.03.007. URL http://www.sciencedirect.com/science/article/pii/S0378778807001016.

[68] Pronk, L. Air conditioning with tbab clathrate hydrate slurry as distribution fluid. Master thesis, Delft University of Technology, 2017.

[69] Pronk, P. *Fluidized bed heat exchangers to prevent fouling in ice slurry systems and industrial crystallizers*. PhD thesis, Delft University of Technology, 2016.

[70] Römer, J., and Jong, M. Warmte- en koedevraagpatronen in de utiliteitsbouw. Technical report, ECN, 1999.

[71] Schmidt, T. *Die Warmeleistung berippter Oberflachen*. Deutscher Kältetechnischer Verein, Karlsruhe, heft 4 edition, 1950.

[72] Shah, R., and Focke, W. Plate heat exchangers and their design theory. *Heat Transfer Equipment Design*, 227:254, 1988.

[73] Shi, L. Control model of a co2 booster refrigeration system for supermarkets., 2015. Mechanical Engineering, SPET.

[74] Shi, X. J., and Zhang, P. A comparative study of different methods for the generation of tetra-n-butyl ammonium bromide clathrate hydrate slurry in a cold storage air-conditioning system. *Applied Energy*, 112:1393–1402, 2013. ISSN 0306-2619. doi: http://dx.doi.org/10.1016/j.apenergy.2012.12.021. URL http://www.sciencedirect.com/science/article/pii/S0306261912009038.

[75] Shi, X. J., and Zhang, P. Cold storage by tetra-n-butyl ammonium bromide clathrate hydrate slurry generated with different storage approaches at 40 wtsolution concentration. *International Journal of Refrigeration*, 42:77–89, 2014. ISSN 0140-7007. doi: http://dx.doi.org/10.1016/j.ijrefrig.2014.02.002. URL http://www.sciencedirect.com/science/article/pii/S0140700714000267.

[76] Shi, X. J., and Zhang, P. Conjugated heat and mass transfer during flow melting of a phase change material slurry in pipes. *Energy*, 99:58–68, 2016. ISSN 0360-5442. doi: http://dx.doi.org/10.1016/j.energy.2016.01.033. URL http://www.sciencedirect.com/science/article/pii/S0360544216000542.

[77] Shimada, W., Ebinuma, T., Oyama, H., Kamata, Y., and Narita, H. Free-growth forms and growth kinetics of tetra-n-butyl ammonium bromide semi-clathrate hydrate crystals. *Journal of Crystal Growth*, 274 (1–2):246–250, 2005. ISSN 0022-0248. doi: http://dx.doi.org/10.1016/j.jcrysgro.2004.09.071. URL http://www.sciencedirect.com/science/article/pii/S0022024804012138.

[78] Shire, G. S. F., Quarini, G. L., and Evans, T. S. Pressure drop of flowing ice slurries in industrial heat exchangers. *Applied Thermal Engineering*, 29(8–9):1500–1506, 2009. ISSN 1359-4311. doi: https://doi.org/10.1016/j.applthermaleng.2008.06.033. URL http://www.sciencedirect.com/science/article/pii/S1359431108002925.

[79] Singh, R., and Kachhwaha, S. S. Heat transfer and pressure drop analysis of chilled water and ice slurry in a plate heat exchanger. *Journal of Thermal Science and Engineering Applications*, 8(1):011020–011020–9, 2015. ISSN 1948-5085. doi: 10.1115/1.4030738. URL http://dx.doi.org/10.1115/1.4030738.

[80] Sinnott, R., and Towler, G. *Chemical Engineering Design - Principles, Practice and Economics of Plant and Process Design*. Elsevier, 2013. ISBN 978-0-08-096659-5.

[81] Sloan Jr, E. D., and Koh, C. *Clathrate hydrates of natural gases*. CRC press, 2007.

[82] Song, W., Xiao, R., and Feng, Z.-p. Experimental investigation on tetra-n-butyl-ammonium bromide clathrate hydrate slurry flows in a horizontal tube: Flow behavior and its rheological model. *HVAC&R Research*, 18(3):461–467, 2012. ISSN 1078-9669.

[83] Tamasauskas, J., Poirier, M., Zmeureanu, R., and Sunyé, R. Modeling and optimization of a solar assisted heat pump using ice slurry as a latent storage material. *Solar Energy*, 86(11):3316–3325, 2012. ISSN 0038-092X. doi: http://dx.doi.org/10.1016/j.solener.2012.08.021. URL http://www.sciencedirect.com/science/article/pii/S0038092X12003246.

[84] Thonon, B. Design method for plate evaporators and condensers. In *BHR Group Conference Series Publication*, volume 18, pages 37–50. Mechanical engineering publications limited, 1995.

[85] United Nations. Paris agreement, December 2015. URL http://unfccc.int/paris_agreement/items/9485.php.

[86] United Nations Environment Programme. Montreal protocol on substances that deplete the ozone layer, September 1987. URL http://ozone.unep.org/en/handbook-montreal-protocol-substances-deplete-ozone-layer/5.

[87] U.S. Energy Information Administration. International energy outlook 2017, September 2017.

[88] van Putten, H., and Colonna, P. Dynamic modeling of steam power cycles: Part ii – simulation of a small simple rankine cycle system. *Applied Thermal Engineering*, 27(14–15):2566–2582, 2007. ISSN 1359-4311. doi: http://dx.doi.org/10.1016/j.applthermaleng.2007.01.035. URL http://www.sciencedirect.com/science/article/pii/S135943110700066X.

[89] VDI-Gesellschaft Verfahrenstechnik und Chemieingenieurwesen. *VDI Heat Atlas*. Springer-Verlag Berlin Heidelberg, 2 edition, 2010. ISBN 978-3-540-77876-9.

[90] Wang, X., and Dennis, M. Characterisation of thermal properties and charging performance of semi-clathrate hydrates for cold storage applications. *Applied Energy*, 167:59–69, 2016. ISSN 0306-2619. doi: http://dx.doi.org/10.1016/j.apenergy.2016.01.032. URL http://www.sciencedirect.com/science/article/pii/S0306261916300125.

[91] Wang, X., Dennis, M., and Hou, L. Clathrate hydrate technology for cold storage in air conditioning systems. *Renewable and Sustainable Energy Reviews*, 36:34–51, 2014. ISSN 1364-0321. doi: http://dx.doi.org/10.1016/j.rser.2014.04.032. URL http://www.sciencedirect.com/science/article/pii/S1364032114002597.

[92] Warnakulasuriya, F. S. K., and Worek, W. M. Heat transfer and pressure drop properties of high viscous solutions in plate heat exchangers. *International Journal of Heat and Mass Transfer*, 51(1–2):52–67, 2008. ISSN 0017-9310. doi: http://dx.doi.org/10.1016/j.ijheatmasstransfer.2007.04.054. URL http://www.sciencedirect.com/science/article/pii/S0017931007003730.

[93] Wenji, S., Rui, X., Chong, H., Shihui, H., Kaijun, D., and Ziping, F. Experimental investigation on tbab clathrate hydrate slurry flows in a horizontal tube: Forced convective heat transfer behaviors. *International Journal of Refrigeration*, 32(7):1801–1807, 2009. ISSN 0140-7007. doi: http://dx.doi.org/10.1016/j.ijrefrig.2009.04.008. URL http://www.sciencedirect.com/science/article/pii/S0140700709000966.

[94] Xiao, R., He, S., Huang, C., and Feng, Z. Pressure-drop and energy-saving analysis of tbab clathrate hydrate slurry as a and energy-saving analysis of tbab clathrate hydrate slurry as a latent heat transportation media. 2007.

[95] Xiao, R., Wu, S., Tang, L., Huang, C., and Feng, Z. Experimental investigation of the pressure-drop of clathrate hydrate slurry (chs) flow of tetrabutylammonium bromide (tbab) in straight pipe. In *Proceedings of 10th International Conference on Thermal Energy Storage, NJ, USA*, pages 89–96, 2006.

[96] Yan, Y. Y., and Lin, T. F. Evaporation heat transfer and pressure drop of refrigerant r-134a in a plate heat exchanger. *Journal of Heat Transfer*, 121(1):118–127, 1999. ISSN 0022-1481. doi: 10.1115/1.2825924. URL http://dx.doi.org/10.1115/1.2825924.

[97] Youssef, Z., Delahaye, A., Huang, L., Trinquet, F., Fournaison, L., Pollerberg, C., and Doetsch, C. State of the art on phase change material slurries. *Energy Conversion and Management*, 65:120–132, 2013. ISSN 0196-8904. doi: http://dx.doi.org/10.1016/j.enconman.2012.07.004. URL http://www.sciencedirect.com/science/article/pii/S0196890412002907.

[98] Zak, H. Air-conditioning in office buildings, performance-ratio between water and tbab-hydrate slurry in ac-distribution systems, applied to large office buildings. Master's thesis, Delft University of Technology, 2014.

[99] Zhang, P., and Ma, Z. W. An overview of fundamental studies and applications of phase change material slurries to secondary loop refrigeration and air conditioning systems. *Renewable and Sustainable Energy Reviews*, 16(7):5021–5058, 2012. ISSN 1364-0321. doi: http://dx.doi.org/10.1016/j.rser.2012.03.059. URL http://www.sciencedirect.com/science/article/pii/S1364032112002432.

[100] Zhang, P., and Ye, J. Experimental investigation of forced flow and heat transfer characteristics of phase change material slurries in mini-tubes. *International Journal of Heat and Mass Transfer*, 79:1002–1013, 2014. ISSN 0017-9310. doi: http://dx.doi.org/10.1016/j.ijheatmasstransfer.2014.08.067. URL http://www.sciencedirect.com/science/article/pii/S0017931014007650.

[101] Zhang, P., Shi, X. J., and Ma, Z. W. Solid fraction determination in cold storage by tetra-n-butyl ammonium bromide clathrate hydrate slurry. *International Journal of Refrigeration*, 36(3):809–819, 2013. ISSN 0140-7007. doi: http://dx.doi.org/10.1016/j.ijrefrig.2012.11.012. URL http://www.sciencedirect.com/science/article/pii/S0140700712003118.

[102] Zhang, P., Ma, Z. W., Shi, X. J., and Xiao, X. Thermal conductivity measurements of a phase change material slurry under the influence of phase change. *International Journal of Thermal Sciences*, 78: 56–64, 2014. ISSN 1290-0729. doi: http://dx.doi.org/10.1016/j.ijthermalsci.2013.11.013. URL http://www.sciencedirect.com/science/article/pii/S1290072913002810.

[103] Zhang, P., Ma, Z. W., Bai, Z. Y., and Ye, J. Rheological and energy transport characteristics of a phase change material slurry. *Energy*, 106:63–72, 2016. ISSN 0360-5442. doi: http://dx.doi.org/10.1016/j.energy.2016.03.025. URL http://www.sciencedirect.com/science/article/pii/S0360544216302699.

[104] Zhou, H. *Hydrate slurry as cold energy storage and distribution medium*. PhD thesis, Delft University of Technology, 2017.

[105] Zhou, H., Vasilescu, C., and Infante Ferreira, C. Heat transfer and flow characteristics during the formation of tbab hydrate slurry in a coil heat exchanger. *International Journal of Refrigeration*, 64: 130–142, 2016. ISSN 0140-7007. doi: http://dx.doi.org/10.1016/j.ijrefrig.2015.12.021. URL http://www.sciencedirect.com/science/article/pii/S0140700716000098.

A

Air cooler specifications

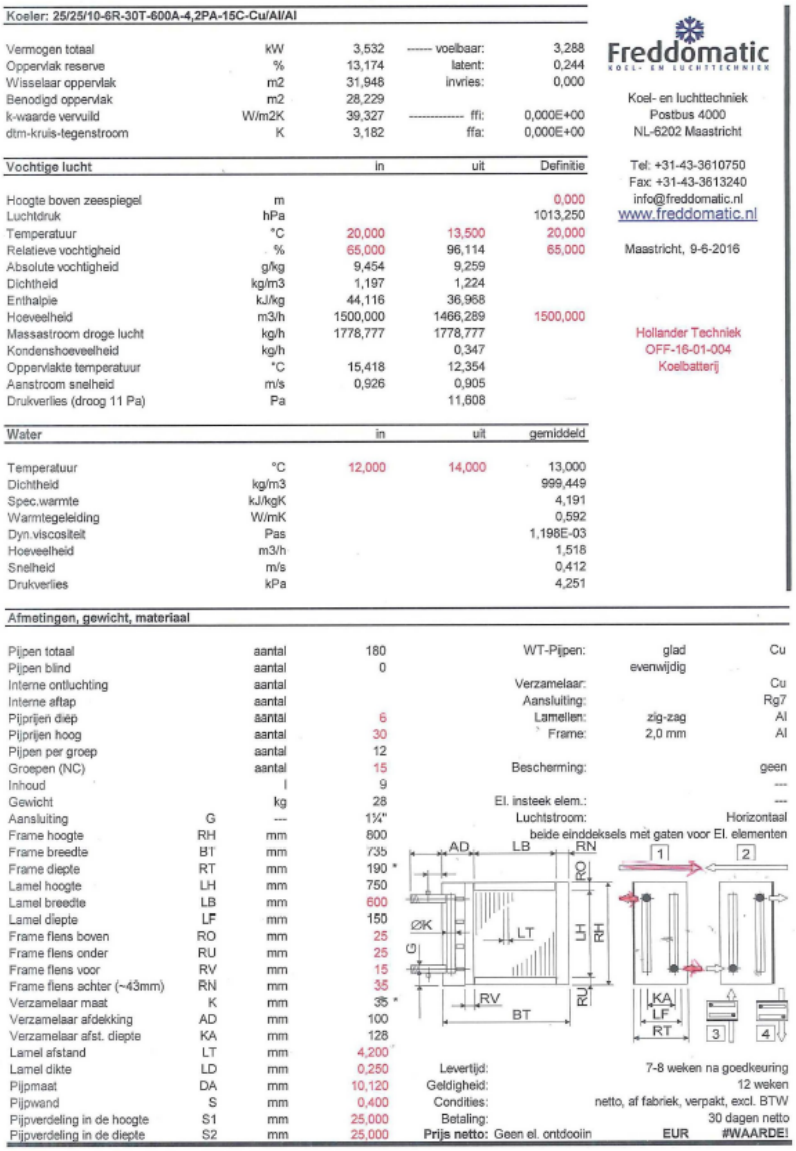

Koeler: 25/25/10-6R-30T-600A-4,2PA-15C-Cu/Al/Al

Vermogen totaal	kW	3,532	------ voelbaar:	3,288
Oppervlak reserve	%	13,174	latent:	0,244
Wisselaar oppervlak	m2	31,948	invries:	0,000
Benodigd oppervlak	m2	28,229		
k-waarde vervuild	W/m2K	39,327	---------- ffi:	0,000E+00
dtm-kruis-tegenstroom	K	3,182	ffa:	0,000E+00

Vochtige lucht		in	uit	Definitie
Hoogte boven zeespiegel	m			0,000
Luchtdruk	hPa			1013,250
Temperatuur	°C	20,000	13,500	20,000
Relatieve vochtigheid	%	65,000	96,114	65,000
Absolute vochtigheid	g/kg	9,454	9,259	
Dichtheid	kg/m3	1,197	1,224	
Enthalpie	kJ/kg	44,116	36,968	
Hoeveelheid	m3/h	1500,000	1466,289	1500,000
Massastroom droge lucht	kg/h	1778,777	1778,777	
Kondenshoeveelheid	kg/h		0,347	
Oppervlakte temperatuur	°C	15,418	12,354	
Aanstroom snelheid	m/s	0,926	0,905	
Drukverlies (droog 11 Pa)	Pa		11,608	

Water		in	uit	gemiddeld
Temperatuur	°C	12,000	14,000	13,000
Dichtheid	kg/m3			999,449
Spec.warmte	kJ/kgK			4,191
Warmtegeleiding	W/mK			0,592
Dyn.viscositeit	Pas			1,198E-03
Hoeveelheid	m3/h			1,518
Snelheid	m/s			0,412
Drukverlies	kPa			4,251

Freddomatic
KOEL- EN LUCHTTECHNIEK

Koel- en luchttechniek
Postbus 4000
NL-6202 Maastricht

Tel: +31-43-3610750
Fax: +31-43-3613240
info@freddomatic.nl
www.freddomatic.nl

Maastricht, 9-6-2016

Hollander Techniek
OFF-16-01-004
Koelbatterij

Afmetingen, gewicht, materiaal

Pijpen totaal		aantal	180	WT-Pijpen:	glad	Cu
Pijpen blind		aantal	0		evenwijdig	
Interne ontluchting		aantal		Verzamelaar:		Cu
Interne aftap		aantal		Aansluiting:		Rg7
Pijprijen diep		aantal	6	Lamellen:	zig-zag	Al
Pijprijen hoog		aantal	30	Frame:	2,0 mm	Al
Pijpen per groep		aantal	12			
Groepen (NC)		aantal	15	Bescherming:		geen
Inhoud		l	9			---
Gewicht		kg	28	El. insteek elem.:		---
Aansluiting	G	---	1¼"	Luchtstroom:		Horizontaal
Frame hoogte	RH	mm	800	beide einddeksels met gaten voor El. elementen		
Frame breedte	BT	mm	735			
Frame diepte	RT	mm	190 *			
Lamel hoogte	LH	mm	750			
Lamel breedte	LB	mm	600			
Lamel diepte	LF	mm	150			
Frame flens boven	RO	mm	25			
Frame flens onder	RU	mm	25			
Frame flens voor	RV	mm	15			
Frame flens achter (~43mm)	RN	mm	35			
Verzamelaar maat	K	mm	35 *			
Verzamelaar afdekking	AD	mm	100			
Verzamelaar afst. diepte	KA	mm	128			
Lamel afstand	LT	mm	4,200			
Lamel dikte	LD	mm	0,250	Levertijd:		7-8 weken na goedkeuring
Pijpmaat	DA	mm	10,120	Geldigheid:		12 weken
Pijpwand	S	mm	0,400	Condities:		netto, af fabriek, verpakt, excl. BTW
Pijpverdeling in de hoogte	S1	mm	25,000	Betaling:		30 dagen netto
Pijpverdeling in de diepte	S2	mm	25,000	**Prijs netto:** Geen el. ontdooiin	**EUR**	**#WAARDE!**

Figure A.1: Specifications from the manufacturer of the air cooler used in the pilot plant

B

Pump characteristics

The manufacturer of the two peripheral pumps, T MAG-M2 and T MAG-M2, provided the pump characteristics of the pump at a rotational speed of 2900 rpm. This data can be found in figure B.1 and figure B.2 for the pump T MAG-M2 and T MAG-M4 respectively. This data is used to describe the pump characteristics at other rotational speeds as discussed in section 5.2. Figure B.3 shows the modelled pump characteristics of the T MAG-M2 pump and figure B.4 shows the modelled pump characteristics of the T MAG-M4 pump.

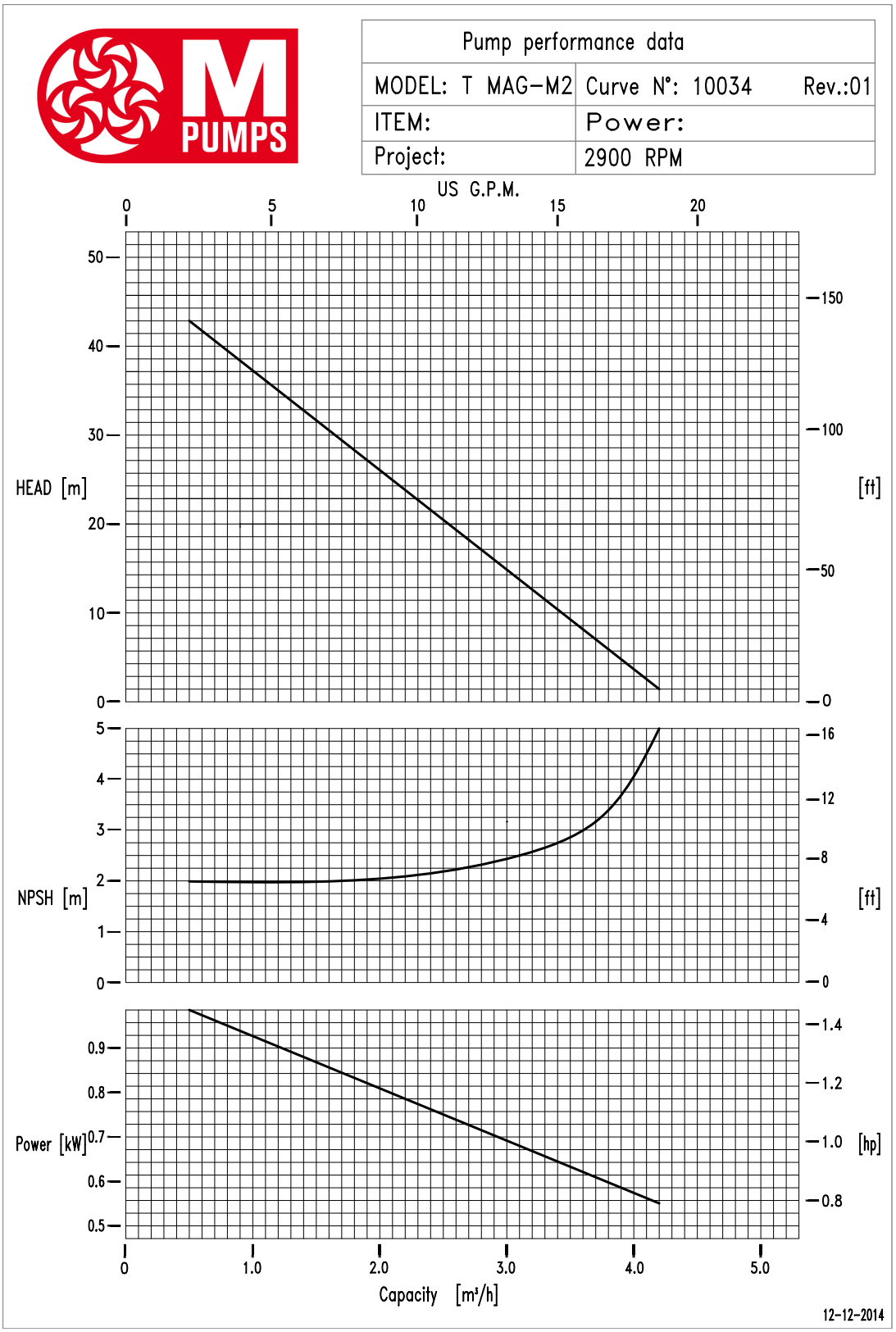

Figure B.1: Pump characteristic of the T MAG-M2 peripheral pump at a rotational speed of 2900 rpm.

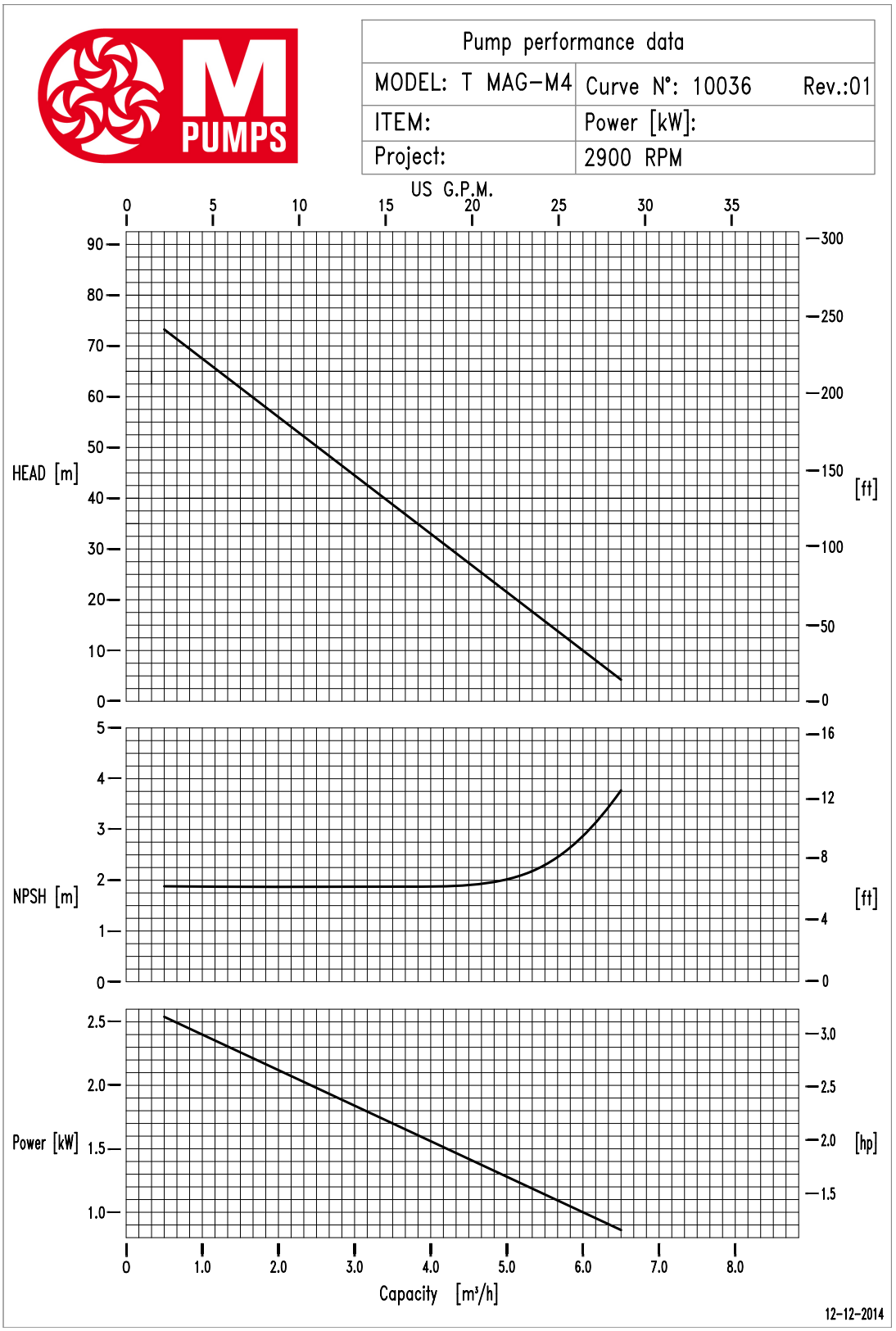

Figure B.2: Pump characteristic of the T MAG-M4 peripheral pump at a rotational speed of 2900 rpm.

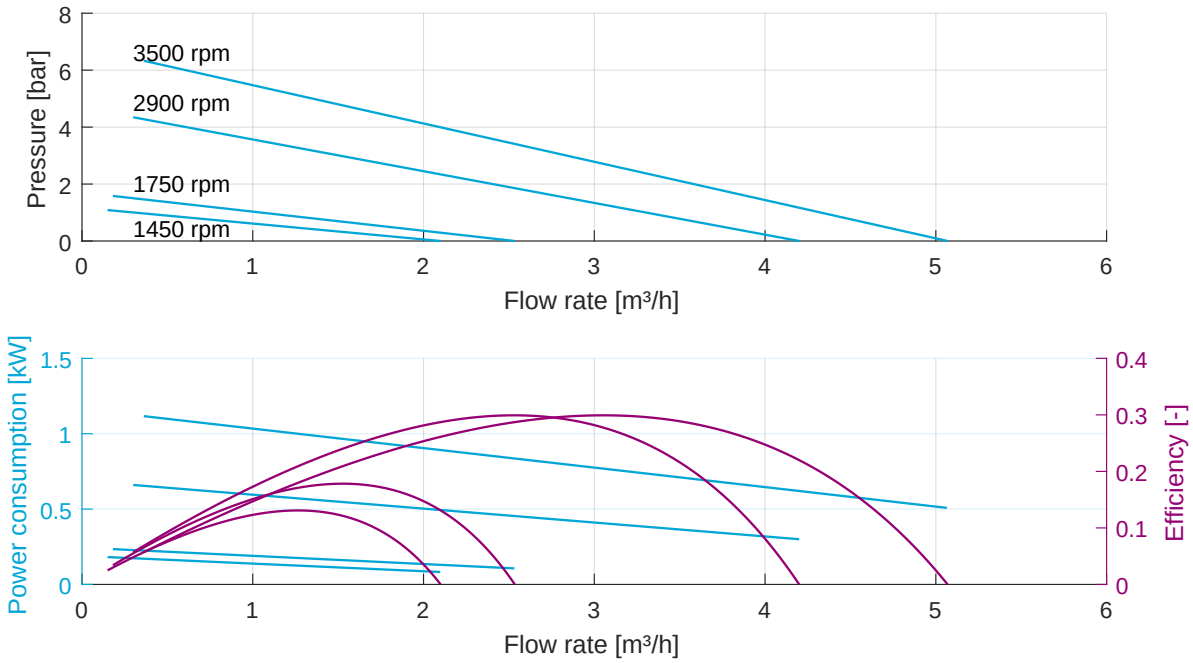

Figure B.3: The pump characteristics of the T MAG-M2 pump.

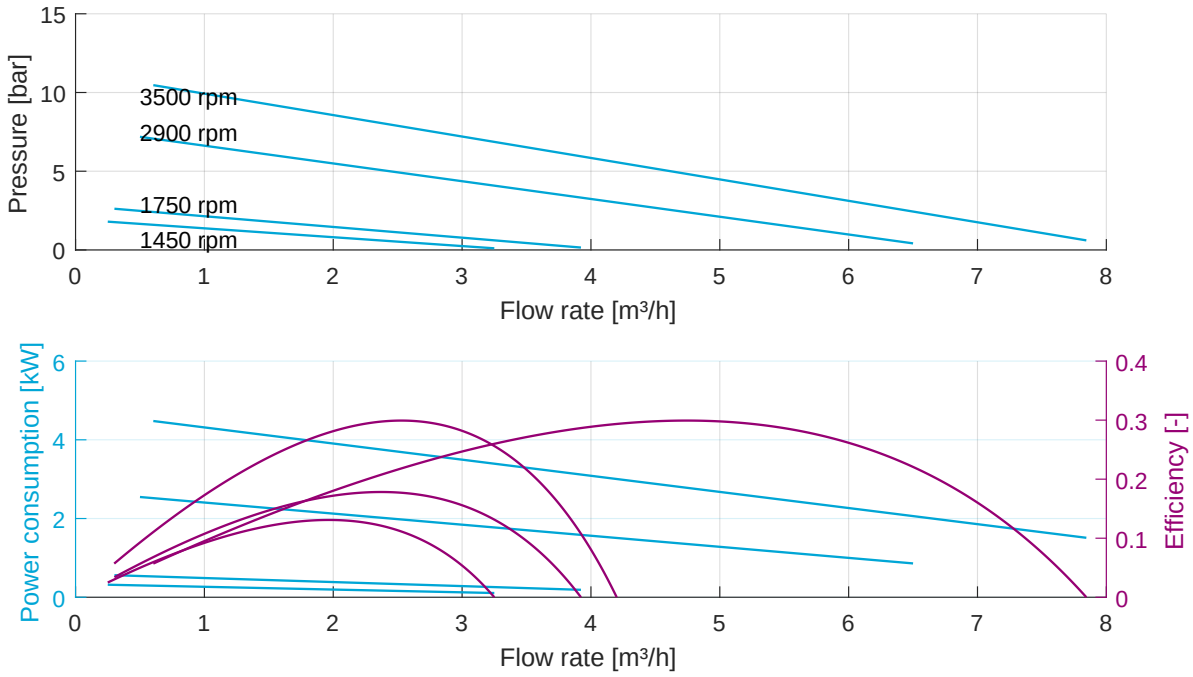

Figure B.4: The pump characteristics of the T MAG-M4 pump.

C

Data acquisition

The data acquisition of the pilot system in Twello is composed of a data logger and multiple sensors. The data logger measures every 10 seconds the data output of the sensors. The transducers consist out of temperature sensors, flow sensors, pressure sensors, density sensors and power sensors. Table C.1 summarizes the sensors and the accuracy of the sensors. Figure C.1 shows the global configuration of the sensors.

The precision of the data is limited by the number of decimals of the saved data. This precision can be manually adjusted in the data logger. The precision of the data is set to match the accuracy of the transducers.

Table C.1: Summary of the sensors used in the pilot plant in Twello and the accuracies of the instrumentation.

Sensor name	Property	Unit	Accuracy
FT10.01A, FT20.01A, FT30.01A	Density	kg/m³	±0.5
FT10.01B, FT20.01B, FT30.01B	Flow rate	kg/h	±0.15 %
V10.01	Valve opening	%	-
PT10.01, PT10.02, PT10.03, PT10.04, PT20.01, PT20.02, PT30.01	Pressure	kPa	1.0
TT10.01, TT10.02, TT10.03, TT20.01, TT20.02, TT30.01, TT30.02, TT30.03, TT30.04, TT30.05 T40.01	Temperature	K	0.03
M10Spd, P21Spd, P31Spd	Rotational speed	%	-
M10Power, P21Power, P31Power	Power	W	-

The accuracy of the sensor is not only determined by the sensors itself, but also the placement of the sensors has influence on the accuracy. The pressure- and temperature sensors are placed for instance in the center of the connecting pipes between the components. For example, when the pressure drop over the generator is measured, the pressure drop over a small pipe section is also measured. Since the pressure drop over the generator is much larger compared to the pressure drop over a pipe section, this effect is assumed to be negligible.

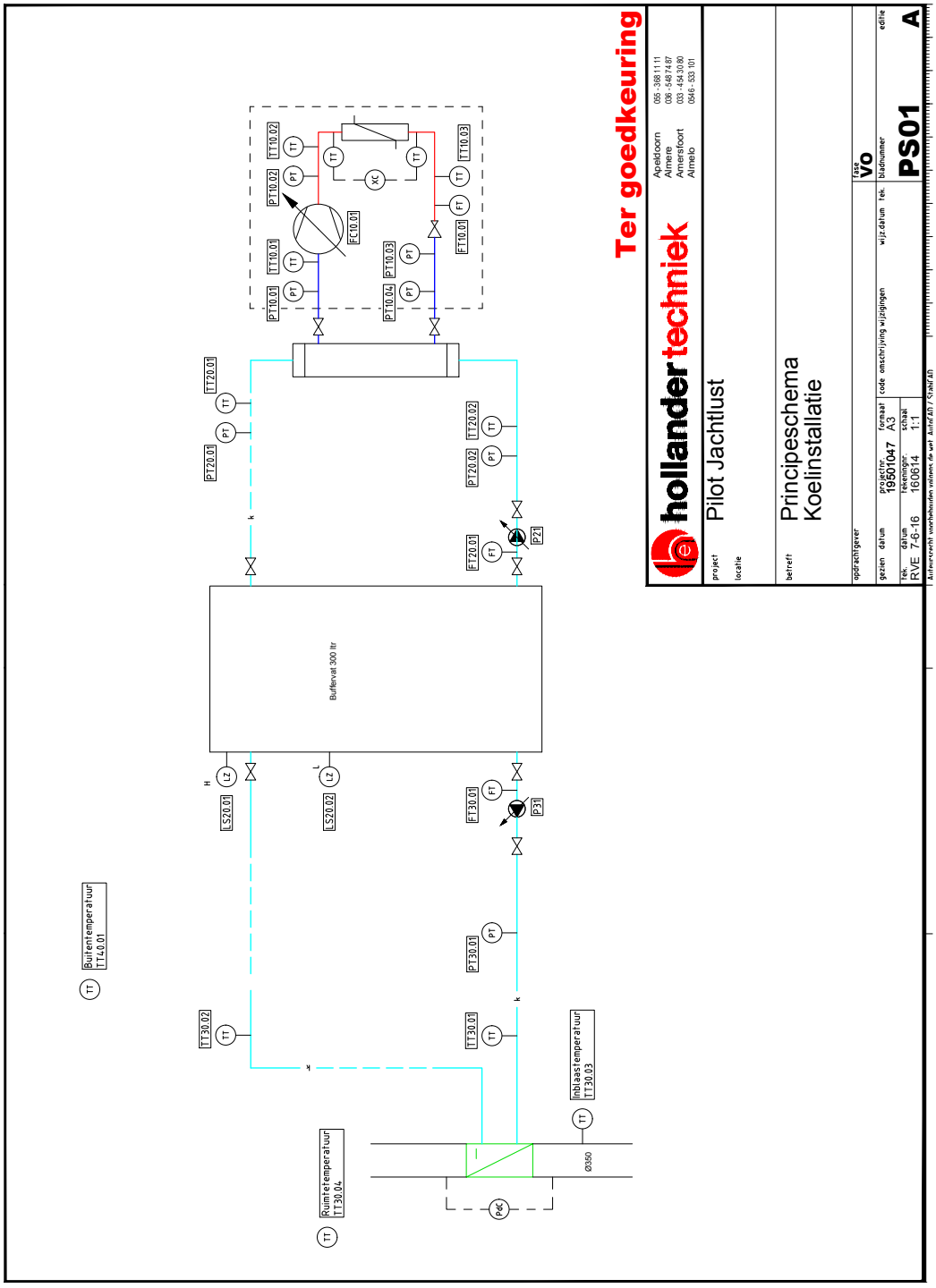

Figure C.1: A global overview of the sensor configuration at the pilot plant provided by Holland Techniek.